Master Thesis

Josephson effect in normal and ferromagnetic topological insulator junctions

Jennifer Nussbaum

April 10, 2014
(revised: May 8, 2014)

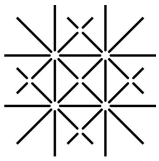

Department of Physics, University of Basel
Klingelbergstrasse 82, 4056 Basel, Switzerland

Supervisors: Dr. Rakesh Tiwari
Dr. Thomas L. Schmidt
Prof. Dr. Christoph Bruder

Contents

1 Introduction

In condensed matter physics a large variety of systems, as for example crystalline solids, magnets, superconductors, superfluids, liquid crystals etc. are investigated and one aims to know how electrons and atoms in the quantum world can originate their properties. Since the last century these quantum states can be classified by the principle of spontaneous symmetry breaking [1]. For instance, a superconductor breaks the gauge symmetry, which leads to phenomena as flux quantization and Josephson effects. There exists a state which does not follow this principle: the quantum Hall state. This 2D state is insulating in the bulk, but along the edge, electric current can be carried. This unidirectional current causes a quantized Hall effect. The quantum Hall state is the first example of a quantum state which is topologically distinct from all states of matter known before.
To distinguish such different quantum states, a mathematical concept is used: the concept of topological invariance. Mathematicians classify different geometrical objects in terms of this concept into broad classes. A popular example are 2D surfaces, which are classified by the number holes in them (also called genus). For example, the surface of a square is topologically equivalent to the surface of a circle or a triangle. Similarly one can smoothly deform a coffee cup into a donut, which in this terms also means they are topologically equivalent: both have one hole.
The key concept which is used in physics for this topological classification is the "smooth deformation". To be more precise, one can consider a Hamiltonian of many particle systems with an energy gap. A smooth deformation then is defined as a change in the Hamiltonian which does not close the bulk gap. This concept can be applied to insulators as well as to superconductors with a full energy gap but not to gapless states as for example metals. If two gapped states are in a different topological class, one gapped state cannot be deformed into the other gapped state unless a quantum phase transition occurs where the system becomes gapless.
Mathematicians expressed the concept of genus in terms of an integral over the local curvature of the surface. This integral is called the topological invariant. Similarly topologically quantized physical quantities can be expressed as invariant integrals over the frequency momentum space. Such an integral uniquely determines the nature of the quantum states enabling it to serve as a topological order parameter.

In 2005 Kane and Mele [2] found such a topological invariant that could be computed for any 2D material. This allows to predict, whether a material has a stable edge state and it enabled them to show that there have to exist realistic 2D materials with a stable edge state. Soon after, Bernevig, Hughes and Zhang predicted theoretically that a 2D topological insulator would be realized in HgTe/CdTe quantum wells [3]. König et al. observed this experimentally in 2007. In 2006 it was found that the 2D topological insulator can be generalized to 3D ([4], [5], [6]). Eventually, in 2008 the first 3D topological insulator, the semiconducting alloy $Bi_{1-x}Sb_x$, was experimentally identified [7].

These new 2D and 3D quantum states are invariant under time-reversal (TR) symmetry, and spin-orbit coupling (SOC) plays an essential role. All TR invariant insulators in nature without ground state degeneracy can be distributed into two classes which are classified by a $\mathbb{Z}_2$ topological order parameter. One class is formed by the topologically trivial states, which are gapped inside the bulk and on the surface. The other class represents the topologically nontrivial insulators which have a full insulating gap in the bulk, but gapless edge or surface states.
In a nutshell, topological insulators are new states of quantum matter whose electronic structure cannot be adiabatically connected to conventional insulators and semiconductors. They are characterized by a full insulating gap in the bulk and gapless edge or surface states which are protected by TR symmetry. Moreover, they exhibit certain qualities, which make them particularly interesting for research.

Some of these exciting qualities we will employ in this thesis. We aim to calculate the Josephson effect on topological insulator surfaces. We use not only the conductive property of the surface states, but also the special form of the proximity-induced topological superconductivity and ferromagnetism. It is a very convenient circumstance, that the surface states of the topological insulator can be described by a simple 2×2 Dirac Hamiltonian.

To introduce the reader into the topic, the thesis begins with a theory part explaining topological insulators, the BCS theory of superconductivity, proximity effects and Andreev reflection. In the main part we provide a derivation of the Hamiltonians of the topological insulator surface states which are used to calculate the Josephson effect. Afterwards we investigate the Josephson effect in topological insulator planar, step and edge junctions and finally in ferromagnetic topological insulator planar and step junctions.

2 Theory

2.1 2D topological insulators: HgTe/CdTe

To understand the concept of a 3D topological insulator we will begin with the simpler case of a 2D topological insulator. The explanation of the topological band structure in 2D can then be generalized to the band structure in 3D.

The first 2D topological insulator was discovered in HgTe/CdTe quantum wells theoretically in 2006 by Bernevig, Hughes, and Zhang [3] and experimentally in 2007 by König et al. [8]. They observed an insulating state which is conducting only through 1D edge channels. Furthermore, the state is strongly influenced by a TR symmetry-breaking magnetic field.
In this section we will make a brief introduction to 2D topological insulators and we will discuss HgTe/CdTe quantum wells as a concrete example.

2.1.1 2D topological insulators

A 2D topological insulating state, also called quantum spin Hall (QSH) insulator state is characterized by three specific features: it is invariant under TR, it has a charge excitation gap in the bulk and it has topologically protected 1D gapless edge states that lie inside the bulk insulating gap. By topologically protected edge states we refer to the fact, that the TR symmetry prevents the edge states from backscattering. The absence of backscattering relies on the destructive interference between all possible backscattering paths taken by the edge electrons. This destructive interference is due to the helical nature of the edge states which means: at a given edge, two spins with opposite spin polarization counterpropagate, thus the spin is correlated with the direction of motion [9].
A key to understand these topological nontrivial edge states is the analysis of the TR symmetry. TR symmetry is represented by an anti unitary operator $\mathcal{T} = e^{i\pi\sigma_y/2}K$ with the Pauli matrix σ_y and the complex conjugation K. For a spin-1/2 particle the TR operator has the property $\mathcal{T}^2 = -1$ which is due to the fact that TR leads to a spin flip. There exists a theorem, Kramers' theorem, which states that all eigenstates of a TR invariant Hamiltonian are at least twofold degenerate (up and down spins in absence of SOC). Kramers' theorem can be explained with the anti unitary TR operator $\mathcal{T}$. For a TR invariant system, two states $|\chi\rangle$ and $\mathcal{T}|\chi\rangle$ have the same energy. If we can prove, that they are two different quantum states, it proves Kramers' theorem. Thus, we assume a non degenerate state $|\chi\rangle$ existed and we assume, that the state $\mathcal{T}|\chi\rangle$ with the same energy is the same state. Then $\mathcal{T}^2|\chi\rangle = \mathcal{T}c|\chi\rangle = c^*\mathcal{T}|\chi\rangle = |c|^2|\chi\rangle$ for a constant c. This is not allowed because $|c|^2 \neq -1 = \mathcal{T}^2$ for spin-1/2 particles. Consequently, these two states have to be different, implying that the edge states occur in Kramers doublets.

We can group TR invariant Hamiltonians in two topological classes. We try to understand this with the energy dispersion illustrated in Fig. 1. The Fig. shows half of the Brillouin zone: $0 < k < \pi/a$, where k is the crystal momentum along the edge. Due to TR symmetry we know that the other half, $-\pi/a < k < 0$, is a mirror image. Furthermore, the conduction and the valence bands of the bulk, separated by an energy gap, are drawn. Depending on the Hamiltonian near the edge there may be edge states inside the gap. We assume there are such edge states inside the gap. Kramers' theorem now requires that they are twofold degenerate at TR invariant crystal momenta k. As TR symmetry transfers k to $-k$, we have two such TR invariant points: $k = 0$ and $k = \pi/a$. Away from these points, SOC splits the degeneracy.
In a next step we want to connect these special points. There are two ways to do this: we can connect them pairwise, as in Fig. 1(a) or not pairwise as in Fig. 1(b). In the first case, we can push the bound states out of the gap by shifting the Fermi energy E_F. This is not possible in the second case, as E_F is intersected an odd number of times. Each intersection of E_F at k has a partner at $-k$. We can count the number of Kramers' pairs n_k intersecting E_F. This number can be related to the change in a $\mathbb{Z}_2$ topological invariant ν across the interface: $n_k = \delta\nu$ mod2.
The topological properties of the 2D topological insulator are mathematically characterized by this $\mathbb{Z}_2$ topological invariant ν: states with an even number of Kramers' pairs of edge states at an edge are topologically trivial ($\nu = 0$), those with an odd number are nontrivial ($\nu = 1$).

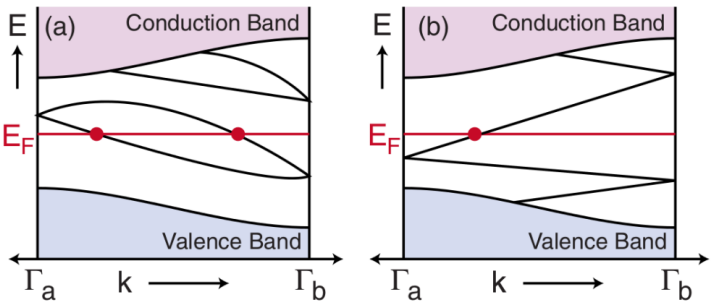

Figure 1: Energy dispersion in half of the Brillouin zone. Γ_a at $k = 0$ and Γ_b at $k = \pi/a$ are the two Kramers' degenerate points. Away from these points the degeneracy is lifted by SOC. The points can be connected in two ways such that the Fermi energy E_F is intersected (a) an even number of times and (b) an odd number of times. Adapted from Ref. [10].

2.1.2 HgTe/CdTe quantum wells

As an example of a 2D topological insulator, the topological insulator in HgTe/CdTe quantum wells is reviewed. The basic electronic structure of the bulk HgTe and CdTe can be depicted by a model introduced by Bernevig, Hughes, and Zhang (BHZ) in 2006 [3]. It describes the physics of the subbands of the quantum wells which are relevant for the QSH effect. Both, HgTe and CdTe, crystallize in zinc blende lattice structure (diamond lattice formed by two interpenetrating fcc lattices shifted along the body diagonal and each sublattice is made of a different atom). The important bands near the Fermi level are close to the Γ point in the Brillouin zone.

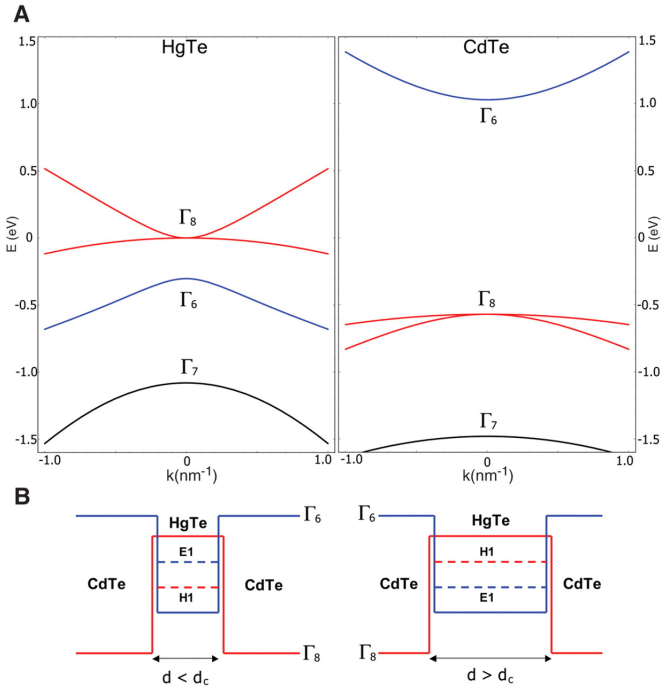

Figure 2: Energy bands: red $\Gamma_8/H1$ and blue $\Gamma_6/E1$. (A) Bulk energy bands of HgTe and CdTe near the Γ point. (B) The quantum well in the normal regime $E1 > H1$ and $d > d_c$ (left) and in the inverted regime $H1 > E1$ and $d > d_c$ (right). Adapted from Ref. [3].

In Fig. 2(A) the energy bands near the Γ point of HgTe and CdTe are shown. CdTe has a s-type Γ_6 conduction band and a p-type Γ_8 valence band which is split into two bands (with total angular momentum $J = 3/2$ and $J = 1/2$) due to SOC. In HgTe the p-levels rise above the s-levels due to the

heavy element Hg, thus it has an inverted band structure.
Now the HgTe is sandwiched between layers of CdTe. This is shown in Fig. 2(B). When the thickness d of the HgTe layer is smaller than a critical thickness $d_c = 6.3nm$, the 2D electronic states ($E1$, $H1$) bound to the quantum well have the normal band order. But for $d > d_c$ the 2D bands invert. In [11] they demonstrate with a simple model why quantum wells with $d > d_c$ are expected to be TR invariant 2D topological insulators with protected edge states.
BHZ showed that the band inversion as a function of the thickness d signals a quantum phase transition between the trivial insulator and the QSH insulator. The system can be approximated by constructing an effective Hamiltonian considering bulk symmetries. The opposite parity of the s- and p-states results in the crossing of the bands at d_c and the energy gap vanishes at $d = d_c$. This signals a phase transition in which the $\mathbb{Z}_2$ topological invariant ν changes.

In the basis $\{|E1+\rangle, |H1+\rangle, |E1-\rangle, |H1-\rangle\}$, where $|E1\pm\rangle$ are the Kramers' partners of the s-type electron band and $|H1\pm\rangle$ are the Kramers' partners of the heavy-hole band (compare Fig. 2), the model takes the following form:

$$H(\mathbf{k}) = \begin{pmatrix} h(\mathbf{k}) & 0 \\ 0 & h^*(-\mathbf{k}) \end{pmatrix}, \tag{1}$$

$$h(\mathbf{k}) = \varepsilon(\mathbf{k})\mathbb{I}_{2\times 2} + d_i(\mathbf{k})\sigma_i, \tag{2}$$

with the 2×2 identity matrix $\mathbb{I}_{2\times 2}$ and the Pauli matrices σ_i. $d_i(\mathbf{k})$ can be expanded:

$$d_1 + id_2 = A(k_x + ik_y), \qquad d_3 = M - B(k_x^2 + k_y^2), \qquad \varepsilon(\mathbf{k}) = C - D(k_x^2 + k_y^2). \tag{3}$$

A, B, C and D are expansion parameters that depend on the heterostructure [3]. M is the mass or gap parameter, which is the energy difference between the $E1$ and $H1$ levels at the Γ point and thus the most important quantity. When the thickness d gets bigger than the critical thickness d_c, the sign of M changes, signifying that the $E1$ and $H1$ bands cross at $d = d_c$.

Eventually we understand 2D topological insulators and know how they can be realized. The whole concept can now be transferred to 3D topological insulators.

2.2 3D topological insulators: Bi_2Se_3

The topological characterization of the QSH insulator state has a natural generalization in three dimensions. This was discovered in 2006 ([4], [5], [6]). In contrast to the QSH insulator, 3D topological insulators are characterized by four $\mathbb{Z}_2$ topological invariants $(\nu_0; \nu_1, \nu_2, \nu_3)$. In this chapter some basics about 3D topological insulators are summarized and explained.

2.2.1 Strong and weak topological insulators

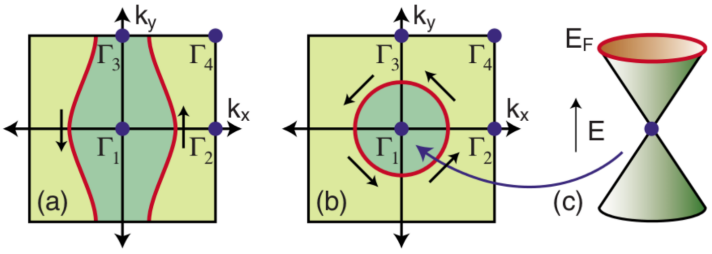

Figure 3: 2D surface Brillouin zone with the Fermi circles (red). (a) illustrates a weak topological insulator, where the Fermi circle encloses an even number of Dirac points Γ. In (b) the simplest case of a strong topological insulator (one enclosed Dirac point) is shown. In (c) the corresponding energy relation is drawn. Adapted from Ref. [10].

The surface states of a 3D crystal can be described with a 2D crystal momentum. We analyze the 2D surface states the same way as we did in the 2D case with the 1D edge states. To provide support, we

use Fig. 3, where the Fermi surfaces in the surface Brillouin zone are shown. In 2D the surface Brillouin zone has four TR invariant points $\Gamma_{1,2,3,4}$ where the surface states must be Kramers degenerate. Away from these points the degeneracy is lifted by SOC. A line joining a pair Γ_a and Γ_b can be crossed by the surface Fermi surface an even or an odd number of times, which is determined by the four topological invariants. If it is odd, then the surface states are topologically protected, like in the 2D case.
Still, there exist several possibilities for nontrivial 3D topological insulators. A possible Fermi surface is illustrated in 3(a). A single surface band intersects the Fermi energy between Γ_1 and Γ_2 and between Γ_3 and Γ_4. This state is called a weak topological insulator. It can be constructed by stacking layers of 2D quantum spin Hall insulators. If we stack the layers along the $y-$direction, we would get something like the Fermi surface illustrated in Fig. 3(a). We can interpret the indices (ν_1, ν_2, ν_3) as Miller indices describing the orientation of the layers. The important topological invariant is ν_0 which determines, whether an even or an odd number of Kramers' points is enclosed by the surface Fermi circle. This weak topological insulator has $\nu_0 = 0$ as the Fermi circle encloses Γ_1 and Γ_3. If the surface Fermi circle encloses an odd number of Kramers' degenerate Dirac points, it is called a strong topological insulator and we have the topological invariant $\nu_0 = 1$. This is illustrated in Fig. 3(b), where only the Γ_1 point is enclosed. In Fig. 3(c) we can see the energy dispersion which takes a cone form due to Kramers' degeneracy. Strong topological insulators of the form shown in Fig. 3 are the simplest, as there is only one Dirac point encircled by the Fermi energy. We can describe this topological insulator by the Hamiltonian

$$H = -i\hbar v_F \sigma \cdot \nabla, \tag{4}$$

where σ is the vector of Pauli matrices which characterizes the spin. The electronic structure of the surface of a topological insulator is quite similar to that of graphene, but instead of the two Dirac points and the spin degeneracy in graphene, there is just a single Dirac point without spin degeneracy in a topological insulator. This appears to violate Kramers' theorem, but it is solved as the partner Dirac points reside on opposite surfaces.

The 2D topological metal formed by the surface states of a strong topological insulator is quite unique. In contrast to an ordinary metal, which has up and down spins at every point of the Fermi surface, the surface states of the strong topological insulator are not spin degenerate. TR symmetry requires that states with momentum $\mathbf{k}$ and $-\mathbf{k}$ have opposite spin. Thus the spin must rotate with $\mathbf{k}$ around the Fermi surface. This is shown in Fig. 3(b) by the arrows. If an electron goes around the Fermi circle, it gains a so-called Berry phase of 0 or π. If an electron circles a Dirac point, its spin rotates by 2π, leading to a π Berry phase. Due to the fact that the surface is connected to the bulk, the metallic surface state cannot vanish, even when disorder or impurities at the surface lead to scattering of the surface states.

To find 3D topological insulators one searches for insulators where the conduction and the valence bands have opposite parity and a 'band inversion' occurs when the strength of some parameter (for example the SOC) is tuned. On the basis of such an analysis, in 2008 a Princeton University group led by Hasan [7] could experimentally identify the first 3D topological insulator, the semiconducting alloy $Bi_{1-x}Sb_x$. But the surface states in $Bi_{1-x}Sb_x$ are very complicated and cannot be described by simple model Hamiltonians. For this reason, this work focuses on the Bi_2Se_3 topological insulator which can be described by a simple low-energy effective Hamiltonian.

2.2.2 Low-energy effective model of the Bi_2Se_3 topological insulator

In this section, the effective model of the Bi_2Se_3 topological insulator is explained (also valid for Bi_2Te_3 and Sb_2Te_3) in form of a summary of the paper "Topological insulators in Bi_2Se_3, Bi_2Te_3 and Sb_2Te_3 with a single Dirac cone on the surface" from Haijun Zhang et al., 2009 [12]. A detailed description of the models can be found in Ref. [13].

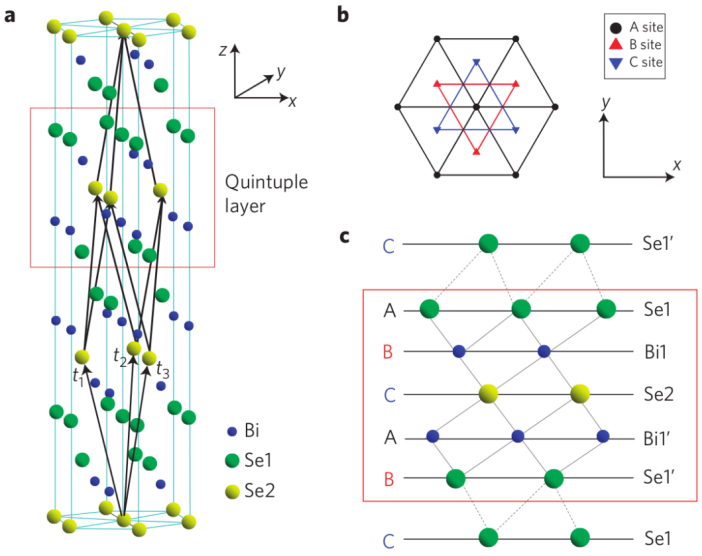

Figure 4: (a) Crystal structure of Bi_2Se_3. A quintuple layer with Se1–Bi1–Se2–Bi1'–Se1' is indicated by the red square. (b) Top view along the $z-$direction. The triangle lattice in one quintuple layer has three different positions, denoted as A, B and C. (c) Side view of the quintuple layer structure. Adapted from Ref. [12].

Bi_2Se_3 has a rhombohedral crystal structure with the space group D^5_{3d} ($R\bar{3}m$) with five atoms in one unit cell (see Fig. 4). It has a three-fold rotation symmetry about the $z-$axis and a two fold rotation symmetry about the $x-$axis. It consists of five-atom layers arranged along the $z-$direction, known as quintuple layers. These layers consist of two equivalent Se atoms, Se1 and Se1', and two equivalent Bi atoms, Bi1 and Bi1', and a third Se atom, Se2. The coupling between two atomic layers within one quintuple layer is strong and the coupling between two quintuple layers is much weaker and predominantly of the Van der Waals type. There exists an inversion symmetry, where the Se2 site is the inversion center. This enables the construction of eigenstates with definite parity.

To get a physical picture of the band structure one looks at the atomic orbitals of Bi and Se. Bi has the electron configuration $6s^26p^3$ and Se has $4s^24p^4$. Only the outermost shells are considered (p-orbitals) and the others are neglected. Within one quintuple layer there are five atoms in one unit cell and each has three orbitals: p_x, p_y and p_z. Figure 5 shows the orbitals of Bi and Se at the Γ point. In order to construct a low-energy effective Hamiltonian, we need to identify the low lying states at the Γ point. We do this in several steps where we examine one interaction at one time and search for the states nearest the Fermi energy. The states farther away can then be neglected as their contribution to a low-energy effective Hamiltonian is negligible. We proceed as follows:

1. At first, the spin is neglected. As all Se layers are separated by Bi layers, the strongest coupling is the coupling between Bi and Se layers. This coupling causes level repulsion such that the Bi energy levels are pushed up and form two hybridized states, while the Se energy levels are pushed down and yield three states. Due to inversion symmetry, the system can be described by bonding and antibonding states with definite parity. If the coupling between the Bi states is taken into account, the bonding and antibonding states are split and the antibonding state has higher energy than the bonding state. The only states which are considered are denoted as $|P1^+_\alpha\rangle$ ($\alpha = x, y, z$) which is the bonding state of Bi and $|P2^-_\alpha\rangle$ which is the antibonding state of Se. These are the states found near the Fermi surface and the others can be neglected. They are marked green in Fig. 5 at stage (I) and (II).

2. As the crystal has a layered structure, the $z-$direction is different than the $x-$ or $y-$direction. The resulting energy splitting between p_z and $p_{x,y}$ yields that the conduction band mainly consists

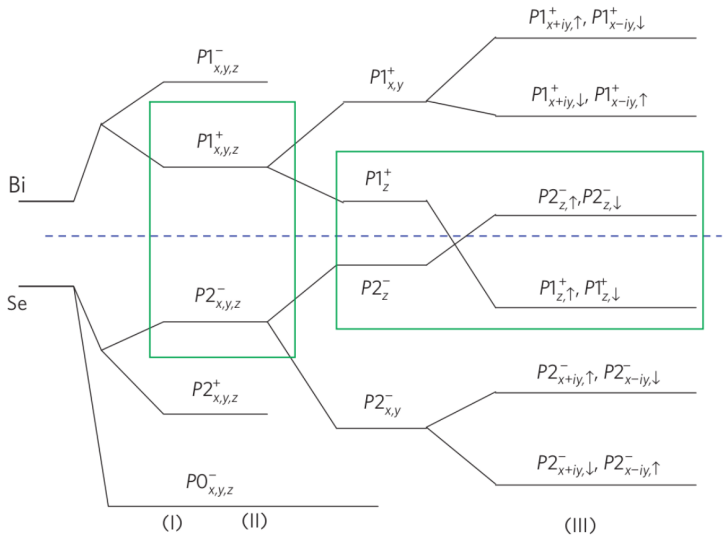

Figure 5: Atomic $p_{x,y,z}$ orbitals of Bi and Se of Bi_2Se_3 at the Γ point. The stages (I), (II) and (III) represent the effect of turning on chemical bonding (I), crystal-field splitting (II) and SOC (III). The index $j = x, y, z$ (in eg. $P1^{\pm}_j$ and $P2^{\pm}_j$) denotes the momentum $p_{x,y,z}$. The blue dashed line represents the Fermi energy. Adapted from Ref. [12].

of $|P1^+_z\rangle$ while the valence band is dominated by the $|P2^-_z\rangle$ orbital (see Fig. 5 between stage (II) and (III)).

3. Finally, SOC is included into the atomic picture. The states are all doubly degenerate: $|P1^+_\alpha\sigma\rangle$ and $|P2^-_\alpha\sigma\rangle$ with the spin $\sigma = \uparrow, \downarrow$. The SOC Hamiltonian is given by $H_{SO} = \lambda \mathbf{LS}$ with the orbital angular momentum $\mathbf{L}$, spin angular momentum $\mathbf{S}$ and the SOC parameter λ. We transform the p_x and p_y orbitals to $p_{x\pm iy}$ with definite orbital angular momentum:

$$|\Lambda_{x+iy}\sigma\rangle = -\frac{1}{\sqrt{2}}(|\Lambda_x\sigma\rangle + i\,|\Lambda_y\sigma\rangle), \tag{5}$$

$$|\Lambda_{x-iy}\sigma\rangle = \frac{1}{\sqrt{2}}(|\Lambda_x\sigma\rangle - i\,|\Lambda_y\sigma\rangle), \tag{6}$$

where $\Lambda = P1^+, P2^-$. The spin orbit Hamiltonian mixes spin and orbital angular momenta but preserves the total angular momentum. After some calculation it can be seen that SOC couples $|\Lambda_z \uparrow\rangle$ ($|\Lambda_z \downarrow\rangle$) and $|\Lambda_{x-iy} \downarrow\rangle$ ($|\Lambda_{x-iy} \uparrow\rangle$) such that it leads to a level repulsion between the states resulting in the band diagram of stage (III) in Fig. 5. The states relevant to a low-energy effective Hamiltonian are $|P2^-_z\sigma\rangle$ and$|P1^+_z\sigma\rangle$. We can see, that the order of these levels is reversed. This band inversion happens when the SOC is strong enough ($\lambda > \lambda_c$). It resembles the quantum phase transition in the HgTe/CdTe quantum wells discussed before.

The topological nature is determined by the physics near the Γ point. We write down a low-energy effective model to characterize the low-energy and long-wavelength properties of the system by using the symmetries of the atomic structure.
As basis we choose the four low-lying states: ($|P1^+_z \uparrow\rangle$, $|P2^-_z \uparrow\rangle$, $|P1^+_z \downarrow\rangle$, $|P2^-_z \downarrow\rangle$). The important symmetries of the system are:

1. TR symmetry with the representation $\mathcal{T} = K \cdot i\sigma_y \otimes \mathbb{I}_{2\times2}$,
2. inversion symmetry with the representation $I = \mathbb{I}_{2\times2} \otimes \tau_z$,
3. three-fold rotation symmetry C_3 along the $z-$axis with the representation $C_3 = e^{i(\pi/3)\sigma_z \otimes \mathbb{I}_{2\times2}}$.

K is the complex conjugation, $\sigma_{x,y,z}$ are the Pauli matrices in the spin space and $\tau_{x,y,z}$ are the Pauli matrices in the orbital space. If one requires these three symmetries and keeps only the terms up to quadratic order in $\mathbf{k}$, the following effective Hamiltonian can be obtained:

$$H(\mathbf{k}) = \varepsilon_0(\mathbf{k})\mathbb{I}_{4\times 4} + \begin{pmatrix} M(\mathbf{k}) & A_1 k_z & 0 & A_2 k_- \\ A_1 k_z & -M(\mathbf{k}) & A_2 k_- & 0 \\ 0 & A_2 k_+ & M(\mathbf{k}) & -A_1 k_z \\ A_2 k_+ & 0 & -A_1 k_z & -M(\mathbf{k}) \end{pmatrix} \tag{7}$$

where $k_\pm = k_x \pm i k_y$, $\varepsilon_0(\mathbf{k}) = C + D_1 k_z^2 + D_2 k_+ k_-$, $M(\mathbf{k}) = M - B_1 k_z^2 - B_2 k_+ k_-$, and $k_+ k_- = k_x^2 + k_y^2$. (The exact derivation is described in Ref. [13] as well as a derivation using the $\mathbf{k}\cdot\mathbf{p}$ perturbation theory.)

H. Zhang et al. [12] fitted the energy spectrum of the effective Hamiltonian with that of their ab initio calculation and received the following parameters for the effective model for Bi_2Se_3: $M = 0.28$ eV, $A_1 = 2.2$ eVÅ, $A_2 = 4.1$ eVÅ, $B_1 = 10$ eVÅ^2, $B_2 = 56.6$ eVÅ^2, $C = -0.0068$ eV, $D_1 = 1.3$ eVÅ^2, $D_2 = 19.6$ eVÅ^2.
There exists a straightforward procedure to obtain the effective Hamiltonian describing the surface states [14]. The effective Hamiltonian describing carriers in the $(x-y)$ plane in a topological insulator is then given by [14]

$$H^{xy} = \varepsilon_0^{xy} + \hbar v_F^{xy}(\sigma_x k_y - \sigma_y k_x), \tag{8}$$

where $\varepsilon_0^{xy} = C + (D_1/B_1)M$ is the Dirac point energy. $\hbar v_F^{xy} = A_2\sqrt{1-(D_1/B_1)^2}$ represents the Fermi velocity in the $(x-y)$ plane, and $\sigma_i, (i = x, y, z)$ denote the usual Pauli matrices. The $(y-z)$ plane can be described by

$$H^{yz} = \varepsilon_0^{yz} + \hbar v_F^{yz}(\sigma_y \frac{A_1}{A_2} k_z - \sigma_z k_y), \tag{9}$$

with $\varepsilon_0^{yz} = C + (D_2/B_2)M$ and $\hbar v_F^{yz} = A_2\sqrt{1-(D_2/B_2)^2}$ and the $(x-z)$ plane by

$$H^{xz} = \varepsilon_0^{xz} + \hbar v_F^{xz}(\sigma_x \frac{A_1}{A_2} k_z - \sigma_z k_x), \tag{10}$$

with $\varepsilon_0^{xz} = C + (D_2/B_2)M = \varepsilon_0^{yz}$ and $\hbar v_F^{xz} = A_2\sqrt{1-(D_2/B_2)^2} = \hbar v_F^{yz}$. Note that there is a factor $\frac{A_1}{A_2}$ in front of k_z in H^{yz} and H^{xz}. This signifies that in the $(y-z)$ and $(x-z)$ plane the topological insulator has an elliptical Dirac cone. In the $(x-y)$ plane, on the other hand, the Dirac cone is circular. In addition, this prefactor implies that the Fermi velocity in $z-$direction is different from the Fermi velocity in $x-$ and $y-$direction.
There is so far no derivation of the Hamiltonians describing the $(y-z)$ and $(x-z)$ planes published, this is why we will provide a detailed derivation in chapter 3.

Since we now have the required knowledge about topological insulators, we can continue with the theory of superconductivity which will provide us the tools to calculate the Josephson effect on the surface of topological insulators.

2.3 Superconductivity

The goal of this section is to understand the proximity-induced superconductivity in a topological insulator surface. We will begin with a short introduction to the BCS theory of superconductivity, then we derive the Bogoliubov-de-Gennes equation and finally we discuss the superconductivity for spinless fermions in 2D which can be directly related to the proximity-induced superconductivity on the surface of topological insulators.
Most of this section is based on "Introduction to Superconductivity" by M. Tinkham [15].

2.3.1 BCS theory of superconductivity

To explain the phenomenon of (type I) superconductivity, Bardeen, Cooper and Schrieffer created the BCS theory in 1957 [16]. Their theory is based on the following knowledge:

1. There is a critical temperature T_c above which the superconductor is a normal material. In the normal state ($T > T_c$) the specific heat $C(T)$ is linearly dependent on T: $C(T) = \gamma T$. For $T < T_c$, in contrast, the specific heat is dominated by an exponential dependence on T: $C(T) = \gamma T_c a e^{-bTc/T}$, where a and b are constants. This jump in the specific heat at $T = T_c$ is a second order phase transition.

2. Resistivity ρ vanishes for $T < T_c$, which also means that the electric field $\mathbf{E}$ vanishes (because the current $\mathbf{I} = \mathbf{E}/\rho$ can not be infinite).

3. Meissner effect: a superconductor is a perfect diamagnet: no magnetic field $\mathbf{B}$ can penetrate.

4. Isotope effect: the critical temperature T_c depends on the mass M of the ion, meaning superconductivity cannot be explained by electrons alone.

5. Bardeen-Pines & Fröhlich proposed a theory which states that for small energy transfers, phonon mediated electron-electron interaction can be attractive.

The last point is closely related to the problem Cooper solved: what is the ground state of two attractive electrons in the presence of a dormant Fermi sea? Let's assume, the formation of a bound pair of two electrons near the dormant Fermi sea lowers the energy. Consequently, pairs of electrons would condense until an equilibrium point is reached leading to a new ground state. As it happens, this is exactly the case. Cooper discovered these bound pairs of two electrons, therefore they are called Cooper pairs.
Since the Cooper pairs are the basis in understanding superconductivity, we want to derive them, by answering Coopers question of the ground state of two attractive electrons in the presence of a dormant Fermi sea. We start by splitting the wave function into an orbital and a spin part:

$$\Psi(\mathbf{r_1}, \mathbf{r_2}) = \psi(\mathbf{r_1}, \mathbf{r_2}) \cdot \chi(\sigma_1, \sigma_2), \tag{11}$$

where $\mathbf{r_1}$ and $\mathbf{r_2}$ are the positions of the two electrons. In the ground state we expect the total momentum to be 0, thus, we can write the orbital wave function as

$$\psi(\mathbf{r}) = \sum_{\mathbf{k}} g_{\mathbf{k}} e^{i\mathbf{kr}}, \qquad \mathbf{r} = \mathbf{r_1} - \mathbf{r_2}. \tag{12}$$

Fermionic wave functions are always antisymmetric. If we assume that the antisymmetry comes from the orbital part, we will see that $\psi(\mathbf{r}) \to 0$ for $\mathbf{r} \to 0$. Since we have attractive electrons, $\psi(0)$ should be finite. Consequently, the sign change must come from the spin part, meaning it must be in a singlet state:

$$\chi = \frac{1}{\sqrt{2}}(|\uparrow\downarrow\rangle - |\downarrow\uparrow\rangle). \tag{13}$$

With the Schrödinger equation we get

$$2E_{\mathbf{k}}\psi(\mathbf{r_1}, \mathbf{r_2}) + V(\mathbf{r_1} - \mathbf{r_2})\psi(\mathbf{r_1}, \mathbf{r_2}) = (2E_F + E)\psi(\mathbf{r_1}, \mathbf{r_2}), \tag{14}$$

where the factor 2 arises from the two electrons at the same energy. The total energy is $2E_F + E$ and E is the extra energy to the Fermi energy. Our aim is to get energy $E < 0$, such that the ground state energy is lowered by having two electrons in the presence of a dormant Fermi sea. By including the orbital wave functions we can write

$$\sum_{\mathbf{k}} 2E_{\mathbf{k}} g_{\mathbf{k}} e^{i\mathbf{kr}} + V(r) \sum_{\mathbf{k}} g_{\mathbf{k}} e^{i\mathbf{kr}} = \sum_{\mathbf{k}} (2E_F + E) g_{\mathbf{k}} e^{i\mathbf{kr}}. \tag{15}$$

Integration over the normalization volume Ω (operate $\frac{1}{\Omega}\int d^3r e^{-i\mathbf{k'r}}$ on the equation) results in

$$(E - 2\xi_{\mathbf{k}}) g_{\mathbf{k}} = \sum_{\mathbf{k'}} V_{\mathbf{kk'}} g_{\mathbf{k'}} \quad \text{with} \quad V_{\mathbf{kk'}} = \frac{1}{\Omega}\int d^3r V(r) e^{i(\mathbf{k}-\mathbf{k'})\mathbf{r}} \quad \text{and} \quad \xi_{\mathbf{k}} = E_{\mathbf{k}} - E_F. \tag{16}$$

$V_{\mathbf{kk'}}$ is the matrix element of the interaction potential. It characterizes the strength of the potential for scattering a pair of electrons with momenta ($\mathbf{k'}$, $-\mathbf{k'}$) to momenta ($\mathbf{k}$, $-\mathbf{k}$). To show the existence of a bound-pair state, we have to find a set of $g_{\mathbf{k}}$ satisfying Eq. (16). To simplify the problem, Cooper

introduced a very serviceable approximation, the "on shell" approximation, where he uses a cut-off energy $\hbar\omega_c$ to define the potential:

$$V_{\mathbf{k}\mathbf{k}'} = \begin{cases} -V & |E_{\mathbf{k}} - E_F| \leq \hbar\omega_c \text{ and } |E_{\mathbf{k}'} - E_F| \leq \hbar\omega_c, \\ 0 & \text{otherwise.} \end{cases}$$

By solving Eq. (16) for $g_{\mathbf{k}}$

$$g_{\mathbf{k}} = \frac{V}{2\xi_{\mathbf{k}} - E} \sum_{\mathbf{k}'}^{*} g_{\mathbf{k}'} \quad \text{, (where the * indicates that the summation is only over the shell,)} \tag{17}$$

and applying the summation over the shell, we finally get

$$\frac{1}{V} = \sum_{\mathbf{k}}^{*} \frac{1}{2\xi_{\mathbf{k}} - E} \approx D(E_F) \int_0^{\hbar\omega_c} d\xi \frac{1}{2\xi - E} = \frac{1}{2} D(E_F) \ln\left(\frac{E - 2\hbar\omega_c}{E}\right), \tag{18}$$

where $D(E_F)$ is the density of states at the Fermi energy. This diverges whenever $E = 2\xi_{\mathbf{k}}$. In most classic superconductors we have $D(E_F)V < 0.3$. This allows the use of the "weak-coupling approximation", which is valid for small potentials $D(E_F)V \ll 1$. The energy is then approximated by

$$E \approx -2\hbar\omega_c \exp(-\frac{2}{D(E_F)V}). \tag{19}$$

No matter how thin the shell is, there is always a negative energy solution (as the shell is around the Fermi energy and thus the Fermi energy is always in the shell). Thus, we found a bound state which lowers the energy of the system meaning that, if we want to minimize the ground state energy, we should pair up the electrons. This results in Cooper pairs, with the Cooper pair wave functions

$$\psi(r) = \sum_{\mathbf{k}} g_{\mathbf{k}} e^{i\mathbf{k}r}, \tag{20}$$

or in second quantization

$$|\psi\rangle = \sum_{|\mathbf{k}|>k_F} g_{\mathbf{k}} c^{\dagger}_{\mathbf{k}\uparrow} c^{\dagger}_{-\mathbf{k}\downarrow} |F\rangle , \tag{21}$$

where k_F is the Fermi momentum and $|F\rangle$ the Fermi sea. In this form it is obvious that pairs of time-reversed states are always occupied together. In the presence of N electrons (N is even) we have $N/2$ Cooper pairs:

$$|\psi^{(N)}\rangle = (\sum_{\mathbf{k}} g_{\mathbf{k}} c^{\dagger}_{\mathbf{k}\uparrow} c^{\dagger}_{-\mathbf{k}\downarrow})^{N/2} |vacuum\rangle . \tag{22}$$

To know this state, we need to know a large number of $g_{\mathbf{k}}$'s since there are a lot of $\mathbf{k}$ values. Because there are so many particles, BCS argued, it would be a good approximation to use a Hartree self-consistent field or mean-field approach. There the occupancy of each state $\mathbf{k}$ is taken to depend only on the average occupancy of the other states. Using this, BCS wrote the ground state:

$$|\psi_{BCS}\rangle = \Pi_{\mathbf{k}} (u_{\mathbf{k}} + v_{\mathbf{k}} c^{\dagger}_{\mathbf{k}\uparrow} c^{\dagger}_{-\mathbf{k}\downarrow}) |vacuum\rangle \quad \text{with} \quad |u_{\mathbf{k}}|^2 + |v_{\mathbf{k}}|^2 = 1. \tag{23}$$

$|v_{\mathbf{k}}|^2$ is the probability that the state $(\mathbf{k}\uparrow, -\mathbf{k}\downarrow)$ is occupied and $|u_{\mathbf{k}}|$ the probability that this state is unoccupied. This BCS ground state should minimize the energy of the system. To verify this, we use the minimal model Hamiltonian which still describes all the interactions of the system:

$$H - E_F \hat{N} = \sum_{\mathbf{k},\sigma} \xi_{\mathbf{k}} c^{\dagger}_{\mathbf{k},\sigma} c_{\mathbf{k},\sigma} + \sum_{\mathbf{k},\mathbf{k}'} V_{\mathbf{k}\mathbf{k}'} c^{\dagger}_{\mathbf{k},\uparrow} c^{\dagger}_{-\mathbf{k},\downarrow} c_{-\mathbf{k}',\downarrow} c_{\mathbf{k}',\uparrow}, \tag{24}$$

where $\hat{N}$ is the electron number operator. We want to minimize

$$\langle\psi_{BCS}| H - E_F \hat{N} |\psi_{BCS}\rangle . \tag{25}$$

By evaluating this, substituting $u_{\mathbf{k}} = \sin(\theta_{\mathbf{k}})$ and $v_{\mathbf{k}} = \cos(\theta_{\mathbf{k}})$ and taking the derivative with respect to $\theta_{\mathbf{k}}$, we finally get

$$\tan(2\theta_{\mathbf{k}}) = \frac{\sum_{\mathbf{k}'} V_{\mathbf{k}\mathbf{k}'} \sin(2\theta_{\mathbf{k}'})}{2\xi_{\mathbf{k}}} = -\frac{\Delta_{\mathbf{k}}}{\xi_{\mathbf{k}}} \tag{26}$$

with $\Delta_{\mathbf{k}} = -1/2 \sum_{\mathbf{k}'} V_{\mathbf{k}\mathbf{k}'} \sin(2\theta_{\mathbf{k}'})$ and $E_{\mathbf{k}} = \sqrt{\xi_{\mathbf{k}}^2 + \Delta_{\mathbf{k}}^2}$, which leads to $\sin(2\theta_{\mathbf{k}}) = 2u_{\mathbf{k}}v_{\mathbf{k}} = \frac{\Delta_{\mathbf{k}}}{E_{\mathbf{k}}}$ and $\cos(2\theta_{\mathbf{k}}) = v_{\mathbf{k}}^2 - u_{\mathbf{k}}^2 = -\frac{\xi_{\mathbf{k}}}{E_{\mathbf{k}}}$. This results in the BCS gap equation

$$\Delta_{\mathbf{k}} = -\frac{1}{2} \sum_{\mathbf{k}'} \frac{\Delta_{\mathbf{k}'}}{\sqrt{\xi_{\mathbf{k}'}^2 + \Delta_{\mathbf{k}'}^2}} V_{\mathbf{k}\mathbf{k}'}. \tag{27}$$

The trivial solution $\Delta_{\mathbf{k}} = 0$ of this equation describes the normal state. We are looking for nontrivial solutions, which describe the superconducting state. In the discussion of $V_{\mathbf{k}\mathbf{k}'}$, we suggested that the relevant energy is $|E_{\mathbf{k}} - E_{\mathbf{k}'}|$. To get a simple solution, we need to make the stronger restriction that $|E_{\mathbf{k}} - E_F|$ and $|E_{\mathbf{k}'} - E_F|$ are separately smaller than $\hbar\omega_c$. Inserting this $V_{\mathbf{k}\mathbf{k}'}$ in Eq. (27) we can see that this is satisfied by

$$\Delta_{\mathbf{k}} = \begin{cases} \Delta_0 & |E_{\mathbf{k}} - E_F| < \hbar\omega_c, \\ 0 & |E_{\mathbf{k}} - E_F| > \hbar\omega_c. \end{cases}$$

For this approximation the gap equation can be solved and results in

$$\Delta_0 = \frac{\hbar\omega_c}{\sinh(\frac{1}{D(E_F)V})} \overset{D(E_F)\ll 1}{\approx} 2\hbar\omega_c e^{-(VD(E_F))^{-1}}, \tag{28}$$

where $D(E_F) \ll 1$ means that the attractive interaction is very small. We find that $\Delta_0 \ll \hbar\omega_c \ll E_F$, $v_{\mathbf{k}}^2 = \frac{1}{2}(1 - \frac{\xi_{\mathbf{k}}}{E_{\mathbf{k}}})$ and $u_{\mathbf{k}}^2 = \frac{1}{2}(1 + \frac{\xi_{\mathbf{k}}}{E_{\mathbf{k}}})$.

After this brief introduction to the BCS theory of superconductivity we want to present equations which are very suitable to calculate systems with superconducting regions. These equations are the so-called Bogoliubov-de-Gennes equations.

2.3.2 Bogoliubov-de-Gennes (BdG) equations

The BdG equations are convenient equations in which the direct relation between the electron and hole wave functions of a system can be seen. In this chapter we derive the BdG equations in real space. This derivation is also applicable in the presence of a magnetic field. The method presented is a generalization of the Hartree-Fock equations to the case of superconductivity. It was first published in the book "Superconductivity of Metals and Alloys" from Pierre de Gennes [17] and this chapter is based on this book.

At first we write the Hamiltonian of the electron system. The operators $\Psi(\mathbf{r}\sigma)$ and $\Psi^\dagger(\mathbf{r}\sigma)$ are defined as

$$\begin{aligned} \Psi(\mathbf{r}\sigma) &= e^{i\mathbf{k}\mathbf{r}} c_{r\sigma}, \\ \Psi^\dagger(\mathbf{r}\sigma) &= e^{-i\mathbf{k}\mathbf{r}} c_{r\sigma}^\dagger, \end{aligned} \tag{29}$$

where $\sigma = \uparrow, \downarrow$ is the spin index. They satisfy the anticommutation relations $\{\Psi(\mathbf{r_1}\sigma_1), \Psi(\mathbf{r_2}\sigma_2)\} = \{\Psi^\dagger(\mathbf{r_1}\sigma_1), \Psi^\dagger(\mathbf{r_2}\sigma_2)\} = 0$ and $\{\Psi^\dagger(\mathbf{r_1}\sigma_1), \Psi(\mathbf{r_2}\sigma_2)\} = \delta_{\sigma_1\sigma_2}\delta(\mathbf{r_1} - \mathbf{r_2})$. In terms of $\Psi(\mathbf{r}\sigma)$ and $\Psi^\dagger(\mathbf{r}\sigma)$ we can write the Hamiltonian $\mathcal{H}$ as

$$\mathcal{H} = \sum_\sigma \int \Psi^\dagger(\mathbf{r}\sigma) H(\mathbf{r}) \Psi(\mathbf{r}\sigma) d\mathbf{r} \tag{30}$$

H is the electron Hamiltonian defined in the section before. As in the book of de Gennes we can write the electron Hamiltonian with the vector potential $\mathbf{A}$ and the spin independent potential $U_0(\mathbf{r})$:

$$H(\mathbf{r}) = \frac{1}{2m}\left(-i\hbar\nabla - \frac{e\mathbf{A}}{c}\right)^2 + U_0(\mathbf{r}) - E_F, \tag{31}$$

with the charge of the electron e and the velocity of light c. We include an interaction by adding an average potential which acts only on one particle at a time. Thus, we insert a potential U and a pairing potential $\Delta(\mathbf{r})$ and we get the effective Hamiltonian $\mathcal{H}_{\text{eff}}$

$$\mathcal{H}_{\text{eff}} = \int \left(\sum_{\sigma} \Psi^{\dagger}(\mathbf{r}\sigma) H(\mathbf{r}) \Psi(\mathbf{r}\sigma) + U(\mathbf{r}) \Psi^{\dagger}(\mathbf{r}\sigma) \Psi(\mathbf{r}\sigma) \right) + \Delta(\mathbf{r}) \Psi^{\dagger}(\mathbf{r}\uparrow) \Psi^{\dagger}(\mathbf{r}\downarrow) + \Delta^{*}(\mathbf{r}) \Psi(\mathbf{r}\downarrow) \Psi(\mathbf{r}\uparrow) d\mathbf{r}. \tag{32}$$

We aim to determine the eigenstates of $\mathcal{H}_{\text{eff}}$. The Hamiltonian is diagonalized by performing a unitary transformation:

$$\begin{aligned} \Psi(\mathbf{r}\uparrow) &= \sum_{n} (\gamma_{n\uparrow} u_n(\mathbf{r}) - \gamma_{n\downarrow}^{\dagger} v_n^{*}(\mathbf{r})), \\ \Psi(\mathbf{r}\downarrow) &= \sum_{n} (\gamma_{n\downarrow} u_n(\mathbf{r}) + \gamma_{n\uparrow}^{\dagger} v_n^{*}(\mathbf{r})). \end{aligned} \tag{33}$$

$\gamma_{n\sigma}$ and $\gamma_{n\sigma}^{\dagger}$ are new operators which also satisfy the fermion anticommutation relations. The transformation has to diagonalize the effective Hamiltonian, such that

$$\mathcal{H}_{\text{eff}} = E_g + \sum_{n\sigma} \varepsilon_n \gamma_{n\sigma}^{\dagger} \gamma_{n\sigma}. \tag{34}$$

E_g is the ground state energy and ε_n is the energy of the excitation n. By taking the commutator we get

$$\begin{aligned} [\mathcal{H}_{\text{eff}}, \gamma_{n\sigma}] &= -\varepsilon_n \gamma_{n\sigma}, \\ [\mathcal{H}_{\text{eff}}, \gamma_{n\sigma}^{\dagger}] &= \varepsilon_n \gamma_{n\sigma}^{\dagger}. \end{aligned} \tag{35}$$

We also calculate the commutators

$$\begin{aligned} [\Psi(\mathbf{r}\uparrow), \mathcal{H}_{\text{eff}}] &= [H + U(\mathbf{r})] \Psi(\mathbf{r}\uparrow) + \Delta(\mathbf{r}) \Psi^{\dagger}(\mathbf{r}\downarrow), \\ [\Psi(\mathbf{r}\downarrow), \mathcal{H}_{\text{eff}}] &= [H + U(\mathbf{r})] \Psi(\mathbf{r}\downarrow) - \Delta^{*}(\mathbf{r}) \Psi^{\dagger}(\mathbf{r}\uparrow). \end{aligned} \tag{36}$$

By replacing the Ψ operators by the Eqs. (33) and using the anticommutation relations of the fermions and the commutation relations of Eq. (35) and finally by comparing the coefficients of γ_n and $\gamma_n^{\dagger}$ we get the Bogoliubov equations:

$$\varepsilon \begin{pmatrix} u(\mathbf{r}) \\ v(\mathbf{r}) \end{pmatrix} = \begin{pmatrix} [H + U(\mathbf{r})] & \Delta(\mathbf{r}) \\ \Delta^{*}(\mathbf{r}) & -[H + U(\mathbf{r})]^{*} \end{pmatrix} \begin{pmatrix} u(\mathbf{r}) \\ v(\mathbf{r}) \end{pmatrix}. \tag{37}$$

It can be seen that the BdG equations take the same form for both spins. Thus, we can write them in a Nambu basis where the spins are included:

$$\varepsilon \begin{pmatrix} \psi_{\uparrow} \\ \psi_{\downarrow} \\ \psi_{\uparrow}^{\dagger} \\ \psi_{\downarrow}^{\dagger} \end{pmatrix} = \begin{pmatrix} H_0(\mathbf{r}) & \mathbf{\Delta}(\mathbf{r}) \\ -\mathbf{\Delta}(\mathbf{r}) * & -H_0^{*}(\mathbf{r}) \end{pmatrix} \begin{pmatrix} \psi_{\uparrow} \\ \psi_{\downarrow} \\ \psi_{\uparrow}^{\dagger} \\ \psi_{\downarrow}^{\dagger} \end{pmatrix}. \tag{38}$$

H_0 is the free fermion Hamiltonian. For p-wave superconductivity in 2D (which we will get when using the proximity effect on the surface of a topological superconductor, as explained later) we have the gap matrix $\mathbf{\Delta}(\mathbf{r}) = \Delta i\sigma_y$ where $\Delta = \Delta_0 e^{i\phi}$ is independent of $\mathbf{r}$ [18]. In the Nambu basis which we use in this project, the BdG equations take the form:

$$\varepsilon \begin{pmatrix} \psi_{\uparrow} \\ \psi_{\downarrow} \\ \psi_{\downarrow}^{\dagger} \\ -\psi_{\uparrow}^{\dagger} \end{pmatrix} = \begin{pmatrix} H_0(\mathbf{r}) & \mathbf{\Delta} \\ -\mathbf{\Delta}^{*} & -\sigma_y H_0^{*}(\mathbf{r}) \sigma_y \end{pmatrix} \begin{pmatrix} \psi_{\uparrow} \\ \psi_{\downarrow} \\ \psi_{\downarrow}^{\dagger} \\ -\psi_{\uparrow}^{\dagger} \end{pmatrix} = \begin{pmatrix} H_0(\mathbf{r}) & \mathbf{\Delta} \\ \mathbf{\Delta}^{*} & -\mathcal{T} H_0(\mathbf{r}) \mathcal{T}^{-1} \end{pmatrix} \begin{pmatrix} \psi_{\uparrow} \\ \psi_{\downarrow} \\ \psi_{\downarrow}^{\dagger} \\ -\psi_{\uparrow}^{\dagger} \end{pmatrix} = \mathbf{H}(\mathbf{r}) \begin{pmatrix} \psi_{\uparrow} \\ \psi_{\downarrow} \\ \psi_{\downarrow}^{\dagger} \\ -\psi_{\uparrow}^{\dagger} \end{pmatrix}, \tag{39}$$

with the gap matrix $\Delta = \Delta_0 e^{i\phi} \cdot \mathbb{I}_{2\times 2}$ and the TR operator $\mathcal{T} = i\sigma_y K$ (more details in Appendix A). Furthermore, we will identify this basis with electron and hole wave functions: $(\psi_{\uparrow}, \psi_{\downarrow}, \psi_{\downarrow}^{\dagger}, -\psi_{\uparrow}^{\dagger})^{\intercal} = (\Psi_e, \Psi_h)^{\intercal}$. Solving the BdG equations leads to two sets of energy eigenstates, because with the Nambu

states, we have artificially doubled the dimension of the Hamiltonian and consequently also doubled the number of eigenstates. The solutions with negative energies would represent electrons with $k < k_F$ and holes with $k > k_F$, which contradicts the conventional definition of electrons and holes in a normal metal. Therefore it is usual to use only positive energy solutions, which represent a complete set of solutions. Since the number of independent solutions remains the same, there must be a symmetry relation between the eigenstates. This symmetry is the particle-hole symmetry.
In principle there are two very important symmetries: the TR symmetry and the particle-hole symmetry. They are explained in detail in Appendix A.

So far we discussed superconductivity for normal Dirac fermions with spin-1/2. What happens if we assume spinless fermions?

2.3.3 Superconductivity for spinless fermions in 2D

Superconductivity for spinless fermions has a certain importance for this work, as the topological superconducting state which we receive due to the proximity of a s-wave superconductor to the topological insulator resembles the spinless $p_x + ip_y$ topological superconductor. Still, there are some differences, which will be explained in the section about topological superconductors.
As it is not obvious that superconductivity is possible for spinless particles, we want to derive it here. This chapter is adapted from a review by Read and Green [19]. We start with the Hamiltonian which describes the 2D system of spinless fermions:

$$H = \sum_{\mathbf{k}} (\xi_{\mathbf{k}} c_{\mathbf{k}}^\dagger c_{\mathbf{k}} + \frac{1}{2}(\Delta_{\mathbf{k}}^* c_{-\mathbf{k}} c_{\mathbf{k}} + \Delta_{\mathbf{k}} c_{\mathbf{k}}^\dagger c_{-\mathbf{k}}^\dagger). \tag{40}$$

$\xi_{\mathbf{k}} = \frac{\mathbf{k}^2}{2m} - \mu$ is the energy for free fermions and μ is the chemical potential (which is equal to the Fermi energy E_F at temperature $T = 0$). The spinless fermions also fulfill the anticommutation relations. With spinless particles we have the problem that for a constant gap $\Delta_{\mathbf{k}} = \Delta$ we don't have any pairing:

$$\Delta^* c_{-\mathbf{k}} c_{\mathbf{k}} = \frac{\Delta^*}{2L^2} \int d\mathbf{r} d\mathbf{r}' \psi(\mathbf{r}) \psi(\mathbf{r}') \sum_{\mathbf{k}} e^{-i(-\mathbf{k})\mathbf{r}} e^{-i(\mathbf{k})\mathbf{r}'} = \frac{\Delta^*}{2} \int d\mathbf{r} \psi(\mathbf{r}) \psi(\mathbf{r}) = 0, \tag{41}$$

where L^2 is the volume of the two dimensional system. This problem can be solved by using a $\mathbf{k}-$dependent pairing potential. There are several symmetries which the pairing potential can have. A superconductor with a constant gap $\Delta_{\mathbf{k}} = \Delta$ is called s-wave superconductor. In 2D, the simplest nontrivial pairing is the so-called p-wave superconductor where $\Delta_{\mathbf{k}} = \Delta(k_x \pm ik_y)$. With such a pairing potential the Hamiltonian is not invariant under parity and TR symmetry anymore.
To diagonalize the Hamiltonian, we introduce the Nambu spinors $\psi_{\mathbf{k}} = \begin{pmatrix} c_{\mathbf{k}} \\ c_{-\mathbf{k}}^\dagger \end{pmatrix}$ and $\psi_{\mathbf{k}}^\dagger = \begin{pmatrix} c_{\mathbf{k}}^\dagger \\ c_{-\mathbf{k}} \end{pmatrix}$. As a further simplification we use: $\xi_{\mathbf{k}} c_{\mathbf{k}}^\dagger c_{\mathbf{k}} = \xi_{\mathbf{k}}(-c_{\mathbf{k}} c_{\mathbf{k}}^\dagger + 1) \overset{\text{drop constant part}}{\rightarrow} -\xi_{\mathbf{k}} c_{\mathbf{k}} c_{\mathbf{k}}^\dagger$, since constant parts do not change the physics of the system. The Hamiltonian of Eq. (40) can now be rewritten in terms of the Nambu spinors:

$$H = \frac{1}{2} \sum_{\mathbf{k}} \psi_{\mathbf{k}}^\dagger \begin{pmatrix} \xi_{\mathbf{k}} & \Delta_{\mathbf{k}} \\ \Delta_{\mathbf{k}}^* & -\xi_{\mathbf{k}} \end{pmatrix} \psi_{\mathbf{k}}, \tag{42}$$

with the eigenvalues $E_{\mathbf{k}} = \pm\sqrt{\xi_{\mathbf{k}}^2 + |\Delta_{\mathbf{k}}|^2}$. We diagonalize the Hamiltonian by doing a Bogoliubov transformation: $\alpha_{\mathbf{k}} = u_{\mathbf{k}} c_{\mathbf{k}} - v_{\mathbf{k}} c_{-\mathbf{k}}^\dagger$ and $\alpha_{\mathbf{k}}^\dagger = u_{\mathbf{k}}^* c_{\mathbf{k}}^\dagger - v_{\mathbf{k}}^* c_{-\mathbf{k}}$. By demanding that these two quasiparticles should fulfill anticommutation relations we get the condition $|u_{\mathbf{k}}|^2 + |v_{\mathbf{k}}|^2 = 1$. In terms of the Bogoliubov particles the diagonalized Hamiltonian is $H = \sum_{\mathbf{k}} E_{\mathbf{k}} \alpha_{\mathbf{k}}^\dagger \alpha_{\mathbf{k}}$. For $u_{\mathbf{k}}$ and $v_{\mathbf{k}}$ we get equations, the BdG equations, that have to be fulfilled:

$$E_{\mathbf{k}} u_{\mathbf{k}} = \xi_{\mathbf{k}} u_{\mathbf{k}} - \Delta_{\mathbf{k}}^* v_{\mathbf{k}}, \tag{43}$$

$$E_{\mathbf{k}} v_{\mathbf{k}} = -\xi_{\mathbf{k}} v_{\mathbf{k}} - \Delta_{\mathbf{k}} u_{\mathbf{k}}. \tag{44}$$

The solutions are

$$\frac{v_{\mathbf{k}}}{u_{\mathbf{k}}} = -\frac{E_{\mathbf{k}} - \xi_{\mathbf{k}}}{\Delta_{\mathbf{k}}^*}, \qquad |u_{\mathbf{k}}|^2 = \frac{1}{2}(1 + \frac{\xi_{\mathbf{k}}}{E_{\mathbf{k}}}), \qquad |v_{\mathbf{k}}|^2 = \frac{1}{2}(1 - \frac{\xi_{\mathbf{k}}}{E_{\mathbf{k}}}). \tag{45}$$

We can see that if $u_{\mathbf{k}}$ and $v_{\mathbf{k}}$ are solutions, $e^{i\phi_{\mathbf{k}}}u_{\mathbf{k}}$ and $e^{i\phi_{\mathbf{k}}}v_{\mathbf{k}}$ are solutions as well.
The ground state can be written as

$$|\psi\rangle = (\Pi_{\mathbf{k}}|u_{\mathbf{k}}|^{1/2})e^{\frac{1}{2}(\sum_{\mathbf{k}} g_{\mathbf{k}}c^{\dagger}_{\mathbf{k}}c^{\dagger}_{-\mathbf{k}})}\,|vacuum\rangle \text{ with } g_{\mathbf{k}} = \frac{v_{\mathbf{k}}}{u_{\mathbf{k}}} = -\frac{E_{\mathbf{k}} - \xi_{\mathbf{k}}}{\Delta^{*}_{\mathbf{k}}}. \tag{46}$$

We can expand the exponential function and because of the Pauli principle all higher order terms vanish and we get

$$|\psi\rangle = (\Pi_{\mathbf{k}}|u_{\mathbf{k}}|^{1/2})\Pi_{\mathbf{k}}(1 + g_{\mathbf{k}}c^{\dagger}_{\mathbf{k}}c^{\dagger}_{-\mathbf{k}})\,|vacuum\rangle\,. \tag{47}$$

For p-wave superconductivity we have $\Delta \to 0$ for $\mathbf{k} \to 0$ and thus $E_{\mathbf{k}} - |\xi_{\mathbf{k}}| \to 0$ for $\mathbf{k} \to 0$. Hence, we have three options for $\mathbf{k} \to 0$:

- strong-pairing phase when $\mu < 0$ which implies $\xi_{\mathbf{k}} > 0$:
  This leads to $g_{\mathbf{k}} \propto \frac{\Delta}{2}(k_x - ik_y) \overset{\mathbf{k}\to 0}{\to} 0$ and in real space $g(\mathbf{r}) \propto e^{-\mathbf{r}/\mathbf{r}_0}$ for $\mathbf{r} \to \infty$ which means that the wave functions of the Cooper pairs are exponentially localized and the Cooper pairs are strongly bound.

- weak-pairing phase when $\mu > 0$ which implies $\xi_{\mathbf{k}} < 0$:
  This leads to $g_{\mathbf{k}} \propto -\frac{2\mu}{\Delta}\frac{1}{k_x - ik_y} \overset{\mathbf{k}\to 0}{\to} \infty$ and in real space $g(\mathbf{r}) \propto \frac{1}{x+iy}$ for $\mathbf{r} \to \infty$ which means that the wave functions decay very slowly and the Cooper pairs are weakly bound. The weak-pairing phase does not require that the coupling is weak, but that it is continuously connected to the weak coupling BCS region.

- weak-strong transition when $\mu = 0$ which implies $\xi_{\mathbf{k}} = 0$:
  At small $\mathbf{k}$ we find $g_{\mathbf{k}} = \frac{k_x - ik_y}{|\mathbf{k}|}$ and in real space $g(\mathbf{r}) \propto \frac{1}{(x+iy)|x+iy|}$ for $\mathbf{r} \to \infty$. This shows a mixed behaviour of the two former cases.

Apparently, depending on the sign of the chemical potential μ, we have different phases. As soon as $\mu \neq 0$ we get a gapped spectrum. We will see that, if $\mu < 0$ (strong-pairing phase) we have a topological trivial superconductor which can be adiabatically transformed into an insulator, like vacuum. For $\mu > 0$ (weak-pairing phase) this is not possible and we have a topologically nontrivial state. We call this a p-wave superconductor. To analyze consequences of this new state, we calculate the BdG equations in position and time representation.

BdG equations in position and time representation

We write the wave functions in position and time representation and we use $\xi_{\mathbf{k}} \simeq -\mu < 0$ (weak-pairing phase) and

$$\begin{aligned} u(\mathbf{r},t) &= \sum_{\mathbf{k}} e^{i\mathbf{k}\mathbf{r} - iE_{\mathbf{k}}t}u_{\mathbf{k}}, \\ v(\mathbf{r},t) &= \sum_{\mathbf{k}} e^{i\mathbf{k}\mathbf{r} - iE_{\mathbf{k}}t}v_{\mathbf{k}}. \end{aligned} \tag{48}$$

The BdG equations now become

$$\begin{aligned} i\frac{\partial u(\mathbf{r},t)}{\partial t} &= -\mu u(\mathbf{r},t) + i\Delta^{*}(\frac{\partial}{\partial x} + i\frac{\partial}{\partial y})v(\mathbf{r},t), \\ i\frac{\partial v(\mathbf{r},t)}{\partial t} &= \mu u(\mathbf{r},t) + i\Delta(\frac{\partial}{\partial x} - i\frac{\partial}{\partial y})u(\mathbf{r},t). \end{aligned} \tag{49}$$

These two equations are compatible with $u(\mathbf{r},t) = v^{*}(\mathbf{r},t)$ $(*)$. This has consequences for the Bogoliubov quasiparticles $\alpha_{\mathbf{k}}$:

$$\alpha(\mathbf{r},t) = \sum_{\mathbf{k}} e^{i\mathbf{k}\mathbf{r} - iE_{\mathbf{k}}t}\alpha_{\mathbf{k}} = \sum_{\mathbf{k}} e^{i\mathbf{k}\mathbf{r} - iE_{\mathbf{k}}t}(u_{\mathbf{k}}c_{\mathbf{k}} - v_{\mathbf{k}}c^{\dagger}_{-\mathbf{k}}) \tag{50}$$

We use the Fourier transformation for fermions $c_{\mathbf{k}} = \frac{1}{L}\int d^2r e^{-i\mathbf{k}\mathbf{r}}c(r)$, include $(*)$ and finally get our Bogoliubov quasiparticle in position and time space:

$$\alpha(\mathbf{r},t) = \frac{1}{L}\int dr'(u(\mathbf{r}-\mathbf{r}')c(\mathbf{r}') - u^{*}(\mathbf{r}-\mathbf{r}')c^{\dagger}(\mathbf{r}')). \tag{51}$$

Thus, we have $\alpha^\dagger(\mathbf{r},t) = -\alpha(\mathbf{r},t)$. Now we can define a fermionic state which is its own antiparticle: $\gamma(\mathbf{r},t) = i\alpha(\mathbf{r},t) \to \gamma^\dagger = \gamma$. Such a particle is called a Majorana fermion. More about these Majorana fermions is explained later. At this point it is only important to see, that Majorana fermions can appear as a solution of the BdG equations. This raises the question, where they can appear as solutions. One example is at the edge of a weak-pairing phase superconductor and a strong-pairing phase superconductor.

Edge of a weak- and a strong-pairing phase superconductor

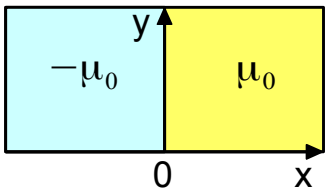

Figure 6: Edge of a topological nontrivial weak-pairing phase superconductor ($\mu = \mu_0 > 0$) and a strong-pairing phase superconductor ($\mu = -\mu_0 < 0$).

Figure 6 shows the system we want to calculate. We have a chemical potential $\mu(x)$ which is dependent on x: for $x < 0$ we have $\mu(x) = -\mu_0 < 0$ and for $x > 0$ we have $\mu(x) = \mu_0 > 0$. A change in sign across a line represents a domain wall between the weak and strong-pairing phases and $\mu = 0$ is the point at which the transition occurs. The weak-pairing phase is nontrivial and it makes sense to capture the generic properties of an edge by a domain wall. The strong pairing phase, on the other hand, has the same topology as the vacuum and can be continuously connected to it. Therefore the strong-pairing phase does not need to have a domain wall. In a next step we want to solve the BdG equations. We consider solutions with definite k_y. At first we set $k_y = 0$ and $E_k = 0$:

$$i\Delta\frac{\partial v_0}{\partial x} = \mu(x)u_0, \qquad i\Delta\frac{\partial u_0}{\partial x} = -\mu(x)v_0. \tag{52}$$

u_0 and v_0 are the wave functions at $k_y = 0$ and $E_\mathbf{k} = 0$. To solve the equation we use the Ansatz $v_0 = iu_0$.

$$-\Delta\frac{\partial u_0}{\partial x} - \mu(x)u_0 = 0 \tag{53}$$

has a unique normalizable solution ($\mu(x) \overset{x\to\infty}{\to} 0$): $u_0(x) = e^{-i\pi/4}e^{-\frac{1}{\Delta}\int_0^x dx'\mu(x')}$. This state satisfies $u_0^* = v_0 = iu_0$ and for $|x| \to \infty$, $u_0(x)$ is exponentially suppressed, thus, the state is bound in $x-$direction. We have found a Majorana fermion. It is time independent, as it is a zero energy solution. Next we assume finite k_y and a small energy $E_\mathbf{k} = -\Delta k_y$. The BdG equations become

$$\begin{aligned} E_\mathbf{k}u_{k_y} &= -\mu(x)u_{k_y} + i\Delta(\frac{\partial v_{k_y}}{\partial k_y} - k_y v_{k_y}), \\ E_\mathbf{k}v_{k_y} &= \mu(x)v_{k_y} + i\Delta(\frac{\partial u_{k_y}}{\partial k_y} + k_y u_{k_y}). \end{aligned} \tag{54}$$

We can find bound states in $x-$ direction, meaning they are bound to the domain wall:

$$u_{k_y}(x,y,t) = u_{k_y}(x)e^{ik_y y + i\Delta k_y t} = u_{k_y}(x)e^{ik_y(y+\Delta t)}. \tag{55}$$

This state is propagating in time along the domain wall in one direction. This is only possible, because parity and TR symmetry are broken.

Vortices in p-wave superconductors

A vortex in a superconductor is a topological defect. Such vortices can be created by bringing the superconductor into a magnetic field. The magnetic flux then flows through vortices. We will only take into

account vortices of minimal flux which is half-flux quantum. We can consider a vortex as a small circular edge with vacuum at the center. If we have vortices in the strong-pairing phase, we expect nothing interesting to happen. In the weak-pairing phase, on the contrary, we must include a concentric circular domain wall to separate the vacuum at the center of the vortex from the weak-pairing phase outside.

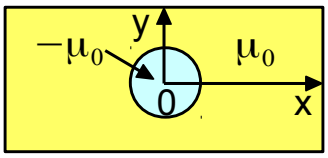

Figure 7: Vortex in a weak-pairing phase superconductor ($\mu = \mu_0 > 0$). At the core of the vortex the chemical potential is $\mu = -\mu_0 < 0$. The circle signals the domain wall which corresponds to the phase transition with $\mu = 0$.

We want to study what is happening on the boundary of a vortex with strong-pairing phase in a weak-pairing phase superconductor. The setting is shown in Fig. 7. We write the BdG equations for a single vortex and for $E = 0$ in polar coordinates $r = \sqrt{x^2 + y^2}$ and $\theta = \arctan\left(\frac{y}{x}\right)$:

$$i\Delta e^{i\theta}\left(\frac{\partial}{\partial r} + \frac{i}{r}\frac{\partial}{\partial \theta}\right) v = \mu u, \tag{56}$$

$$i\Delta e^{-i\theta}\left(\frac{\partial}{\partial r} + -\frac{i}{r}\frac{\partial}{\partial \theta}\right) u = -\mu v, \tag{57}$$

with the boundary conditions $u(r, \theta + 2\pi) = -u(r, \theta)$ and $v(r, \theta + 2\pi) = -v(r, \theta)$. For $r \to \infty$ we have $\mu \to \mu_0 > 0$ (weak-pairing phase), and for $r \to 0$ we have $\mu \to -\mu_0$. We can get normalizable solutions of the form

$$u = (i(x - iy))^{-1/2} f(r) \qquad \text{and} \qquad v = (-i(x + iy))^{-1/2} f(r) = u^*, \tag{58}$$

where $f(r)$ is a real function which fulfills

$$\frac{\partial f(r)}{\partial r} = -\mu(r)\frac{f(r)}{\Delta} \text{ with solution } f(r) \propto e^{-\int_0^r dr' \mu(r')/\Delta}. \tag{59}$$

Finally, we found a Majorana state bound to the vortex core. This was calculated at $E = 0$. This should, like in the edge case, persist when we relax our assumptions, as long as the bulk outside the vortex is in the weak-pairing phase.

The main problem about this weak-pairing phase p-wave superconductor is, that it does not exist in real materials. Nevertheless, if we bring a s-wave superconductor near to the surface of a topological insulator, we receive a surface state which resembles the spinless $p_x + ip_y$ topological superconductor.

2.3.4 Proximity-induced superconductivity on the surface of a topological insulator

When we put a superconductor on top of the surface of a topological insulator, Cooper pairs may tunnel from the superconductor to the surface of the topological insulator. This results in an induced superconducting energy gap in the surface states. Here we use a s-wave superconductor which we bring on top of our Bi_2Se_3 topological insulator. The resulting superconducting state resembles the spinless $p_x + ip_y$ superconductor. In contrast to the spinless superconductor, the topological superconductor we get does not violate TR symmetry, and its Cooper pairs have even parity. In this section we want to describe what happens, when the superconductor is brought near to the topological insulator, and we want to show, how it is related to the spinless $p_x + ip_y$ superconductor. The following argumentation is based on Ref. [20].
We start with the TR invariant surface Hamiltonians H^p where $p = xy, yz, xz$ refers to the different

surface planes of the Bi_2Se_3 topological insulator. We write the Hamiltonian with the electron field operators $(\psi_\uparrow, \psi_\downarrow)^\intercal$:

$$H_0 = \begin{pmatrix} \psi_\uparrow^\dagger \\ \psi_\downarrow^\dagger \end{pmatrix} (H^p - \mu) \begin{pmatrix} \psi_\uparrow \\ \psi_\downarrow \end{pmatrix}. \tag{60}$$

Next we suppose that an s-wave superconductor is deposited on the surface. If there is a good interface between the topological insulator and the superconductor, electrons tunnel between these two systems. The electrons in the topological insulator then feel an effective proximity-induced superconducting pairing field. We include the pairing effect in the topological insulator by adding $V = \Delta\psi_\uparrow^\dagger\psi_\downarrow^\dagger + \Delta^\dagger\psi_\downarrow\psi_\uparrow$, where $\Delta = \Delta_0 e^{i\phi}$, to the phenomenological Hamiltonian H_0. Eventually, we write the total Hamiltonian $\mathbf{H}$ in Nambu basis:

$$\mathbf{H} = \frac{1}{2} \begin{pmatrix} \psi_\uparrow \\ \psi_\downarrow \\ \psi_\downarrow^\dagger \\ -\psi_\uparrow^\dagger \end{pmatrix}^\dagger \mathbf{H^s} \begin{pmatrix} \psi_\uparrow \\ \psi_\downarrow \\ \psi_\downarrow^\dagger \\ -\psi_\uparrow^\dagger \end{pmatrix}, \tag{61}$$

$$\mathbf{H^s} = \begin{pmatrix} (H^p - \mu) & \mathbf{\Delta} \\ \mathbf{\Delta}^* & -\mathcal{T}(H^p - \mu)\mathcal{T}^{-1} \end{pmatrix}, \tag{62}$$

where $\Delta = \Delta_0 e^{i\phi} \cdot \mathbb{I}_{2\times 2}$. The excitation spectrum of this system is $\varepsilon_{\mathbf{k}} = \pm\sqrt{|\Delta_0|^2 + (\mu \pm \hbar v_F|\mathbf{k}|)^2}$, where v_F is the Fermi velocity of the corresponding surface and $\mathbf{k}$ the two dimensional momentum of the surface. Owing to the TR invariance of the surface Hamiltonian, the second diagonal element equals $-\mathcal{T}(H^p - \mu)\mathcal{T}^{-1} = -(H^p - \mu)$. For $\mu \gg \Delta_0$ the low energy spectrum resembles that of a spinless $p_x + ip_y$ superconductor. We can compare the Hamiltonian $\mathbf{H^s}$ to that of Eq. (42). Apparently, it is formally equivalent to a spinless $p_x + ip_y$ superconductor, but in contrast to the spinless superconductor, $\mathbf{H^s}$ is still TR invariant.

We have already shown that in 2D spinless $p_x \pm ip_y$ superconductors Majorana bound states can be found. With the proximity-induced superconductivity on the surface of topological insulators we found an existent system which resembles that of a $p_x + ip_y$. In contrast to the Hamiltonian of a p-wave superconductor, the Hamiltonian of the proximity-induced superconducting surface is TR invariant. To enable the existence of Majorana fermions, we need to bring the superconducting surface into contact with a surface which is described by a Hamiltonian which breaks TR symmetry. The edge of these two surfaces then may host a Majorana. One option to create a TR breaking surface state is proximity-induced ferromagnetism.

2.3.5 Proximity-induced ferromagnetism on the surface of a topological insulator

By placing a ferromagnetic insulator on top of the topological insulator, the topological insulator becomes a ferromagnetic insulator due to the exchange coupling [21]. This is called the magnetic proximity effect. The Hamiltonian for the surface of a topological ferromagnet reads:

$$\mathbf{H^f} = \begin{pmatrix} H^p - \mu + m_x\sigma_x + m_y\sigma_y + m_z\sigma_z & 0 \\ 0 & -H^p + \mu + m_x\sigma_x + m_y\sigma_y + m_z\sigma_z \end{pmatrix}, \tag{63}$$

where H^p, $p = xy, yz, xz$, is the surface Hamiltonian of the topological insulator. The ferromagnetic contribution is $\mathbf{M} = \mathbf{m} \cdot \sigma$, where $\mathbf{m} = (m_x, m_y, m_z)$ is an exchange field. If the magnetization $\mathbf{M}$ is perpendicular to the surface, the magnetization opens up a gap. For instance, we consider the $(x-y)$ plane ($H^p = H^{xy}$) and put a ferromagnet on top, which induces a perpendicular magnetization, $\mathbf{m} \cdot \sigma = (0, 0, m_z)^\intercal \cdot \sigma$. The band dispersion becomes $\varepsilon = \pm\hbar v_F^{xy}\sqrt{k_x^2 + k_y^2 + m_z^2} - \mu + \varepsilon_0^{xy}$, thus no energy states with $|\varepsilon| < |m_z|$ exist, meaning m_z opens up a gap. The property making the ferromagnetic insulator interesting is, that it breaks TR symmetry, as it can be seen from the form of $\mathbf{H^f}$. We recall from the section about superconductivity for spinless fermions in 2D, that we can find Majorana fermions on edges of a topological superconductor to a topologically trivial state, if parity and TR symmetry are broken. Indeed, it has been calculated that the edge between a topological superconductor and a topological ferromagnet can host Majorana fermions [20].
Since we are eventually able to establish a system which may host Majorana fermions, we are interested in the properties of of these fermions.

2.3.6 Majorana bound states

In this section we briefly explain some of the characteristics of Majorana fermions and conclude by explaining, why they are so interesting to the physical community. The content is based on the review [22] about topological superconductivity and Majorana fermions.
Majorana fermions are fermionic particles, which are their own antiparticles. Thus, their annihilation operator γ is equal to their creation operator $\gamma^\dagger$. Isolated Majorana fermions may occur, for instance, in vortices and on edges of effectively spinless superconducting systems with triplet pairing symmetry (p-wave superconductivity). In two dimensions this means $p_x \pm ip_y$ pairing symmetry.

In a sense a Majorana fermion is half of a normal fermion since a fermionic operator c_i on site i can be written as a superposition of two Majorana operators $\gamma_{i,1}$, $\gamma_{i,2}$ on site i: $c_i = \frac{1}{2}(\gamma_{i,1} + i\gamma_{i,2})$, $c_i^\dagger = \frac{1}{2}(\gamma_{i,1} - i\gamma_{i,2})$. In a one dimensional system this can be easily sketched in terms of a so-called Kitaev's chain, as it is shown in Fig. 8.

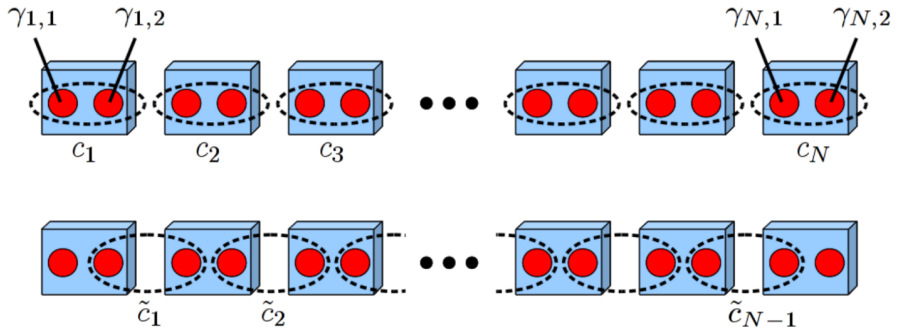

Figure 8: Kitaev's 1D p-wave superconducting tightbinding chain. Upper panel: the fermion operators c_i on each site i can be split into two Majorana operators $\gamma_{i,1}$ and $\gamma_{i,2}$. Lower panel: fermion operators $\tilde{c}_i$ are created by combining Majorana operators on neighboring sites $\gamma_{i+1,1}$ and $\gamma_{i,2}$. This leaves two unpaired Majorana operators $\gamma_{1,1}$ and $\gamma_{N,2}$. Adapted from Ref. [22].

Usually – when the two Majorana fermions are spatially localized close to each other and overlap such that they cannot be addressed individually – this is only a mathematical operation without physical consequences. But here we talk about Majorana fermions which are spatially separated like $\gamma_{1,1}$ and $\gamma_{N,2}$ in the lower panel of Fig. 8. Such a state is protected from most types of decoherence since it cannot be changed by local perturbations that only affect one of the Majoranas forming the fermion. We can write the Majoranas in terms of the fermionic operators: $\gamma_{i,1} = c_i + c_i^\dagger$ and $\gamma_{i,2} = i(c_i^\dagger - c_i)$. They satisfy the anticommutation relation $\{\gamma_{i,p}, \gamma_{j,q}\} = 2\delta_{i,j}\delta_{p,q}$ and we can see that $\gamma_i^2 = 1$. When we construct a "Majorana number operator" $n_i = \gamma_i^\dagger \gamma_i = 1$, we recognize that a Majorana mode is "always empty and always filled".
Even though a Majorana state is protected against local perturbations, we can change the state by physical exchange of the Majorana fermions. This is enabled due to their non-Abelian statistics. Non-Abelian statistics is only possible, if we have a degenerate ground state which is separated from all excited states by a gap. By performing adiabatic operations, like a slow exchange of the quasiparticle positions, we can bring the system from one ground state to another. In the case of Majorana fermions in a $p_x \pm ip_y$ superconductor this can be easily understood.

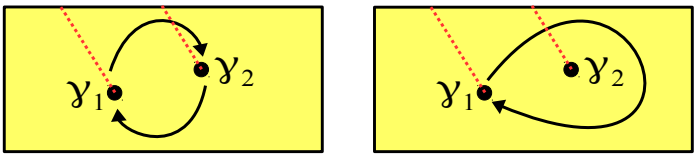

(a) (b)

Figure 9: Two vortices in a 2D $p_x \pm ip_y$ superconductor which host Majorana fermions described by the operators γ_1 and γ_2. The red dashed lines are the branch cuts emanating from the vortex cores. (a) shows a clockwise exchange of the two vortices. In (b) vortex 1 is brought around vortex 2. Both vortices cross the branch cut of the other vortex.

We imagine a 2D topological superconductor with two vortices (1 and 2) where both of them have a Majorana fermion γ_1, γ_2 at their cores (see Fig. 9). Each vortex has a winding of 2π of the superconducting phase ϕ. We choose ϕ to be single-valued everywhere, except for a branch cut that emanates from each vortex. The phase changes by 2π when this branch cut is crossed. If we now exchange the vortices in a clockwise manner (see Fig. 9(a)), one vortex crosses the branch cut of the other and gains a phase shift of 2π, whereas the other does not get any additional phase. The Majorana fermion in the vortex then acquires a phase of π (thus a sign change) when it crosses the branch cut. Consequently, the result of this operation is:

$$\gamma_1 \to -\gamma_2, \qquad \gamma_2 \to \gamma_1. \tag{64}$$

These transformations can be described by so-called braid operators $B_{12} = \frac{1}{\sqrt{2}}(1 + \gamma_1\gamma_2)$:

$$\gamma_1 \to B_{12}\gamma_1 B_{12}^\dagger, \qquad \gamma_2 \to B_{12}\gamma_2 B_{12}^\dagger. \tag{65}$$

If we do the same operation counterclockwise, the other Majorana fermion would get the phase shift and the braid operator used is $\tilde{B}_{12} = \frac{1}{\sqrt{2}}(1 - \gamma_1\gamma_2)$. The braid operations are non-Abelian, because, when they involve some of the same Majorana fermions, they do not commute.
If we exchange the vortices twice, thus bringing them back to their original position, both Majorana fermions gain a negative sign: $\gamma_1 \to -\gamma_1$ and $\gamma_2 \to -\gamma_2$. This is similar to two successive exchanges, thus, the operator is B_{12}^2. This can also be seen in Fig. 9(b), where both vortices cross the branch cut of the other vortex when vortex 1 is brought around vortex 2.
Consequently, the ground state of a system with two Majorana fermions is twofold degenerate. If we have $2N$ vortices, we can define N Dirac fermions consisting of two Majorana fermions and each of these Dirac fermions can be occupied or empty. For $2N$ vortices we have a 2^N-fold degeneracy of the ground state. In a system with only two Majorana fermions the exchange operation cannot change the eigenvalue of the number operator which encodes, whether there are in total an even or odd number of particles in the superconductor. To find nontrivial effects of exchange operations, we need at least four Majorana fermions. Then exchange operations can lead to superposition state of different number states. Only the total parity (all number states added up) must stay the same (meaning must stay odd or even).
By using four Majorana fermions, one can define a Majorana qubit. Such qubits keep the quantum information encoded in delocalized fermionic states and are therefore expected to be robust against most sources of decoherence. This makes the Majorana fermions interesting for quantum computation, even though the braiding operations of the Majorana-based qubits can only explore a tiny fraction of the total Hilbert space, making them insufficient for universal quantum computations. However, by including non-protected operations or by coupling Majorana qubits to other qubit systems, this restriction can be lifted.

In the last sections we provided an introduction to topological insulators, briefly motivated the low-energy effective model Hamiltonian of the Bi_2Se_3 topological insulator and summarized the theory of superconductivity until we finished with systems hosting Majorana fermions. Nevertheless, we aim to calculate the Josephson effect on the surface of a topological insulator. For this reason, we need to discuss what happens, when an electron coming from a normal conductor hits a superconductor. The occurring event is called Andreev reflection.

2.4 Andreev reflection and Josephson current

This section is based on the book by Yuli V. Nazarov and Yaroslav M. Blanter [23]. In the beginning we introduce the scattering matrix s for a nanostructure. By considering an ideal contact between a normal metal and a superconductor, we derive the scattering on superconductors. Later we place a nanostructure between two superconductors and explain the process called Andreev reflection.

2.4.1 Scattering matrix

When nanostructures are fabricated, there are a lot of uncontrollable parameters and it is not possible to construct two identical nanostructures. Nevertheless, the transport properties can be expressed through a smaller set of parameters, such that these fabrication problems do not influence the physics. The condition that must be fulfilled is, that electrons traverse the structure without energy loss and experience only elastic scattering. This is always achieved at sufficiently low temperature and applied voltage.
We can characterize the scattering in a nanostructure by a scattering matrix s which contains the information on the electron wave functions far from the structure. The transport is then described by the transmission eigenvalues of this scattering matrix.

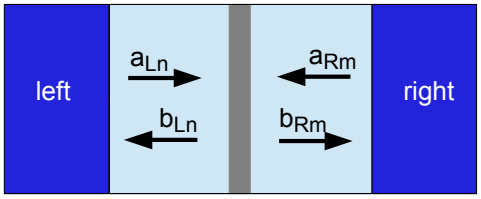

Figure 10: Scattering in a nanostructure. The dark blue regions are the (left and right) reservoirs. The scattering takes place in the scattering region (gray) in the nanostructure (light blue) far from the reservoirs. a_{Ln}, a_{Rm}, b_{Ln}, b_{Rm} represent the amplitude of the plane waves, the arrow shows the direction of transport of the corresponding plane wave.

At first we will derive the scattering matrix. We use the system shown in Fig. 10. It consists of two reservoirs referred to as left and right. In between is the nanostructure in which the scattering happens. The scattering takes place in a finite region (see Fig. 10, gray) and the superconducting reservoirs (see Fig. 10, blue) are far from this region. The wave functions in the scattering region are unknown and may take very complicated form. However, we can assume that the scattering region is connected to the reservoirs by ideal waveguides (see Fig. 10, light blue). The wave functions in ideal waveguides are always combinations of plane waves. As the left and right waveguides are independent of each other, we use different coordinates: $x_L < 0, y_L, z_L$ for the left waveguide and $x_R > 0, y_R, z_R$ for the right one. At fixed energy E we can write the wave function as a linear combination of the plane waves:

$$\begin{aligned}\psi(x_L, y_L, z_L) &= \sum_n \frac{1}{\sqrt{2\pi\hbar v_n}} \Phi_n(y_L, z_L) \left[a_{L_n} e^{ik_x^{(n)} x_L} + b_{L_n} e^{-ik_x^{(n)} x_L}\right], \\ \psi(x_L R, y_R, z_R) &= \sum_m \frac{1}{\sqrt{2\pi\hbar v_m}} \Phi_m(y_R, z_R) \left[a_{R_m} e^{ik_x^{(m)} x_R} + b_{R_m} e^{ik_x^{(m)} x_R}\right].\end{aligned} \tag{66}$$

v_j is the velocity in channel j, $\Phi_n(y_L, z_L)$ and $\Phi_m(y_R, z_R)$ are the transverse wave functions and the energies of the transverse motion are E_n, E_m. For any transport channel n or m, the energy E fixes the value of the wave vector $k_x^{(j)} = \sqrt{2m(E - E_j)/\hbar}$. Here, the transport is due to propagating, not evanescent, waves and $k_x^{(j)}$ has to be real. This means, we only have a finite number of open channels to the left and right at a fixed energy. The coefficients a_{L_n} and a_{R_m} are the amplitudes of the waves coming from the reservoirs and b_{L_n} and b_{R_m} are the amplitudes of the waves transmitted through or reflected back from the scattering region. These coefficients are related to each other:

$$b_{\alpha l} = \sum_{\beta=L,R} \sum_{l'} s_{\alpha l, \beta l'} a_{\beta l'}, \qquad \alpha = L, R, \quad l = n, m. \tag{67}$$

We can write the proportionality coefficients $s_{\alpha l}$ in terms of a matrix:

$$s = \begin{pmatrix} s_{LL} & s_{LR} \\ s_{RL} & s_{RR} \end{pmatrix} = \begin{pmatrix} r & t' \\ t & r' \end{pmatrix}, \tag{68}$$

with the block matrices s_{AB} where $A, B = \{L, R\}$. The reflection matrix r describes the reflection of the waves coming from the left, r' the reflection of the particles coming from the right. t describes the transmission through the scattering region. If we have TR symmetry, the scattering matrix is symmetric: $s = s^\intercal$. Any scattering matrix is unitary: $s^\dagger s = 1$.

2.4.2 Andreev reflection

Andreev reflection is a special form of a scattering process which can happen, when electrons are scattered at the boundary to a superconductor. To explain this process, we first look at the quasiparticle states in a superconductor. The energies of the quasiparticle states are separated from the Fermi energy by the superconducting gap Δ_0. In the gap no states are found. If we bring a metal into contact with the superconductor, an electron in the metal with energy above Δ_0 can enter the superconductor, where it will be converted into a quasiparticle of the same energy. But if an electron has an energy $E < \Delta_0$ this cannot happen, as there are no quasiparticles in the superconductor with such small energy. This means, for voltages and temperatures below Δ_0, no current may flow through the superconductor, at least not in this picture.
As afore mentioned, there exists a different process which enables charge transfer at low energy, the so-called Andreev reflection. An electron coming from the metal hitting a superconductor can be reflected back as a hole, as it is shown in Fig. 11. This process conserves energy but not charge. In the metal we will have a charge deficit of $q_m = -2e$. In the superconductor, on the other hand, there is a Cooper pair with charge $q_s = 2e$. Consequently, charge is transfered from the normal metal to the superconductor. The momentum of the hole $\hbar k_h$ is almost equal to that of the electron: $\hbar k_h = \hbar k_e - 2E/v_F \overset{|E| \ll E_F}{\approx} k_e \approx k_F$, where $\hbar k_F$ is the Fermi momentum. The velocity of the holes is $v_h = \frac{1}{\hbar}\frac{\partial E}{\partial k_h}$ meaning that holes with $k_h > 0$ move away from the superconductor.

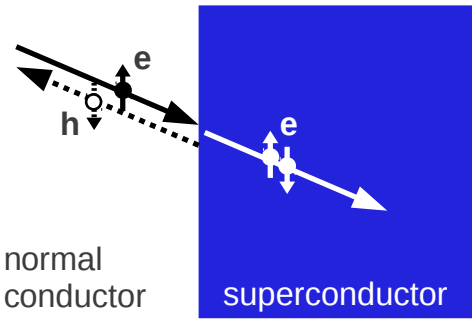

Figure 11: Andreev reflection: an electron is reflected back as a hole inducing a Cooper pair in the superconductor. While energy is conserved, the metal will have a charge deficit of $q_m = -2e$ and the superconductor will gain a charge $q_s = 2e$.

As explained in the preceding chapters, the wave function in a superconductor has to solve the BdG equation

$$\begin{pmatrix} \psi_e(\mathbf{r}) \\ \psi_h(\mathbf{r}) \end{pmatrix} = \begin{pmatrix} H_0(\mathbf{r}) - E_F & \Delta_0 e^{i\phi} \\ \Delta_0 e^{-i\phi} & -\mathcal{T} H_0(\mathbf{r}) \mathcal{T} + E_F \end{pmatrix} \begin{pmatrix} \psi_e(\mathbf{r}) \\ \psi_h(\mathbf{r}) \end{pmatrix}. \tag{69}$$

H_0 is the Hamiltonian for the electrons in the absence of superconductivity. We assume that Δ_0 and ϕ are constant in the superconductor and Δ_0 is the superconducting energy gap far away from the boundaries in the superconductor.
We briefly explain the meaning of this BdG equations. In a normal metal there is no gap ($\Delta_0 = 0$) and the solutions are plane waves $\psi_{e,h}(\mathbf{r}) \propto e^{ik_{e,h}r}$. If we solve the equations for excitations close to the Fermi surface, $|E| \ll E_F$, we find that $k = k_F \pm \frac{E}{\hbar v_F}$ thus the momenta of the electron and hole-like solutions can be either above or below k_F. In the conventional definition of quasiparticles in a normal metal,

electrons have momentum $k > k_F$ and holes $k < k_F$. We can see that the BdG equations allow solutions with positive energies $E_+ = |\hbar v_F(k - k_F)|$ and solutions with negative energies $E_- = -|\hbar v_F(k - k_F)|$ which are not dependent on each other, but they are obtained from each other by a flip of components. As explained in the section above, the underlying symmetry is the particle-hole symmetry. The BdG equations contain a double set of solutions. The solutions with negative energies would represent electrons with $k < k_F$ and holes with $k > k_F$ which contradicts the conventional definition of electrons and holes in a normal metal. Thus, we retain the positive energies only, which represent a complete set of solutions. We look at the solutions of the BdG in a superconductor. By using plane waves for the electron and hole wave functions we get

$$E = \sqrt{\xi^2 + \Delta_0^2}, \qquad \xi = \hbar v_F(k - k_F) \qquad \text{for} \qquad \Delta_0, E \ll E_F. \tag{70}$$

For $E > \Delta_0$ the quasiparticles can freely propagate in the superconductor. For $E < \Delta_0$ no quasiparticles in the superconductor exist.

We consider an ideal (no scattering) contact between a normal metal ($x < 0$) and a superconductor ($x > 0$). Since the transport channels are not mixed we can consider only one channel and we suppress the index. We look at solutions of the form $\psi_{e,h}(x) \propto \tilde{\psi}_{e,h}(x)e^{ik_F x}$ that correspond to an electron propagating to the right and a hole moving in the opposite direction. $\tilde{\psi}$ is the envelope function and varies at a space scale that is much bigger than the electron wavelength. It satisfies the BdG

$$\begin{pmatrix} -i\hbar v_F \frac{\partial}{\partial x} & \Delta(x)e^{i\phi} \\ \Delta(x)e^{-i\phi} & i\hbar v_F \frac{\partial}{\partial x} \end{pmatrix} \begin{pmatrix} \tilde{\psi}_e(x) \\ \tilde{\psi}_h(x) \end{pmatrix} = E \begin{pmatrix} \tilde{\psi}_e(x) \\ \tilde{\psi}_h(x) \end{pmatrix}. \tag{71}$$

In the normal metal the envelope function describes the incoming electron and the outgoing Andreev-reflected hole. With the amplitude r_A of the Andreev reflection we can write

$$\tilde{\psi}(x < 0) = \begin{pmatrix} e^{ixE/\hbar v_F)} \\ r_A e^{-ixE/\hbar v_F} \end{pmatrix}. \tag{72}$$

For $E < \Delta$ we have only evanescent solutions in the superconductors:

$$\tilde{\psi}(x > 0) = C \begin{pmatrix} f_e \\ f_h \end{pmatrix} e^{-x\sqrt{\Delta^2 - E^2}/\hbar v_F}. \tag{73}$$

C is an arbitrary constant and the coefficients $f_{e,h}$ are found from the BdG equation and the normalization condition $|f_e|^2 + |f_h|^2 = 1$. We find

$$f_e = \frac{e^{i\phi}}{\sqrt{2}}, \qquad f_h = \frac{E - i\sqrt{\Delta^2 - E^2}}{\sqrt{2}\Delta}. \tag{74}$$

The superconducting correlation length which describes the scale of penetration into the superconductor is of the order $\hbar v_F/\Delta \gg \lambda_F$ and it diverges at the threshold energy $E = \Delta$. By demanding continuity of the wave functions at $x = 0$, we can calculate r_A and C:

$$C = \frac{1}{f_e}, \qquad r_A = e^{-i\phi}\left(\frac{E}{\Delta} - i\frac{\sqrt{\Delta^2 - E^2}}{\Delta}\right) = e^{i\chi} \qquad \text{with} \qquad \chi = -\arccos\left(\frac{E}{\Delta}\right) - \phi. \tag{75}$$

In other words, the phase of the outgoing hole is shifted by χ with respect to the phase of the incoming electron. Similarly, the phase shift of the amplitude of an incoming hole with respect to an outgoing electron can be calculated: $\tilde{\chi} = -\arccos(E/\Delta) + \phi$.

In a next step we look at a system in which a nanostructure is placed between a normal and a superconducting region. The nanostructure in the normal state is described by the scattering matrix $s(E)$ which depends on energy. At first, we need to find the scattering matrix for electrons and holes. For electrons with energy $E > 0$ it is $s_e = s(E)$. For the holes at the same energy it is related to a scattering matrix with $-E$. We know that an electron and a hole at the same momentum have opposite velocities, meaning that the incoming electrons correspond to outgoing holes and vice versa. Consequently, we have

to invert the usual scattering matrix. As the holes obey a time-reversed Hamiltonian, the matrix has to be transposed. Altogether, we get the scattering matrix s_h for a hole: $s_h = s^*(-E)$.
Like before, we consider only scattering in one channel. As a result, we can write in our scattering matrices: $r_e = r(E)$, $r_h = r^*(-E)$, $t_e = t(E)$ and $t_h = t^*(-E)$. The same is valid for r' and t'. Furthermore, we know that Andreev reflection from the superconductor leads to a phase factor: $e^{i\chi}$ for electrons and $e^{i\tilde{\chi}}$ for holes.

Next, we look at a superconducting junction, where a nanostructure is placed between two superconductors with the same gap Δ_0 but different phases ϕ_L, ϕ_R, as shown in Fig. 12. We assume that the nanostructure is sufficiently short, such that the energy dependence of its scattering matrix is not manifested at the energy scale Δ_0. This implies that the electrons spend a very short time τ_d in the nanostructure and according to Heisenberg's uncertainty principle, this time is too short to allow a response to the superconductivity inside the nanostructure, $\tau_d \Delta_0 \ll \hbar$. The scattering matrix of the nanostructure is thus its scattering matrix in the normal state which we know from the calculations above.
We examine an electron in the nanostructure at sufficiently low energy. It will be Andreev reflected while it tries to enter the superconductor. The same happens to the reflected hole. Consequently, electrons and holes are reflected back and forth which gives rise to discrete energy levels. The bound states for quasiparticles between two superconductors at different phases are called Andreev bound states. At last, we calculate the energy for these bound states.

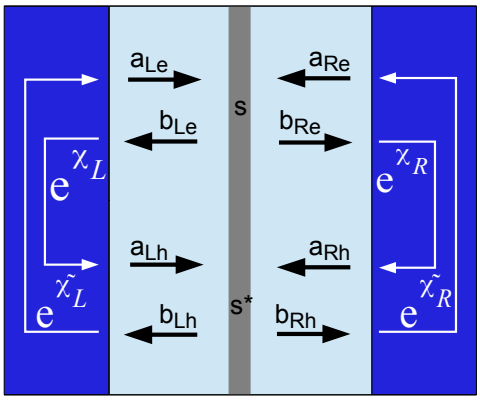

Figure 12: Scattering in the nanostructure and Andreev reflection at the superconductor. The blue regions are the (left and right) superconducting reservoirs. The scattering takes place in the scattering region (gray) in the nanostructure (light blue) far from the reservoirs. At the boundaries to the reservoirs, the plane waves are Andreev reflected, and get an additional phase. a_L, a_R, b_L, b_R represent the amplitude of the plane waves and the arrow shows the direction of transport of the corresponding plane wave. s describes the scattering of the electrons and s^* the scattering of the holes in the nanostructure.

Again we first consider only one channel. Figure 12 illustrates the scattering processes in the nanostructure and at the boundaries to the superconductor. The scattering matrix of the nanostructure relates the amplitudes of the incoming states $(\vec{a}_e, \vec{a}_h)$ and the amplitudes of the outgoing states $(\vec{b}_e, \vec{b}_h)$:

$$\begin{pmatrix} b_e \\ b_h \end{pmatrix} = \begin{pmatrix} s & 0 \\ 0 & s^* \end{pmatrix} \begin{pmatrix} a_e \\ a_h \end{pmatrix}. \tag{76}$$

The two components of the amplitude vectors correspond to the left and right side of the nanostructure:

$$b_e = \begin{pmatrix} b_{L_e} \\ b_{R_e} \end{pmatrix}, \qquad b_h = \begin{pmatrix} b_{L_h} \\ b_{R_h} \end{pmatrix}, \qquad a_e = \begin{pmatrix} a_{L_e} \\ a_{R_e} \end{pmatrix}, \qquad a_h = \begin{pmatrix} a_{L_h} \\ a_{R_h} \end{pmatrix}. \tag{77}$$

The scattering of the holes is given by the complex conjugate s^* of the scattering matrix. The matrix is block-diagonal as the nanostructure does not convert electrons to holes (see Fig. 12). The superconductors, on the contrary, convert electrons to holes and vice versa and lead to an additional phase. This

leads to the relation

$$\begin{pmatrix} a_e \\ a_h \end{pmatrix} = \begin{pmatrix} 0 & s_{eh} \\ s_{he} & 0 \end{pmatrix} \begin{pmatrix} b_e \\ b_h \end{pmatrix}, \tag{78}$$

where

$$\begin{aligned} s_{eh} = \begin{pmatrix} e^{i\tilde{\chi}_L} & 0 \\ 0 & e^{i\tilde{\chi}_R} \end{pmatrix}, \qquad s_{he} = \begin{pmatrix} e^{i\chi_L} & 0 \\ 0 & e^{i\chi_R} \end{pmatrix}, \\ \chi_{L,R} = -\phi_{L,R} - \arccos\left(\frac{E}{\Delta_0}\right), \qquad \tilde{\chi}_{L,R} = \phi_{L,R} - \arccos\left(\frac{E}{\Delta_0}\right). \end{aligned} \tag{79}$$

In Fig. 12 this is shown by the arrows in the superconductor which are labeled with the corresponding phase. By replacing $a_{e,h}$ in Eq. (76) with Eq. (78) we get an equation for $b_{e,h}$. We require nontrivial solutions. This can be expressed in terms of a determinant:

$$\det\left(\begin{pmatrix} s & 0 \\ 0 & s^* \end{pmatrix}\begin{pmatrix} 0 & s_{eh} \\ s_{he} & 0 \end{pmatrix} - \mathbb{I}_{4\times 4}\right) = 0. \tag{80}$$

Solving the equation yields the energy of the bound state:

$$E = \Delta_0\sqrt{1 - \tau\sin^2(\phi/2)}, \tag{81}$$

where τ is the so-called transmission eigenvalue − the eigenvalue of the scattering matrix s − and $\phi = \phi_L - \phi_R$ is the phase difference of the two superconductors. Now we evaluate the solution for many channels. We call k_n the channel n. For any channel we get such a solution $E_n(\tau_n)$.

2.4.3 Josephson current

So far, we computed the excitations in form of bound states. In superconductivity we want to analyze the correspondence between the properties of the excitations and those of the ground state of the superconductor. This is manifested in the symmetry of the BdG equation with respect to positive and negative energies. The solutions at negative energies can be associated with the filled levels contributing to the ground state energy, which is the sum of single particle excitation energies: $E_g = -\sum_n E_n$. All excitation energies contribute to the ground state energy: those corresponding to propagating quasiparticles above the superconducting gap and those of the bound Andreev states. Only the latter contributions depend on the phase difference of the superconductors. This phase dependent part is:

$$E(\phi) = \sum_n E_n(\phi) = \Delta_0 \sum_n \sqrt{1 - \tau_n \sin^2(\phi/2)}, \tag{82}$$

where the sum over n adds all the possible channels in the normal region. This phase dependent energy gives rise to a persistent current in the ground state − a supercurrent. We slowly vary the phase difference. This leads to an energy shift per unit time:

$$\frac{dE}{dt} = \frac{\partial E(\phi)}{\partial \phi}\frac{d\phi}{dt}. \tag{83}$$

The global gauge invariance dictates that the time derivative of the superconducting phase is simply the potential of the corresponding superconductor, $\frac{d\phi}{dt} = \frac{2eV}{\hbar}$. The energy change per unit time is the power dissipated at the junction. On the other hand, this power is the product of current and voltage. We conclude that the current in the junction is given by

$$J(\phi) = -\frac{2e}{\hbar}\sum_n \frac{\partial E_n}{\partial \phi} = \frac{e\Delta_0}{2\hbar}\sum_n \frac{\tau_n \sin(\phi)}{\sqrt{1 - \tau_n \sin^2(\phi/2)}}. \tag{84}$$

This Josephson current is an odd periodic function of the phase difference and vanishes at $\phi = 0$. For a tunnel junction where $\tau_n \ll 1$, the supercurrent is $J(\phi) = J_c \sin(\phi)$, where $J_c = \frac{e\Delta_0}{2\hbar}\sum_n \tau_n$ is the maximal possible supercurrent achieved at $\phi = \pi/2$.

We calculated the Josephson current due to Andreev reflection. We have seen that it can be described in

terms of the transmission eigenvalues of the scattering matrix describing the normal region (the nanostructure). Now we analyze the problem from a slightly different point of view: instead of the scattering approach, we use the wave functions which solve the BdG equations in the different regions and apply conditions for the interfaces. We calculate the energy as a function of the phase difference ϕ of the two superconductors and by taking the derivative of the energy with respect to ϕ we finally get the Josephson current.
In fact, the so-called Josephson effect is an effect which Brian D. Josephson predicted in 1962 [24]. He stated that at zero voltage a supercurrent $J_s = J_c \sin(\phi)$ should flow between two superconducting electrodes which are separated by a thin insulating barrier. ϕ is the phase difference of the wave functions of the two superconducting electrodes. J_c is called the critical current and is the maximum supercurrent that the junction can support. The more general expression Josephson used to calculate the current requires the ground state energy E_g of the junction

$$J(\phi) = -\frac{2e}{\hbar}\frac{\partial E_g}{\partial \phi}, \tag{85}$$

and is valid at temperature $T = 0$.
The expression of the Josephson current may take a form similar to Eq. (84) with a transmission eigenvalue τ (for instance if the junction is a normal metal). But as soon as we have a ferromagnetic junction, the form becomes different, because ferromagnetism breaks the TR symmetry.

By understanding the Josephson effect, we eventually have the basic knowledge to begin with the calculations.

3 Derivation of the surface Hamiltonians of the topological insulator Bi_2Se_3

3.1 Calculation of the surface Hamiltonian in the (y−z) plane

The Hamiltonian describing the bulk of the Bi_2Se_3 topological insulator is given by (see chapter 2)

$$H(\mathbf{k}) = \varepsilon_0(\mathbf{k})\mathbb{I}_{4\times 4} + \begin{pmatrix} M(\mathbf{k}) & A_1 k_z & 0 & A_2 k_- \\ A_1 k_z & -M(\mathbf{k}) & A_2 k_- & 0 \\ 0 & A_2 k_+ & M(\mathbf{k}) & -A_1 k_z \\ A_2 k_+ & 0 & -A_1 k_z & -M(\mathbf{k}) \end{pmatrix}. \tag{86}$$

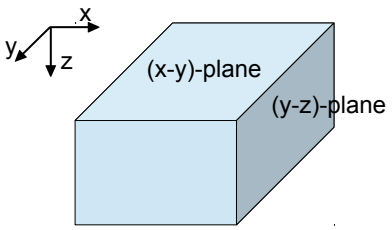

Figure 13: Bulk with the coordinate system.

To get the Hamiltonian for the surfaces, we use the method of Zhou et al. [25] for quantum spin Hall systems and follow the procedure of Ref. [26]. To calculate our surface states in the $(y-z)$ plane (see Fig. 13 for the coordinate orientation) we start with the bulk Hamiltonian (Eq. (86)) and we suggest a four-component trial solution of the form:

$$\Psi = \psi_\lambda e^{\lambda x}. \tag{87}$$

By putting this in the Hamiltonian of the bulk (Eq. (86)) and using $(k_x, k_y, k_z) = (-i\partial_x, k_y, k_z)$ we can write the Hamiltonian as follows:

$$H(\mathbf{k}) = \begin{pmatrix} L_1 - D_-\lambda^2 & A_1 k_z & 0 & -iA_2(k_y+\lambda) \\ A_1 k_z & L_2 - D_+\lambda^2 & -iA_2(k_y+\lambda) & 0 \\ 0 & -iA_2(\lambda - k_y) & L_1 - D_-\lambda^2 & -A_1 k_z \\ -iA_2(\lambda - k_y) & 0 & -A_1 k_z & L_2 - D_+\lambda^2 \end{pmatrix}, \tag{88}$$

where $L_1 = C + M + S_- k_z^2 + D_- k_y^2$, $L_2 = C - M + S_+ k_z^2 + D_+ k_y^2$, $S_\pm = D_1 \pm B_1$ and $D_\pm = D_2 \pm B_2$. We solve the secular equation $\det|H(\mathbf{k}) - \varepsilon \cdot \mathbb{I}_{4\times 4}| = 0$ for λ:

$$\lambda_{\alpha\beta}(\varepsilon) = \beta\sqrt{-\frac{F}{2D_-D_+} + \alpha\frac{\sqrt{R}}{2D_-D_+}}, \tag{89}$$

with $F = A_2^2 + D_+(\varepsilon - L_1) + D_-(\varepsilon - L_2)$, $R = F^2 - 4D_+D_-((\varepsilon - L_1)(\varepsilon - L_2) - A_1^2 k_z^2 - A_2^2 k_y^2)$ and $\alpha = \pm$, $\beta = \pm$. Each of these solutions is doubly degenerate, implying that for each λ there are two linearly independent ψ_λ. Next, we calculate

$$\psi_\lambda = \begin{pmatrix} \phi_1 \\ \phi_2 \\ \phi_3 \\ \phi_4 \end{pmatrix} \tag{90}$$

by solving the equation

$$H(\mathbf{k})\psi_\lambda = \varepsilon\psi_\lambda. \tag{91}$$

We obtain two linearly independent solutions for each λ:

$$\psi_\lambda^{(1)} = \begin{pmatrix} \varepsilon - L_2 + D_+\lambda^2 \\ A_1 k_z \\ 0 \\ -iA_2(\lambda - k_y) \end{pmatrix} \text{ and } \psi_\lambda^{(2)} = \begin{pmatrix} -iA_2(\lambda + k_y) \\ 0 \\ -A_1 k_z \\ \varepsilon - L_1 + D_-\lambda^2 \end{pmatrix}. \tag{92}$$

With these we can devise a general solution

$$\Psi(\varepsilon, k_y, k_z, x) = \sum_{\alpha=\pm} \sum_{\beta=\pm} \sum_{\gamma=1,2} C_{\alpha\beta}^\gamma \psi_{\lambda_{\alpha\beta}}^\gamma e^{\lambda_{\alpha\beta} x}. \tag{93}$$

Afterwards we use the boundary conditions $\Psi(x=0) = \Psi(x=-\infty) = 0$. The latter implies that all $C_{\alpha-}^\gamma = 0$. Thus, there are only solutions for $\beta = +$. We apply $\Psi(x=0) = 0$ and demand a nontrivial solution for $C_{\alpha+}^\gamma$ (which means the determinant of the coefficient matrix has to be 0). This leads to the important equation:

$$(\lambda_+ + \lambda_-)^2 = -\frac{A_2^2}{D_+ D_-}, \tag{94}$$

where we abbreviated $\lambda_{\pm+}$ to $\lambda_\pm$. We compare this expression with $\lambda_{\alpha+}(\varepsilon)$ from Eq. (89)

$$(\lambda_+ + \lambda_-)^2 = \lambda_+^2 + \lambda_-^2 + 2\lambda_+\lambda_- = -\frac{F}{D_+ D_-} + 2\sqrt{\frac{F^2}{(2D_+D_-)^2} - \frac{R}{(2D_+D_-)^2}} \tag{95}$$

and we conclude

$$F^2 - R = (-A_2^2 + F)^2. \tag{96}$$

This can be solved for the energy ε:

$$\varepsilon = C + \frac{D_2}{B_2} M \pm \sqrt{1 - \frac{D_2^2}{B_2^2}} \sqrt{A_2^2 k_y^2 + A_1^2 k_z^2} + (D_1 - \frac{D_2}{B_2} B_1) k_z^2. \tag{97}$$

Furthermore, we find from $\Psi(x=0) = 0$ that

$$C_-^1 = -C_+^1 \text{ and } C_-^2 = -C_+^2, \tag{98}$$

and two similar expressions for C_+^2:

$$C_+^2 = C_+^1 \frac{D_+(\lambda_+ + \lambda_-)}{iA_2} \text{ and } C_+^2 = C_+^1 \frac{iA_2}{D_-(\lambda_+ + \lambda_-)}. \tag{99}$$

We can simplify the total surface wave functions in Eq. (93) to:

$$\Psi(k_y, k_z, x) = C_+^1 \begin{pmatrix} \mp\sqrt{-\frac{D_+}{D_-}} \sqrt{A_2^2 k_y^2 + A_1^2 k_z^2} - D_+(\lambda_+ + \lambda_-) k_y \\ A_1 k_z \\ -A_1 k_z \frac{iA_2}{D_-(\lambda_+ + \lambda_-)} \\ \pm \frac{iA_2}{D_-(\lambda_+ + \lambda_-)} \sqrt{-\frac{D_-}{D_+}} \sqrt{A_2^2 k_y^2 + A_1^2 k_z^2} + iA_2 k_y \end{pmatrix} (e^{\lambda_+ x} - e^{\lambda_- x}). \tag{100}$$

Now we expand the Hamiltonian $H(\mathbf{k})$ (Eq. (88)) for small $|\mathbf{k}|$. This is possible due to the low-energy long-wavelength nature of the Dirac cone of the surface states at the Γ point. This expansion is valid when the energy is limited within the band gap between the conduction and valence bands [26]. For this reason we use:

$$H(\mathbf{k}) = H_0(\mathbf{k} = 0) + \Delta H, \tag{101}$$

where

$$H_0(\mathbf{k}=0) = \begin{pmatrix} C + M - D_-\lambda^2 & 0 & 0 & -iA_2\lambda \\ 0 & C - M - D_+\lambda^2 & -iA_2\lambda & 0 \\ 0 & -iA_2\lambda & C + M - D_-\lambda^2 & 0 \\ -iA_2\lambda & 0 & 0 & C - M - D_+\lambda^2 \end{pmatrix} \tag{102}$$

and

$$\Delta H = \begin{pmatrix} S_- k_z^2 + D_- k_y^2 & A_1 k_z & 0 & -iA_2 k_y \\ A_1 k_z & S_+ k_z^2 + D_+ k_y^2 & -iA_2 k_y & 0 \\ 0 & iA_2 k_y & S_- k_z^2 + D_- k_y^2 & -A_1 k_z \\ iA_2 k_y & 0 & -A_1 k_z & S_+ k_z^2 + D_+ k_y^2 \end{pmatrix}. \tag{103}$$

By using

$$\Psi = \psi_\lambda e^{\lambda x} = \begin{pmatrix} \phi_1 \\ \phi_2 \\ \phi_3 \\ \phi_4 \end{pmatrix} e^{\lambda x}, \tag{104}$$

we recognize that we can write the eigenvalue equation $H(\mathbf{k}=0)\psi_\lambda = \varepsilon\psi_\lambda$ in terms of two decoupled equations:

$$h \begin{pmatrix} \phi_1 \\ \phi_4 \end{pmatrix} = \varepsilon \begin{pmatrix} \phi_1 \\ \phi_4 \end{pmatrix} \text{ and } h \begin{pmatrix} \phi_3 \\ \phi_2 \end{pmatrix} = \varepsilon \begin{pmatrix} \phi_3 \\ \phi_2 \end{pmatrix}, \tag{105}$$

$$\text{where} \qquad h = \begin{pmatrix} C + M - D_- \lambda^2 & -iA_2\lambda \\ -iA_2\lambda & C - M - D_+\lambda^2 \end{pmatrix}. \tag{106}$$

Solving the secular equation $\det|h - \varepsilon \cdot \mathbb{I}_{4\times4}| = 0$ leads to the same $\lambda_{\alpha\beta}$ from Eq. (89) but with $\mathbf{k} = 0$. We calculate the solution of the eigenvalue equation:

$$\begin{pmatrix} \phi_1 \\ \phi_4 \end{pmatrix}_{tot} = \sum_{\alpha=\pm} \sum_{\beta=\pm} C_{\alpha\beta} \begin{pmatrix} C - M - D_+\lambda_{\alpha\beta} - \varepsilon \\ iA_2\lambda_{\alpha\beta} \end{pmatrix} e^{\lambda_{\alpha\beta} x}. \tag{107}$$

Due to the boundary condition $\begin{pmatrix} \phi_1 \\ \phi_4 \end{pmatrix}_{tot}(x = -\infty) = 0$ we know that all $C_{\alpha-} = 0$. We calculate $\begin{pmatrix} \phi_1 \\ \phi_4 \end{pmatrix}_{tot}(x = 0) = 0$. This results in the equations:

$$\begin{aligned} &C_{-+} = -\frac{\lambda_+}{\lambda_-} C_{++}, \\ &(C - M - D_+\lambda_+^2 - \varepsilon)\lambda_- = (C - M - D_+\lambda_-^2 - \varepsilon)\lambda_+, \end{aligned} \tag{108}$$

and finally

$$\varepsilon = C - M + D_+\lambda_+\lambda_-. \tag{109}$$

Now our wave function can be further simplified to

$$\begin{pmatrix} \phi_1 \\ \phi_4 \end{pmatrix}_{tot} = C' \begin{pmatrix} -D_+(\lambda_+ + \lambda_-) \\ iA_2 \end{pmatrix} e^{\lambda_+ x} - e^{\lambda_- x}, \tag{110}$$

where C' is the normalization constant. We use Eq. (94) and normalize the spinors. This ends in

$$\begin{pmatrix} \phi_1 \\ \phi_4 \end{pmatrix} = \sqrt{\frac{-D_-}{2A_2^2 B_2}} \begin{pmatrix} -D_+\sqrt{-\frac{A_2^2}{D_+D_-}} \\ iA_2 \end{pmatrix}. \tag{111}$$

The complete set of spinor solutions for $H(\mathbf{k}=0)\Phi = \varepsilon\Phi$ is given by the two basis spinors:

$$\Phi_1 = \begin{pmatrix} \phi_1 \\ 0 \\ 0 \\ \phi_4 \end{pmatrix} = \sqrt{\frac{-D_-}{2A_2^2 B_2}} \begin{pmatrix} -D_+\sqrt{-\frac{A_2^2}{D_+D_-}} \\ 0 \\ 0 \\ iA_2 \end{pmatrix} \text{ and } \Phi_2 = \begin{pmatrix} 0 \\ \phi_4 \\ \phi_1 \\ 0 \end{pmatrix} = \sqrt{\frac{-D_-}{2A_2^2 B_2}} \begin{pmatrix} 0 \\ iA_2 \\ -D_+\sqrt{-\frac{A_2^2}{D_+D_-}} \\ 0 \end{pmatrix}. \tag{112}$$

We can use these two basis states to expand the Hamiltonian (88). This leads to a new effective surface Hamiltonian:

$$H_{\text{eff}} = \int_{-\infty}^{\infty} dx [\Phi_1, \Phi_2]^\dagger H(\mathbf{k})_{\lambda\to\partial_x} [\Phi_1, \Phi_2], \tag{113}$$

where we replaced λ by ∂_x, and finally

$$H_{\text{eff}} = C + \frac{D_2}{B_2}M + (D_1 - \frac{D_2}{B_2}B_1)k_z^2 - A_2\sqrt{1-\frac{D_2^2}{B_2^2}}\sigma_z k_y + A_1\sqrt{1-\frac{D_2^2}{B_2^2}}\sigma_y k_z, \tag{114}$$

which is the same as the surface Hamiltonian H^{yz} (Eq. (9)) when keeping only the terms to linear order in $|\mathbf{k}|$.

3.2 Calculation of the surface Hamiltonian in the ((x $\cos(\vartheta)$−y $\sin(\vartheta)$)-z) plane

The idea here is to calculate the Hamiltonian of a surface when the bulk is cut at an angle ϑ. The setup is shown in Fig. 14.

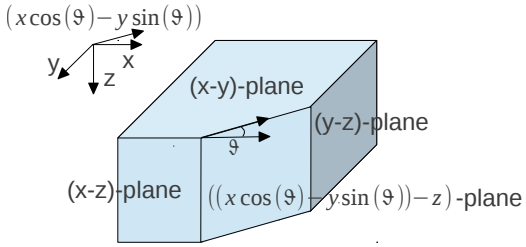

Figure 14: Bulk cut at an angle ϑ and the used coordinate system.

The Hamiltonian describing the bulk of the Bi_2Se_3 topological insulator is given by (see chapter 2)

$$H(\mathbf{k}) = \varepsilon_0(\mathbf{k})\mathbb{I}_{4\times4} + \begin{pmatrix} M(\mathbf{k}) & A_1k_z & 0 & A_2k_- \\ A_1k_z & -M(\mathbf{k}) & A_2k_- & 0 \\ 0 & A_2k_+ & M(\mathbf{k}) & -A_1k_z \\ A_2k_+ & 0 & -A_1k_z & -M(\mathbf{k}) \end{pmatrix}. \tag{115}$$

To get the Hamiltonian for the surfaces, we again use the method of Zhou et al. [25] for quantum spin Hall systems and follow the procedure of Ref. [26]. To calculate our surface states in the $((x\cos(\vartheta) - y\sin(\vartheta)) - z)$ plane we start with the bulk Hamiltonian (Eq. (115))and we suggest a four-component trial solution of the form:

$$\Psi = \psi_\lambda e^{\lambda(x\sin(\vartheta)+y\cos(\vartheta))+ik_p(x\cos(\vartheta)-y\sin(\vartheta))+ik_z z}. \tag{116}$$

k_p is the momentum in the plane at angle ϑ. By putting this in the Hamiltonian of the bulk (equation (115)) and using $(k_x, k_y, k_z) = (-i\partial_x, -i\partial_y, -i\partial_z)$ we get:

$$H(\mathbf{k}) = \varepsilon_0\mathbb{I}_{4\times4} + \begin{pmatrix} M(\mathbf{k}) & A_1k_z & 0 & A_2(k_p-\lambda)(\cos(\vartheta)+i\sin(\vartheta)) \\ -M(\mathbf{k}) & A_2(k_p-\lambda)(\cos(\vartheta)+i\sin(\vartheta)) & 0 & \\ 0 & A_2(\lambda+k_p)(\cos(\vartheta)-i\sin(\vartheta)) & M(\mathbf{k}) & -A_1k_z \\ A_2(\lambda+k_p)(\cos(\vartheta)-i\sin(\vartheta)) & 0 & -A_1k_z & -M(\mathbf{k}) \end{pmatrix}, \tag{117}$$

where $\varepsilon_0 = C + D_1k_z^2 - D_2(\lambda^2 - k_p^2)$ and $M(\mathbf{k}) = M - B_1k_z^2 + B_2(\lambda^2 - k_p^2)$. In the new coordinates we have $\mathbf{k} = (k_p, k_v, k_z)^\intercal$ where k_p is in plane and k_v is perpendicular to the plane. We solve the secular equation $\det|H(\mathbf{k}) - \varepsilon\cdot\mathbb{I}_{4\times4}| = 0$ for λ:

$$\lambda_{\alpha\beta}(\varepsilon) = \beta\sqrt{-\frac{F}{2D_-D_+} + \alpha\frac{\sqrt{R}}{2D_-D_+}}, \tag{118}$$

with

$$F = A_2^2 - 2D_-D_+k_p^2 - D_-(C - M + k_z^2S_+ - \varepsilon) - D_+(C + M + k_z^2S_- - \varepsilon), \tag{119}$$

$$R = F^2 - 4D_+D_-((C + M + k_z^2S_- - \varepsilon + D_-k_p^2)(C + M + k_z^2S_+ - \varepsilon + D_+k_p^2) - A_1^2k_z^2 - A_2^2k_p^2)), \tag{120}$$

and $\alpha = \pm$, $\beta = \pm$, $S_\pm = D_1 \pm B_1$ and $D_\pm = D_2 \pm B_2$. Each of these solution is doubly degenerate, meaning for each λ there are two linearly independent ψ_λ. Next, we calculate

$$\psi_\lambda = \begin{pmatrix} \phi_1 \\ \phi_2 \\ \phi_3 \\ \phi_4 \end{pmatrix} \tag{121}$$

by solving the equation

$$H(\mathbf{k})\psi_\lambda = \varepsilon\psi_\lambda. \tag{122}$$

We obtain two linearly independent solutions for each λ:

$$\psi_\lambda^{(1)} = \begin{pmatrix} A_2(k_p - \lambda)(\cos(\vartheta) + i\sin(\vartheta)) \\ 0 \\ -A_1 k_z \\ -((C+M) + S_- k_z^2 + D_-(k_p^2 - \lambda^2) - \varepsilon) \end{pmatrix}, \; \psi_\lambda^{(2)} = \begin{pmatrix} -((C-M) + S_+ k_z^2 + D_+(k_p^2 - \lambda^2) - \varepsilon) \\ A_1 k_z \\ 0 \\ A_2(k_p + \lambda)(\cos(\vartheta) - i\sin(\vartheta)) \end{pmatrix}. \tag{123}$$

With these we can construct a general solution

$$\Psi(\varepsilon, k_p, k_z, x, y) = \sum_{\alpha=\pm}\sum_{\beta=\pm}\sum_{\gamma=1,2} C_{\alpha\beta}^\gamma \psi_{\lambda_{\alpha\beta}}^\gamma e^{\lambda_{\alpha\beta}(x\sin(\vartheta)+y\cos(\vartheta))}. \tag{124}$$

Afterwards we use the boundary conditions $\Psi((x\sin(\vartheta) + y\cos(\vartheta)) = 0) = \Psi((x\sin(\vartheta) + y\cos(\vartheta)) = -\infty) = 0$. The latter implies that all $C_{\alpha-}^\gamma = 0$, implying that there are only solutions for $\beta = +$. We put the wave function in $\Psi((x\sin(\vartheta) + y\cos(\vartheta)) = 0) = 0$ and demand a nontrivial solution for $C_{\alpha+}^\gamma$ (which means the determinant of the coefficient matrix has to be 0). This leads to the important equation:

$$(\lambda_+ + \lambda_-)^2 = -\frac{A_2^2}{D_+ D_-}, \tag{125}$$

where we abbreviated $\lambda_{\pm+}$ to $\lambda_\pm$. We expand the Hamiltonian $H(\mathbf{k})$ (Eq. (88)) for small $|\mathbf{k}|$. This is possible due to the low-energy long-wavelength nature of the Dirac cone of the surface states at the Dirac point Γ. This expansion is valid when the energy is limited within the band gap between the conduction and valence bands [26]. For this reason we use:

$$H(\mathbf{k}) = H_0(\mathbf{k} = 0) + \Delta H, \tag{126}$$

where

$$H_0(\mathbf{k}=0) = \begin{pmatrix} C + M - D_-\lambda^2 & 0 & 0 & -A_2\lambda(\cos(\vartheta) + i\sin(\vartheta)) \\ 0 & C - M - D_+\lambda^2 & -A_2\lambda(\cos(\vartheta) + i\sin(\vartheta)) & 0 \\ 0 & A_2\lambda(\cos(\vartheta) - i\sin(\vartheta)) & C + M - D_-\lambda^2 & 0 \\ A_2\lambda(\cos(\vartheta) - i\sin(\vartheta)) & 0 & 0 & C - M - D_+\lambda^2 \end{pmatrix} \tag{127}$$

and

$$\Delta H = \begin{pmatrix} S_- k_z^2 + D_- k_p^2 & A_1 k_z & 0 & A_2 k_p(\cos(\vartheta) + i\sin(\vartheta)) \\ A_1 k_z & S_+ k_z^2 + D_+ k_p^2 & A_2 k_p(\cos(\vartheta) + i\sin(\vartheta)) & 0 \\ 0 & A_2 k_p(\cos(\vartheta) - i\sin(\vartheta)) & S_- k_z^2 + D_- k_p^2 & -A_1 k_z \\ A_2 k_p(\cos(\vartheta) - i\sin(\vartheta)) & 0 & -A_1 k_z & S_+ k_z^2 + D_+ k_p^2 \end{pmatrix}. \tag{128}$$

By using

$$\Psi = \psi_\lambda e^{\lambda(x\sin(\vartheta)+y\cos(\vartheta))} = \begin{pmatrix} \phi_1 \\ \phi_2 \\ \phi_3 \\ \phi_4 \end{pmatrix} e^{\lambda(x\sin(\vartheta)+y\cos(\vartheta))} \tag{129}$$

we recognize that we can write the eigenvalue equation $H(\mathbf{k}=0)\psi_\lambda = \varepsilon\psi_\lambda$ in terms of two decoupled equations:

$$h_1 \begin{pmatrix}\phi_1\\ \phi_4\end{pmatrix} = \varepsilon \begin{pmatrix}\phi_1\\ \phi_4\end{pmatrix} \text{ and } h_2 \begin{pmatrix}\phi_2\\ \phi_3\end{pmatrix} = \varepsilon \begin{pmatrix}\phi_2\\ \phi_3\end{pmatrix}, \tag{130}$$

where

$$h_1 = \begin{pmatrix} C+M-D_-\lambda^2 & A_2\lambda(\cos(\vartheta)+i\sin(\vartheta)) \\ A_2\lambda(\cos(\vartheta)-i\sin(\vartheta)) & C-M-D_+\lambda^2 \end{pmatrix} \tag{131}$$

and

$$h_2 = \begin{pmatrix} C-M-D_+\lambda^2 & -A_2\lambda(\cos(\vartheta)+i\sin(\vartheta)) \\ A_2\lambda(\cos(\vartheta)-i\sin(\vartheta)) & C+M-D_-\lambda^2 \end{pmatrix}. \tag{132}$$

Solving the secular equations $\det|h_{1,2}-\varepsilon\cdot\mathbb{I}_{4\times4}|=0$ leads to the same $\lambda_{\alpha\beta}$ from Eq. (118) but with $\mathbf{k}=0$. We calculate the solution of the eigenvalue equations:

$$\begin{pmatrix}\phi_1\\ \phi_4\end{pmatrix}_{tot} = \sum_{\alpha=\pm}\sum_{\beta=\pm} C_{\alpha\beta} \begin{pmatrix} A_2\lambda_{\alpha\beta}(\cos(\vartheta)+i\sin(\vartheta)) \\ C+M-D_-\lambda_{\alpha\beta}-\varepsilon \end{pmatrix} e^{\lambda_{\alpha\beta}(x\sin(\vartheta)+y\cos(\vartheta))}. \tag{133}$$

and

$$\begin{pmatrix}\phi_2\\ \phi_3\end{pmatrix}_{tot} = \sum_{\alpha=\pm}\sum_{\beta=\pm} C'_{\alpha\beta} \begin{pmatrix} C+M-D_-\lambda_{\alpha\beta}-\varepsilon \\ -A_2\lambda_{\alpha\beta}(\cos(\vartheta)-i\sin(\vartheta)) \end{pmatrix} e^{\lambda_{\alpha\beta}(x\sin(\vartheta)+y\cos(\vartheta))}. \tag{134}$$

Due to the boundary condition $\begin{pmatrix}\phi_1\\ \phi_4\end{pmatrix}_{tot}((x\sin(\vartheta)+y\cos(\vartheta))=-\infty)=0$ we know that all $C_{\alpha-}=0$ and similarly $C'_{\alpha-}=0$. We calculate $\begin{pmatrix}\phi_1\\ \phi_4\end{pmatrix}_{tot}((x\sin(\vartheta)+y\cos(\vartheta))=0)=0$. Because we want nontrivial solutions for the coefficients, we can write the equation in Matrix form and ask for a nonzero determinant. This leads to

$$\varepsilon = C+M+D_-\lambda_+\lambda_-. \tag{135}$$

Now our wave function can be further simplified by using Eq. (125)

$$\begin{pmatrix}\phi_1\\ \phi_4\end{pmatrix} = N\begin{pmatrix}\cos(\vartheta)+i\sin(\vartheta)\\ -\sqrt{-\frac{D_-}{D_+}}\end{pmatrix}, \qquad \begin{pmatrix}\phi_2\\ \phi_3\end{pmatrix} = N\begin{pmatrix}\sqrt{-\frac{D_-}{D_+}}\\ \cos(\vartheta)-i\sin(\vartheta)\end{pmatrix}, \tag{136}$$

where $N=\sqrt{\frac{D_+}{2B_2}}$ is the normalization constant.
The complete set of spinor solutions for $H(\mathbf{k}=0)\Phi=\varepsilon\Phi$ is given by the two basis spinors:

$$\Phi_1 = \begin{pmatrix}\phi_1\\0\\0\\\phi_4\end{pmatrix} = \sqrt{\frac{D_+}{2B_2}}\begin{pmatrix}\cos(\vartheta)+i\sin(\vartheta)\\0\\0\\-\sqrt{-\frac{D_-}{D_+}}\end{pmatrix} \text{ and } \Phi_2 = \begin{pmatrix}0\\\phi_2\\\phi_3\\0\end{pmatrix} = \sqrt{\frac{D_+}{2B_2}}\begin{pmatrix}0\\\sqrt{-\frac{D_-}{D_+}}\\\cos(\vartheta)-i\sin(\vartheta)\\0\end{pmatrix}. \tag{137}$$

We can use these two basis states to expand the Hamiltonian (88). This leads to a new effective surface Hamiltonian:

$$H_{\text{eff}} = \int_{-\infty}^{\infty} d(x\sin(\vartheta)+y\cos(\vartheta))[\Phi_1,\Phi_2]^\dagger H(\mathbf{k})_{\lambda\to\partial_x}[\Phi_1,\Phi_2], \tag{138}$$

and finally

$$\begin{aligned} H_{\text{eff}} &= C+\frac{D_2}{B_2}M+(D_1-\frac{B_1}{B_2}D_2)k_z^2 - A_2\sqrt{1-\frac{D_2^2}{B_2^2}}\sigma_z k_p + A_1\sqrt{1-\frac{D_2^2}{B_2^2}}k_z(\sigma_x\cos(\vartheta)+\sigma_y\sin(\vartheta)) \\ &\approx C+\frac{D_2}{B_2}M - A_2\sqrt{1-\frac{D_2^2}{B_2^2}}\sigma_z k_p + A_1\sqrt{1-\frac{D_2^2}{B_2^2}}k_z(\sigma_x\cos(\vartheta)+\sigma_y\sin(\vartheta)). \end{aligned} \tag{139}$$

For $\vartheta = \pi/2$ we get $k_p = k_y$ and we can restore the Hamiltonian for H^{yz} (Eq. (9)). If $\vartheta = 0$ we have $k_p = k_x$ and we receive the Hamiltonian H^{xz} in the $(x - z)$ plane which is

$$H^{xz} = C + \frac{D_2}{B_2} M + A_2 \sqrt{1 - \frac{D_2^2}{B_2^2}} (k_z \frac{A_1}{A_2} \sigma_x - \sigma_z k_x). \tag{140}$$

This result for the $(x - z)$ plane can also be calculated similarly as we presented it for $(y - z)$ plane.

4 Josephson effect in topological insulator planar, step and edge junctions

We derived the Josephson current which is transported through a junction due to Andreev bound states. Such calculations can be done easily in one dimensional and two dimensional systems, as for example nanowires and two dimensional conducting surfaces of topological insulators. In the theory part we also showed that the surfaces can be described by 2×2 Hamiltonians which are TR invariant. All these properties are used to calculate the Josephson effect on surfaces of topological insulators. We do this for three different geometries: planar, step and edge junctions. We begin by briefly summarizing the relevant Hamiltonians of the system.
The bulk material we consider is Bi_2Se_3. As demonstrated, the low-energy effective Hamiltonian for Bi_2Se_3 in the basis of four hybridized states of Se and Bi p_z-orbitals denoted as ($|P1_z^+ \uparrow\rangle$, $|P2_z^- \uparrow\rangle$, $|P1_z^+ \downarrow\rangle$, $|P2_z^- \downarrow\rangle$) can be written as

$$H(\mathbf{k}) = \varepsilon_0(\mathbf{k})\mathbb{I}_{4\times 4} + \begin{pmatrix} M(\mathbf{k}) & A_1 k_z & 0 & A_2 k_- \\ A_1 k_z & -M(\mathbf{k}) & A_2 k_- & 0 \\ 0 & A_2 k_+ & M(\mathbf{k}) & -A_1 k_z \\ A_2 k_+ & 0 & -A_1 k_z & -M(\mathbf{k}) \end{pmatrix}, \tag{141}$$

where $k_\pm = k_x \pm i k_y$, $\varepsilon_0(\mathbf{k}) = C + D_1 k_z^2 + D_2 k_+ k_-$, $M(\mathbf{k}) = M - B_1 k_z^2 - B_2 k_+ k_-$, and $k_+ k_- = k_x^2 + k_y^2$. Here $\uparrow$ ($\downarrow$) stands for up (down) spin and $+$ ($-$) stands for even (odd) parity.

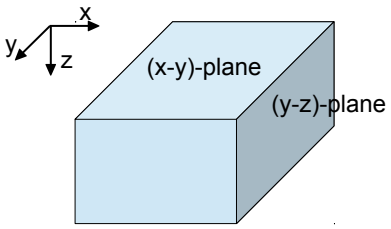

Figure 15: Bulk material and coordinate system.

We use the coordinate orientation shown in Fig. 15. To induce a Josephson effect, we need superconducting regions. This is achieved by bringing the surface in contact with an s-wave superconductor. The proximity effect then induces effective p-wave superconductivity in the surface states. Since the topological insulator Bi_2Se_3 has an insulating bulk and only the surface states are conducting, it is sufficient to know the surface Hamiltonians and we don't have to worry about the bulk anymore.
The effective Hamiltonian describing carriers in the $(x-y)$ plane of the topological insulator is given by

$$H^{xy} = \varepsilon_0^{xy} + \hbar v_F^{xy}(\sigma_x k_y - \sigma_y k_x), \tag{142}$$

where $\varepsilon_0^{xy} = C + (D_1/B_1)M$ is the energy at the Dirac point, $\hbar v_F^{xy} = A_2\sqrt{1-(D_1/B_1)^2}$ represents the Fermi velocity in the $(x-y)$ plane, and $\sigma_i, (i = x, y, z)$ denote the Pauli matrices. In the $(y-z)$ plane it is

$$H^{yz} = \varepsilon_0^{yz} + \hbar v_F^{yz}(\sigma_y \frac{A_1}{A_2} k_z - \sigma_z k_y), \tag{143}$$

with the Dirac point energy $\varepsilon_0^{yz} = C + (D_2/B_2)M$ and the Fermi velocity $\hbar v_F^{yz} = A_2\sqrt{1-(D_2/B_2)^2}$.

These two surface Hamiltonians are TR invariant. The TR operator is $\mathcal{T} = \mathbb{I}_{2\times 2} \otimes i\sigma_y K$. To describe the electrons and holes in one Hamiltonian, we write the surface states in the Nambu basis and subtract the chemical potential μ which is equal to the Fermi energy E_F at $T = 0$ ($\mu \overset{T=0}{=} E_F$):

$$\mathbf{H^n_{xy}} = \begin{pmatrix} H^{xy} - \mu & 0 \\ 0 & -H^{xy} + \mu \end{pmatrix}, \qquad \mathbf{H^n_{yz}} = \begin{pmatrix} H^{yz} - \mu & 0 \\ 0 & -H^{yz} + \mu \end{pmatrix}. \tag{144}$$

The eigenvalue problem now takes the form:

$$\mathbf{H}^{\mathbf{n}}_{\mathbf{xy}}\Psi = \varepsilon\Psi, \qquad \mathbf{H}^{\mathbf{n}}_{\mathbf{yz}}\Psi = \varepsilon\Psi. \tag{145}$$

$\Psi^\intercal = (\Psi_e, \Psi_h)^\intercal$ is a four component vector which contains a two component vector Ψ_e representing the electrons and similarly a two component vector Ψ_h for the holes. In a normal metal electrons and holes move separately and are decoupled. This changes as soon as superconductivity is induced. In the superconducting surface, the electron and hole states are coupled to each other. This is described by the BdG equation. Therefore, the surface Hamiltonians for the superconducting $(x-y)$ plane and $(y-z)$ plane take the following form:

$$\mathbf{H}^{\mathbf{s}}_{\mathbf{xy}} = \begin{pmatrix} H^{xy} - U_0 - \mu & \Delta_0 e^{i\phi} \\ \Delta_0 e^{-i\phi} & -H^{xy} + U_0 + \mu \end{pmatrix}, \qquad \mathbf{H}^{\mathbf{s}}_{\mathbf{yz}} = \begin{pmatrix} H^{yz} - U_0 - \mu & \Delta_0 e^{i\phi} \\ \Delta_0 e^{-i\phi} & -H^{yz} + U_0 + \mu \end{pmatrix}, \tag{146}$$

and the corresponding BdG equations

$$\mathbf{H}^{\mathbf{s}}_{\mathbf{xy}}\Psi_s = \varepsilon\Psi_s, \qquad \mathbf{H}^{\mathbf{s}}_{\mathbf{yz}}\Psi_s = \varepsilon\Psi_s. \tag{147}$$

Note the simple form of the diagonal elements due to the TR invariance of the surface state Hamiltonian. These are all the Hamiltonians needed for the calculation of the Josephson effect in topological insulator planar, step and edge junctions. The setups are drawn in Fig. 16. The junctions are divided into three regions: region I and III denote topological superconducting planes and region II denotes a topological insulator plane (which is normal conducting). We are doing our calculations in the small junction limit, $L \ll W$, where W is the width in $y-$direction, which is still finite. The superconducting regions are assumed to be infinite on the open sides.

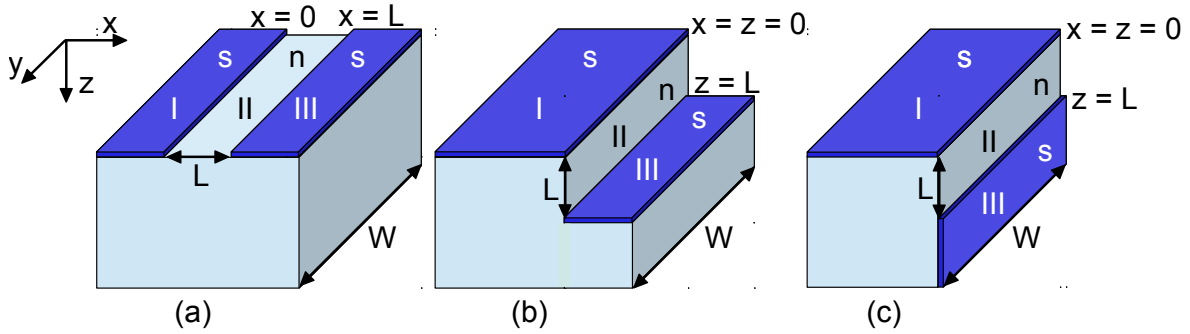

Figure 16: Schematics of the three topological junctions: (a) planar junction, (b) step junction, (c) edge junction. The blue planes are the superconductors inducing p-wave superconductivity in the surface of the topological insulator. The superconducting regions (s) are referred to as region I and III. The junction in between is the normal conducting (n) surface of the topological insulator (region II).

In general, regions I and III are topological superconductors and thus described by the BdG Eqs. (147). Furthermore, it is assumed that there is an electrostatic potential U in the three regions which can be adjusted independently by a gate voltage or doping. The zero potential is chosen to be in region II. In region I and III the potential is $U = -U_0$. Moreover, we use $U_0 \gg |\mu - \varepsilon_0|, \varepsilon$. This means that the Fermi wave length λ_F' in the superconductor is sufficiently small, such that $\lambda_F' \ll \xi, \lambda_F$, where $\lambda_F = \hbar v_F/\mu$ is the Fermi wave length in the normal region II and $\xi = \hbar v_F/\Delta_0$ is the superconducting coherence length. In this regime of a heavily doped superconductor with $|k_y| \leq |(\mu - \varepsilon_0)/\hbar v_F|$ the wave functions can be simplified. In addition, it is assumed that the interface is smooth and impurity free on the scale of ξ.

When the calculation is done for the different setups, it can soon be seen, that the results of the planar junction can be derived from the step junction by a simple change of variables. This is why the main part of the discussion is always about the step junction, with the intention, that it includes the discussion of the planar case.

In the next section, we will talk about the interfaces. The most common boundary condition to describe interfaces is the continuity of the wave functions at the interfaces. But for Hamiltonians with TR symmetry, a boundary may be described in terms of a more general condition by including a very thin potential barrier at the interface.

4.1 Boundary conditions

The usual boundary conditions are the continuity of the wave functions and current conservation. We derive a different set of boundary conditions, which fulfills the usual condition of current conservation but is more general than the continuity of the wave functions. More specifically, it includes the continuity of the wave functions as a special case.

4.1.1 Current conservation

Naturally, the current has to be conserved at the interfaces. In second quantization we can calculate the current density operator $\mathbf{j}(\mathbf{r},t)$ by using Heisenberg's equation of motion for the probability density $\rho(\mathbf{r},t)=\Psi^\dagger(\mathbf{r},t)\Psi(\mathbf{r},t)$:

$$i\hbar\frac{\partial\rho(\mathbf{r},t)}{\partial t}=[\rho(\mathbf{r},t),H], \tag{148}$$

and the continuity equation

$$\nabla\cdot\mathbf{j}+\frac{\partial\rho}{\partial t}=0. \tag{149}$$

In second quantization we have $\mathcal{H}=\int dr\Psi^\dagger(\mathbf{r},t)H(\mathbf{r},t)\Psi(\mathbf{r},t)$ where $H(\mathbf{r},t)$ is the Hamiltonian density. $\Psi(\mathbf{r},t)^\intercal=(\Psi_e,\Psi_h)^\intercal$ denote the wave functions.

Independent of whether we are dealing with a topological insulator or superconductor, the current operator in the $(x-y)$ plane becomes:

$$\mathbf{j_{xy}}=\begin{pmatrix}-v_F^{xy}\Psi_e^\dagger\sigma_y\Psi_e+v_F^{xy}\Psi_h^\dagger\sigma_y\Psi_h\\ v_F^{xy}\Psi_e^\dagger\sigma_x\Psi_e-v_F^{xy}\Psi_h^\dagger\sigma_x\Psi_h\\ 0\end{pmatrix}. \tag{150}$$

Similarly in the $(y-z)$ plane the current becomes

$$\mathbf{j_{yz}}=\begin{pmatrix}0\\ -v_F^{yz}\Psi_e^\dagger\sigma_z\Psi_e+v_F^{xy}\Psi_h^\dagger\sigma_z\Psi_h\\ v_F^{yz}\frac{A_1}{A_2}\Psi_e^\dagger\sigma_y\Psi_e-v_F^{yz}\frac{A_1}{A_2}\Psi_h^\dagger\sigma_y\Psi_h\end{pmatrix}. \tag{151}$$

In the step junction, the current which flows in $x-$direction is conserved by flowing in $z-$direction in region II.

4.1.2 Hermiticity of the total Hamiltonian

Planar junction

In a TR invariant system an interface between a superconducting and a normal conducting region can be described by a single parameter which determines the scattering at the interface [27]. Since the normal conducting junctions are described by TR-invariant Hamiltonians, we derive such a boundary condition similar to Ref. [27] for our normal conducting junctions. To explain the idea of the method, we derive the boundary conditions for the planar junction in detail.

The Hamiltonian for the entire system is given by $\mathbf{H^s_{xy}}$ for $x<0$, $\mathbf{H^n_{xy}}$ for $0<x<L$ and $\mathbf{H^s_{xy}}$ for $x>L$. We demand that this total Hamiltonian $\mathcal{H}$ is hermitian. We proceed by doing an integration by parts, requiring all the surface terms have to vanish. In second quantization

$$\mathcal{H}=\int_{-\infty}^{\infty}dy\left[\int_{-\infty}^{0}dx+\int_0^L dx+\int_L^\infty dx\right]\Psi^\dagger H\Psi \tag{152}$$

has to be hermitian. We simplify the problem by considering only one interface for the moment. Then, for the first interface, the Hamiltonian $\mathcal{H}_\mathcal{I}$ with $\mathbf{H^s_{xy}}$ for $x<0$, $\mathbf{H^n_{xy}}$ for $0<x$ shall be hermitian. This means, when doing an integration by parts all the surface terms have to vanish:

$$\begin{aligned}
&\mathcal{H}_\mathcal{I} = \int_{-\infty}^{\infty} dy \left[\int_{-\infty}^{0} dx + \int_{0}^{\infty} dx \right] \Psi^\dagger H \Psi = \\
&\int_{-\infty}^{\infty} dy \left[\begin{pmatrix} \Psi_e^{sI} \\ \Psi_h^{sI} \end{pmatrix}^\dagger i\hbar v^{xy}_{F,I} \begin{pmatrix} \sigma_y & 0 \\ 0 & -\sigma_y \end{pmatrix} \begin{pmatrix} \Psi_e^{sI} \\ \Psi_h^{sI} \end{pmatrix} \Big|_{x\to 0^-} - \begin{pmatrix} \Psi_e^{II} \\ \Psi_h^{II} \end{pmatrix}^\dagger i\hbar v^{xy}_{F,II} \begin{pmatrix} \sigma_y & 0 \\ 0 & -\sigma_y \end{pmatrix} \begin{pmatrix} \Psi_e^{II} \\ \Psi_h^{II} \end{pmatrix} \Big|_{x\to 0^+} \right] \\
&- \int dy \int dx \ldots,
\end{aligned} \tag{153}$$

where $v^{xy}_{F,I}$ is the Fermi velocity in region I, $v^{xy}_{F,II}$ and $v^{xy}_{F,III}$ in region II and III respectively. This leads to the boundary condition

$$\Psi^{sI\dagger}_{e/h} v^{xy}_{F,I} \sigma_y \Psi^{sI}_{e/h}|_{x\to 0^-} = \Psi^{II\dagger}_{e/h} v^{xy}_{F,II} \sigma_y \Psi^{II}_{e/h}|_{x\to 0^+} \tag{154}$$

for the first interface. An analogous argumentation leads to the boundary condition

$$\Psi^{II\dagger}_{e/h} v^{xy}_{F,II} \sigma_y \Psi^{II}_{e/h}|_{x\to L^-} = \Psi^{sIII\dagger}_{e/h} v^{xy}_{F,III} \sigma_y \Psi^{sIII}_{e/h}|_{x\to L^+} \tag{155}$$

for the second interface. It can be seen, that we get the same boundary conditions for the electrons and the holes. In a next step, a general relation between $\Psi^{sI}|_{x\to 0^+}$ and $\Psi^{II}|_{x\to 0^+}$ is derived. The functions hereafter refer only to the electron part, but the index "e" is omitted for simplicity. (It is exactly the same derivation for the hole part, with the exception of a sign change during the calculation which cancels out in the end.)
At first, we solve the equation

$$\sigma_y = U^\dagger \sigma_y U. \tag{156}$$

The identity matrix $\mathbb{I}$ and the three Pauli matrices σ_i $(i = x, y, z)$ form a basis for 2×2 matrices. In this case

$$U = e^{-\alpha\sigma_x - i\beta\mathbb{I} - i\gamma\sigma_y - \delta\sigma_z} \tag{157}$$

is a general solution for Eq. (156). This can be physically interpreted by considering a thin barrier of width d extending from $x = 0$ to $x = d$. Consequently, in this region we have to include an additional constant term V consisting of both, potential and magnetic parts,

$$V(x) = A\mathbb{I} + B\sigma_x + C\sigma_z + D\sigma_y, \tag{158}$$

where A, B, C and D are real in order that the Hamiltonian is hermitian. A can be thought of as a potential, and B, C and D as being proportional to the three components of a magnetic field which has a Zeeman coupling to the spin of the electron. We will eventually be interested in the limit of a δ-function barrier, so that $A, B, C, D \to \infty$ and $d \to 0$, keeping Ad, Bd, Cd and Dd fixed. The Hamiltonian in the region $0 < x < d$ is now given by

$$H_d = \varepsilon_0^{xy} - i\hbar v_F^{xy}(\sigma_x\partial_y - \sigma_y\partial_x) - \mu + A\mathbb{I} + B\sigma_x + C\sigma_z + D\sigma_y. \tag{159}$$

We look for a state with energy E and momentum k_y in the $y-$direction. The corresponding wave function is of the form:

$$\psi(x, y, t) = f(x)e^{ik_y y - iEt}. \tag{160}$$

In the region $0 < x < d$ it satisfies the equation

$$(\varepsilon_0^{xy} + \hbar v_F^{xy}\sigma_x\partial_y + i\hbar v_F^{xy}\sigma_y\partial_x - \mu + A\mathbb{I} + B\sigma_x + C\sigma_z + D\sigma_y)f = Ef. \tag{161}$$

Since we are interested in the limit $A, B, C, D \to \infty$, we can ignore the terms of finite order (terms of E, k_y, ε_0^{xy} and μ). The equation then can be solved with

$$f(x) = e^{x(iA\sigma_y + B\sigma_z - C\sigma_x + iD\mathbb{I})/v_F^{xy}} \tag{162}$$

and thus

$$f(d) = e^{d(iA\sigma_y + B\sigma_z - C\sigma_x + iD\mathbb{I})/v_F^{xy}}. \tag{163}$$

Next we take the limit $A, B, C, D \to \infty$ and $d \to 0$ and keep $Ad = -v_F^{xy}\gamma$, $Bd = -v_F^{xy}\delta$, $Cd = -v_F^{xy}\alpha$ and $Dd = -v_F^{xy}\beta$ fixed. By superposing states with different values of E and k_y, we recognize that any wave function $\psi(x, y, t)$ must satisfy

$$\psi(0^+, y, t) = \psi(0^-, y, t) e^{-\alpha\sigma_x - i\beta I - i\gamma\sigma_y - \delta\sigma_z}. \tag{164}$$

By imposing invariance under TR (we know that our surface Hamiltonians are TR invariant), only one parameter (A) will be left and the other three parameters (B, C, D) must be zero, since they can be interpreted as arising from a magnetic field. TR invariance of the surface Hamiltonian for the electrons means $\mathcal{T}H\mathcal{T} = i\sigma_y H^*(-i\sigma_y) = \sigma_y H^* \sigma_y = H$. By applying this transformation, it can be seen that only γ (or A) can be nonzero if V is invariant under TR.
Using Eq. (154), the boundary condition for the first interface reads

$$\Psi^{II}_{e/h}|_{x\to 0^+} = \sqrt{\frac{v^{xy}_{F,I}}{v^{xy}_{F,II}}} e^{-i\gamma\sigma_y} \Psi^{sI}_{e/h}|_{x\to 0^-}, \tag{165}$$

and similarly, with Eq. (155), for the second interface

$$\Psi^{sIII}_{e/h}|_{x\to L^+} = \sqrt{\frac{v^{xy}_{F,II}}{v^{xy}_{F,III}}} e^{-i\gamma\sigma_y} \Psi^{II}_{e/h}|_{x\to L^-}. \tag{166}$$

In the planar case all the velocities are the same, as the same material and surface are used.
We refer to the fact that current conservation is fulfilled with the boundary conditions Eqs. (165 and 166).

Step junction
The Hamiltonian for the entire system is given by $\mathbf{H^s_{xy}}$ for $x < 0$, $\mathbf{H^n_{yz}}$ for $0 < z < L$ and $\mathbf{H^s_{xy}}$ for $x > 0$. As before, we demand that this total Hamiltonian is hermitian. Again we consider only one interface at a time and the Hamiltonian $\mathcal{H}_\mathcal{I}$ with $\mathbf{H^s_{xy}}$ for $x < 0$, $z = 0$, $\mathbf{H^n_{yz}}$ for $0 < z$, $x = 0$ shall be hermitian. This implies, the surface terms of the following equation have to vanish:

$$\begin{aligned}
&\mathcal{H}_\mathcal{I} = \int_{-\infty}^{\infty} dy \left[\int_{-\infty}^{0} dx + \int_{0}^{\infty} dz \right] \Psi^\dagger H \Psi = \\
&\int_{-\infty}^{\infty} dy \left[\begin{pmatrix} \Psi^{sI}_e \\ \Psi^{sI}_h \end{pmatrix}^\dagger i\hbar v^{xy}_{F,I} \begin{pmatrix} \sigma_y & 0 \\ 0 & -\sigma_y \end{pmatrix} \begin{pmatrix} \Psi^{sI}_e \\ \Psi^{sI}_h \end{pmatrix} \Big|_{x\to 0^-} + \begin{pmatrix} \Psi^{II}_e \\ \Psi^{II}_h \end{pmatrix}^\dagger i\hbar v^{yz}_{F,II} \frac{A_1}{A_2} \begin{pmatrix} \sigma_y & 0 \\ 0 & -\sigma_y \end{pmatrix} \begin{pmatrix} \Psi^{II}_e \\ \Psi^{II}_h \end{pmatrix} \Big|_{z\to 0^+} \right] \\
&- \int dy \int dx dz \ldots,
\end{aligned} \tag{167}$$

where $v^{xy}_{F,I}$ is the Fermi velocity in region I, $v^{yz}_{F,II}$ and $v^{xy}_{F,III}$ in region II and III respectively. This leads to the boundary condition

$$\Psi^{sI\dagger}_{e/h} v^{xy}_{F,I} \sigma_y \Psi^{sI}_{e/h}|_{x\to 0^-} = -\Psi^{II\dagger}_{e/h} v^{yz}_{F,II} \frac{A_1}{A_2} \sigma_y \Psi^{II}_{e/h}|_{z\to 0^+} \tag{168}$$

for the first interface. An analogous derivation leads to the boundary condition

$$\Psi^{II\dagger}_{e/h} v^{yz}_{F,II} \frac{A_1}{A_2} \sigma_y \Psi^{II}_{e/h}|_{z\to L^-} = -\Psi^{sIII\dagger}_{e/h} v^{xy}_{F,III} \sigma_y \Psi^{sIII}_{e/h}|_{x\to 0^+} \tag{169}$$

for the second interface. It can be seen that we have the same equation as in the planar case, just with a different sign. Thus, the solution for the first interface is

$$\Psi^{II}_{e/h}|_{z\to 0^+} = i\sqrt{\frac{v^{xy}_{F,I} A_2}{v^{yz}_{F,II} A_1}} e^{-i\gamma\sigma_y} \Psi^{sI}_{e/h}|_{x\to 0^-}, \tag{170}$$

and for the second interface

$$\Psi^{sIII}_{e/h}|_{x\to 0^+} = i\sqrt{\frac{v^{yz}_{F,II}A_1}{v^{xy}_{F,III}A_2}}e^{-i\gamma\sigma_y}\Psi^{II}_{e/h}|_{z\to L^-}. \tag{171}$$

Contrary to the planar junction, the velocities in region I and III are equal (both in $(x-y)$ plane) but different from the velocity in region II ($(y-z)$ plane). Current conservation is fulfilled with the boundary conditions (170, 171).

Edge junction

Completely analogously the boundary condition for the edge junction at $z = L$, $x = 0$ can be calculated:

$$\Psi^{II}_{e/h}|_{z\to 0^+} = i\sqrt{\frac{v^{xy}_{F,I}A_2}{v^{yz}_{F,II}A_1}}e^{-i\gamma\sigma_y}\Psi^{sI}_{e/h}|_{x\to 0^-}. \tag{172}$$

The boundary condition for the second interface is

$$\Psi^{sIII}_{e/h}|_{z\to L^+} = e^{-i\gamma\sigma_y}\Psi^{II}_{e/h}|_{z\to L^-}. \tag{173}$$

The above derived boundary conditions are used when the system is TR invariant. For a TR symmetry breaking system such more general boundary conditions would be more complicated, since the magnetic parts are nonzero. Thats why, for simplicity, we will use the continuity of the wave functions for TR invariant systems.

4.2 Planar junction

4.2.1 Solutions of the BdG equations

In all three junctions region I ($x < 0$, $z = 0$) is superconducting and described by the Hamiltonian $\mathbf{H^s_{xy}}$ and the corresponding BdG equations. We are looking for solutions of the BdG equations in the superconducting region which decay exponentially for $\varepsilon < \Delta_0$. In the regime $U_0 + \mu - \varepsilon_0^{xy} \gg \{\Delta_0, \varepsilon\}$ and $\varepsilon < \Delta_0$ we find

$$\Psi^{I\pm}_s(x,y) = \begin{pmatrix}\Psi^{I\pm}_{se}(x,y)\\ \Psi^{I\pm}_{sh}(x,y)\end{pmatrix} = e^{ik_y y \pm ik_x x + \kappa x}\begin{pmatrix} e^{\mp i\beta}\\ \mp ie^{\mp i\beta\pm i\alpha}\\ e^{-i\phi_I}\\ \mp ie^{-i\phi_I\pm i\alpha}\end{pmatrix}, \tag{174}$$

where $\beta = \arccos(\varepsilon/\Delta_0)$, $\sin(\alpha) = \frac{\hbar v_F^{xy} k_y}{U_0+\mu-\varepsilon_0^{xy}}$, $k_x = \sqrt{\frac{(U_0+\mu-\varepsilon_0^{xy})^2}{(\hbar v_F^{xy})^2} - k_y^2}$ and $\kappa = \frac{(U_0+\mu-\varepsilon_0^{xy})\Delta_0}{(\hbar v_F^{xy})^2 k_x}\sin(\beta)$. These solutions decay as $x \to -\infty$. The sign $\pm$ denotes the direction $\pm x$ of transport of the wave. The heavily doped regime ($U_0 \gg |\mu - \varepsilon_0^{xy}|, \varepsilon$) can be approximated with $\alpha = 0$ and thus with the wave functions

$$\Psi^{I\pm}_s(x,y) = e^{ik_y y \pm ik_x x + \kappa x}\begin{pmatrix} e^{\mp i\beta}\\ \mp ie^{\mp i\beta}\\ e^{-i\phi_I}\\ \mp ie^{-i\phi_I}\end{pmatrix}. \tag{175}$$

For the planar case the effective Hamiltonian in region II ($0 < x < L$, $z = 0$) is $\mathbf{H^n_{xy}}$. The solutions of the eigenvalue equation are superpositions of states in the form

$$\Psi^{II\pm}_e(x,y) = \begin{pmatrix}1\\ \mp ie^{\pm i\alpha(\varepsilon)}\\ 0\\ 0\end{pmatrix}e^{ik_y y \pm ik_x(\varepsilon)x}, \qquad \Psi^{II\pm}_h(x,y) = \begin{pmatrix}0\\ 0\\ 1\\ \mp ie^{\pm i\alpha(-\varepsilon)}\end{pmatrix}e^{ik_y y \pm ik_x(-\varepsilon)x}, \tag{176}$$

where $\sin(\alpha(\varepsilon)) = \frac{\hbar v_F^{xy} k_y}{\varepsilon+\mu-\varepsilon_0^{xy}}$ and $k_x(\varepsilon) = \sqrt{\frac{(\varepsilon+\mu-\varepsilon_0^{xy})^2}{(\hbar v_F^{xy})^2} - k_y^2}$.
Region III of the planar junction is described by $\mathbf{H_{xy}^s}$. In contrast to the wave functions in region I, these need to decay for $x \to \infty$. Consequently, we get similar solutions of the BdG equation in region III (for $x > L$, $z = 0$) but with some changes in sign:

$$\Psi_s^{III\pm}(x,y) = \begin{pmatrix} \Psi_{se}^{III\pm}(x,y) \\ \Psi_{sh}^{III\pm}(x,y) \end{pmatrix} = e^{ik_y y \pm ik_x(x-L)-\kappa(x-L)} \begin{pmatrix} e^{\pm i\beta} \\ \mp i e^{\pm i\beta \pm i\alpha} \\ e^{-i\phi_{III}} \\ \mp i e^{-i\phi_{III} \pm i\alpha} \end{pmatrix}, \tag{177}$$

where $\beta = \arccos(\varepsilon/\Delta_0)$, $\sin(\alpha) = \frac{\hbar v_F^{xy} k_y}{U_0+\mu-\varepsilon_0^{xy}}$, $k_x = \sqrt{\frac{(U_0+\mu-\varepsilon_0^{xy})^2}{(\hbar v_F^{xy})^2} - k_y^2}$ and $\kappa = \frac{(U_0+\mu-\varepsilon_0^{xy})\Delta_0}{(\hbar v_F^{xy})^2 k_x}\sin(\beta)$.
These solutions decay for $x \to \infty$.
Here we also restrict ourselves to the heavily doped regime and use $\alpha = 0$, resulting in

$$\Psi_s^{III\pm}(x,y) = e^{ik_y y \pm ik_x(x-L)-\kappa(x-L)} \begin{pmatrix} e^{\pm i\beta} \\ \mp i e^{\pm i\beta} \\ e^{-i\phi_{III}} \\ \mp i e^{-i\phi_{III}} \end{pmatrix}. \tag{178}$$

4.2.2 Boundary conditions

The Hamiltonians describing our system are TR invariant and we can use the more general boundary conditions with the small potential barrier at the interface. For the first interface (between region I and II), the most general boundary conditions are:

$$[a_{e,h}^+ \Psi_{e,h}^{II+}(x,y) + a_{e,h}^- \Psi_{e,h}^{II-}(x,y)]|_{x\to 0^+} = e^{-i\gamma_1\sigma_y}[\alpha^+ \Psi_{s(e,h)}^{I+}(x,y) + \alpha^- \Psi_{s(e,h)}^{I-}(x,y)]|_{x\to 0^-}. \tag{179}$$

The indices e, h denote the electron and hole wave functions. In the superconducting wave function, e refers to the first two entries and h to the last two entries of the four component wave vectors. $a_{e,h}^{\pm}$ are the amplitudes of the electron and hole wave functions propagating in $\pm x-$direction. They are different for electrons and holes in the second region. In the superconducting surface, on the contrary, the electron and hole wave functions have the same amplitudes $\alpha^{\pm}$, as there the electron and holes are coupled to each other via the BdG equations. For the interface between region II and III we get similar equations:

$$[\beta^+ \Psi_{s(e,h)}^{III+}(x,y) + \beta^- \Psi_{s(e,h)}^{III-}(x,y)]|_{x\to L^+} = e^{-i\gamma_2\sigma_y}[a_{e,h}^+ \Psi_{e,h}^{II+}(x,y) + a_{e,h}^- \Psi_{e,h}^{II-}(x,y)]|_{x\to L^-}, \tag{180}$$

with the amplitudes $\beta^{\pm}$ for the superconducting wave functions propagating in $\pm x-$direction. The boundary conditions yield eight equations for eight variables ($a_{e,h}^{\pm}$, $\alpha^{\pm}$ and $\beta^{\pm}$) and two parameters γ_1 and γ_2 for the "potential" of the first and the second interface respectively. We write the eight equations in matrix representation:

$$M \cdot \begin{pmatrix} a_e^+ \\ a_e^- \\ a_h^+ \\ a_h^- \\ \alpha^+ \\ \alpha^- \\ \beta^+ \\ \beta^- \end{pmatrix} = 0, \tag{181}$$

with

$$M = \begin{pmatrix} M_{11} & M_{12} \\ M_{21} & M_{22} \end{pmatrix}, \tag{182}$$

where

$$M_{11} = \begin{pmatrix} \Psi_e^+ 01 & \Psi_e^- 01 & 0 & 0 \\ \Psi_e^+ 02 & \Psi_e^- 02 & 0 & 0 \\ 0 & 0 & \Psi_h^+ 01 & \Psi_h^- 01 \\ 0 & 0 & \Psi_h^+ 02 & \Psi_h^- 02 \end{pmatrix} = \begin{pmatrix} 1 & 1 & 0 & 0 \\ -ie^{i\alpha(\varepsilon)} & ie^{-i\alpha(\varepsilon)} & 0 & 0 \\ 0 & 0 & 1 & 1 \\ 0 & 0 & -ie^{i\alpha(-\varepsilon)} & ie^{i\alpha(-\varepsilon)} \end{pmatrix}, \tag{183}$$

$$
\begin{aligned}
M_{12} &= \begin{pmatrix}
\cos\gamma_1\Psi^{I+}_{se}01 - \sin\gamma_1\Psi^{I+}_{se}02 & \cos\gamma_1\Psi^{I-}_{se}01 - \sin\gamma_1\Psi^{I-}_{se}02 & 0 & 0 \\
\sin\gamma_1\Psi^{I+}_{se}01 + \cos\gamma_1\Psi^{I+}_{se}02 & \sin\gamma_1\Psi^{I-}_{se}01 + \cos\gamma_1\Psi^{I-}_{se}02 & 0 & 0 \\
\cos\gamma_1\Psi^{I+}_{sh}01 - \sin\gamma_1\Psi^{I+}_{sh}02 & \cos\gamma_1\Psi^{I-}_{sh}01 - \sin\gamma_1\Psi^{I-}_{sh}02 & 0 & 0 \\
\sin\gamma_1\Psi^{I+}_{sh}01 + \cos\gamma_1\Psi^{I+}_{sh}02 & \sin\gamma_1\Psi^{I-}_{sh}01 + \cos\gamma_1\Psi^{I-}_{sh}02 & 0 & 0
\end{pmatrix} \\
&= \begin{pmatrix}
e^{-i\gamma_1 - i\beta} & e^{i\gamma_1 + i\beta} & 0 & 0 \\
-ie^{i\gamma_1 - i\beta} & ie^{-i\gamma_1 + i\beta} & 0 & 0 \\
e^{-i\gamma_1 - i\phi_I} & e^{i\gamma_1 - i\phi_I} & 0 & 0 \\
-ie^{i\gamma_1 - i\phi_I} & ie^{-i\gamma_1 - i\phi_I} & 0 & 0
\end{pmatrix},
\end{aligned}
\tag{184}
$$

$$
\begin{aligned}
M_{21} &= \begin{pmatrix}
\Psi^+_e L1 & \Psi^-_e L1 & 0 & 0 \\
\Psi^+_e L2 & \Psi^-_e L2 & 0 & 0 \\
0 & 0 & \Psi^+_h L1 & \Psi^-_h L1 \\
0 & 0 & \Psi^+_h L2 & \Psi^-_h L2
\end{pmatrix} \\
&= \begin{pmatrix}
e^{ik_x(\varepsilon)L} & e^{-ik_x(\varepsilon)L} & 0 & 0 \\
-ie^{i\alpha(\varepsilon)}e^{ik_x(\varepsilon)L} & ie^{-i\alpha(\varepsilon)}e^{-ik_x(\varepsilon)L} & 0 & 0 \\
0 & 0 & e^{ik_x(-\varepsilon)L} & e^{-ik_x(-\varepsilon)L} \\
0 & 0 & -ie^{i\alpha(-\varepsilon)}e^{ik_x(-\varepsilon)L} & ie^{i\alpha(-\varepsilon)}e^{-ik_x(-\varepsilon)L}
\end{pmatrix},
\end{aligned}
\tag{185}
$$

$$
\begin{aligned}
M_{22} &= \begin{pmatrix}
0 & 0 & \cos\gamma_2\Psi^{III+}_{se}L1 + \sin\gamma_2\Psi^{III+}_{se}L2 & \cos\gamma_2\Psi^{III-}_{se}L1 + \sin\gamma_2\Psi^{III-}_{se}L2 \\
0 & 0 & \cos\gamma_2\Psi^{III+}_{se}L2 - \sin\gamma_2\Psi^{III+}_{se}L1 & \cos\gamma_2\Psi^{III-}_{se}L2 - \sin\gamma_2\Psi^{III-}_{se}L1 \\
0 & 0 & \cos\gamma_2\Psi^{III+}_{sh}L1 + \sin\gamma_2\Psi^{III+}_{sh}L2 & \cos\gamma_2\Psi^{III-}_{sh}L1 + \sin\gamma_2\Psi^{III-}_{sh}L2 \\
0 & 0 & \cos\gamma_2\Psi^{III+}_{sh}L2 - \sin\gamma_2\Psi^{III+}_{sh}L1 & \cos\gamma_2\Psi^{III-}_{sh}L2 - \sin\gamma_2\Psi^{III-}_{sh}L1
\end{pmatrix} \\
&= \begin{pmatrix}
0 & 0 & e^{i\gamma_2 - i\beta} & e^{-i\gamma_2 + i\beta} \\
0 & 0 & -ie^{-i\gamma_2 - i\beta} & ie^{i\gamma_2 + i\beta} \\
0 & 0 & e^{i\gamma_2 - i\phi_{III}} & e^{-i\gamma_2 - i\phi_{III}} \\
0 & 0 & -ie^{-i\gamma_2 - i\phi_{III}} & ie^{i\gamma_2 - i\phi_{III}}
\end{pmatrix}.
\end{aligned}
\tag{186}
$$

The first label $(0, L)$ behind the wave functions Ψ indicates the $x-$position at which the wave function is evaluated and the second label $(1, 2)$ denotes the component.
Any matrix equation $A \cdot \vec{x} = 0$, where A is a $n \times n$ square matrix and $\vec{x}$ a n component vector of solution variables, is solved by the trivial solution $\vec{x} = 0$. If the determinant of A is nonzero, the trivial solution is the only solution of the equation. In our case this implies, that our wave functions are 0 as their components are 0. But since we want nontrivial solutions, we need the determinant of the matrix to be zero: $\det(M) = 0$. We solve the equation for the phase difference $\phi = \phi_I - \phi_{III}$ of the two superconducting regions by writing the phases of the superconductors in terms of the phase difference ϕ: $\phi_I = \phi/2$ and $\phi_{III} = -\phi/2$. We get:

$$
\begin{aligned}
\cos(\phi) = &\left(\cos(k_x(\varepsilon)L)\cos(k_x(-\varepsilon)L) + \frac{\sin(k_x(\varepsilon)L)\sin(k_x(-\varepsilon)L)}{\cos(\alpha(\varepsilon))\cos(\alpha(-\varepsilon))}\right)\cos(2\beta) \\
&+ \left(\frac{\sin(k_x(\varepsilon)L)\cos(k_x(-\varepsilon)L)}{\cos(\alpha(\varepsilon))} - \frac{\cos(k_x(\varepsilon)L)\sin(k_x(-\varepsilon)L)}{\cos(\alpha(-\varepsilon))}\right)\sin(2\beta) \\
&- \sin(k_x(\varepsilon)L)\sin(k_x(-\varepsilon)L)\tan(\alpha(\varepsilon))\tan(\alpha(-\varepsilon)).
\end{aligned}
\tag{187}
$$

We find that Eq. (187) is independent of the interface parameters γ_1 and γ_2. This means, we obtain the same expression for $\cos(\phi)$ in the special case $\gamma_1 = \gamma_2 = 0$ which corresponds to the continuity of the wave functions. Naturally, the wave functions look different, if we use the boundary conditions with the potential barriers γ_1 and γ_2 at the boundaries than if we only demand continuity. In our general case the wave functions are functions of γ_1 and γ_2.

4.2.3 Josephson current

In a next step, a finite width W is introduced to quantize the transverse wave vectors, $k_y \to k_{yn}$, $n = 0, 1, 2, \ldots$. With $\rho_n(\varepsilon, \phi)$, the density of states in mode n, the Josephson current at zero temperature is given by:

$$
J(\phi) = -\frac{2e}{\hbar}\frac{d}{d\phi}\int_0^\infty d\varepsilon \sum_{n=0}^{\infty} \rho_n(\varepsilon, \phi)\varepsilon. \tag{188}
$$

With the "infinite mass" boundary conditions [28] at $y = 0$ and $y = W$ quantized values $k_{yn} = (n + 1/2)\pi/W$ can be used [29]. As a result of this quantization, we get $k_{xn} = \sqrt{((\mu - \varepsilon_0^{xy})/\hbar v_F^{xy})^2 - k_{yn}^2}$, which means, the lowest $N(\mu) = (\mu - \varepsilon_0^{xy})W/(\pi\hbar v_F^{xy})$ modes are propagating as k_{xn} is real, while the higher modes are evanescent, since for these modes k_{xn} is imaginary. The analysis of the Josephson current is done in the short-junction regime where the length L of the normal region is small relative to the superconducting coherence length ξ. This requires $\Delta_0 \ll \hbar v_F^{xy}/L$. This implicates that the energy ε is small, making the following simplifications valid to leading order in the small parameter $\Delta_0 L/\hbar v_F^{xy}$: $\alpha(-\varepsilon) \approx \alpha(\varepsilon) \approx \alpha(0) =: \alpha$ and $k_x(-\varepsilon) \approx k_x(\varepsilon) \approx k_x(0) =: k_{xn}$. The solution is a single bound state per mode:

$$\varepsilon_n(\phi) = \Delta_0 \sqrt{1 - \tau_n \sin^2(\phi/2)}, \tag{189}$$

$$\tau_n = \frac{k_{xn}^2}{k_{xn}^2 \cos^2(k_{xn}L) + \left(\frac{\mu - \varepsilon_0^{xy}}{\hbar v_F^{xy}}\right)^2 \sin^2(k_{xn}L)}. \tag{190}$$

In Eq. (189) we have written the energy in a special form. This enables us to compare it to the expression of the energy which we derived in chapter 2 for Andreev scattering. We see that the Andreev bound states of a topological insulator junction look like those in a normal (trivial) Josephson junction. Consequently, we may interpret τ_n as the transmission probability of region II − the conducting surface of the topological insulator. By using $\rho_n(\varepsilon, \phi) = \delta(\varepsilon - \varepsilon_n(\phi))$ the supercurrent due to the discrete spectrum becomes:

$$J(\phi) = \frac{e\Delta_0}{2\hbar} \sum_{n=0}^{\infty} \frac{\tau_n \sin(\phi)}{\sqrt{1 - \tau_n \sin^2(\phi/2)}} = \frac{e\Delta_0}{\hbar} \frac{W}{2\pi} \int_0^{\infty} \frac{\tau_n \sin(\phi)}{\sqrt{1 - \tau_n \sin^2(\phi/2)}} dk_{yn}. \tag{191}$$

Contributions to the supercurrent from the continuous spectrum are smaller by a factor proportional to L/ξ where ξ is the superconducting coherence length and may be neglected in the short-junction regime [30]. For $L \ll W$ the summation over n may be replaced by an integration. The integral can be solved numerically. Since the chemical potential μ can be tuned (e.g. by a gate voltage), it makes sense to plot the critical Josephson current as a function of the chemical potential with respect to the Dirac point energy. This is done in Fig. 17 (blue line). The current is a combination of propagating (real k_x) and evanescent (imaginary k_x) waves. The red line in Fig. 17 shows the contribution of the propagating waves only. We can see that the contribution of the evanescent waves can be neglected for $|\Lambda| = |\frac{\mu - \varepsilon_0^{xy}}{\hbar v_F^{xy}}| \geq 2$ but becomes dominant for $|\Lambda| \to 0$. The limiting behaviour at the Dirac point ($|\mu - \varepsilon_0^{xy}| \ll \hbar v_F^{xy}/L$) for a short junction can be calculated analytically by doing a Taylor expansion of the sum around τ_n (the calculation can be found in the analysis of the step junction). This results in

$$J(\phi) = \frac{e\Delta_0}{2\hbar} \frac{W}{\pi L} \cos(\phi/2) \arctan(\sin(\phi/2)) \quad \text{for} \quad |\mu - \varepsilon_0^{xy}| \ll \hbar v_F^{xy}/L, \tag{192}$$

which leads to the critical current

$$J_{c,min} = 0.21 \frac{e\Delta_0}{\hbar} \frac{W}{L}. \tag{193}$$

This is plotted in Fig. 17 (red line). In the opposite regime ($|\mu - \varepsilon_0^{xy}| \gg \hbar v_F^{xy}/L$) the critical current becomes:

$$J_{c,slope} = 0.61 \frac{e\Delta_0}{\hbar} \frac{(\mu - \varepsilon_0^{xy})W}{\pi\hbar v_F^{xy}}, \tag{194}$$

which is plotted in Fig. 17 (black line). In this regime the oscillating behaviour of the critical current can be considered as a small deviation.

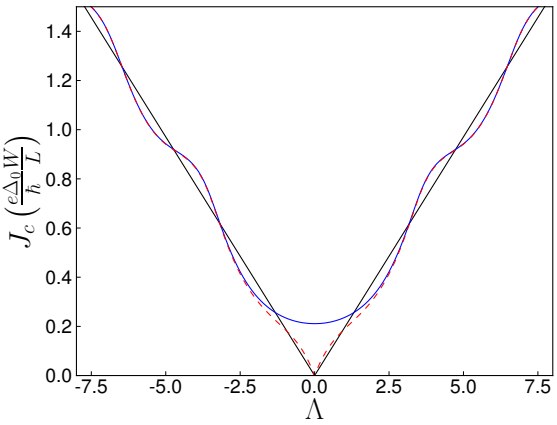

Figure 17: Critical current J_c of a planar Josephson junction, as a function of $\Lambda = \frac{\mu - \varepsilon_0^{xy}}{\hbar v_F^{xy}}$ (where the chemical potential is the tunable parameter) in the normal region (blue). The black lines are the asymptotes and the red lines show the contribution of the propagating waves only.

In 2006 Titov and Beenakker [31] made a similar calculation of the "Josephson effect in ballistic graphene". In graphene low-lying excitations are also described by a Dirac equation $H_0 = -i\hbar v_F(\sigma_x\partial_x + \sigma_y\partial_y)$. But in contrast to a topological insulator, the energy spectrum of graphene consists of two Dirac cones instead of one. Due to this degeneracy, graphene gives twice the Josephson current of a topological insulator.

4.3 Step junction

4.3.1 Solutions of the BdG equations

Region I ($x < 0$, $z = 0$) is equal to region I of the planar case and we use the solutions of the BdG in the heavily doped regime ($U_0 \gg |\mu - \varepsilon_0^{xy}|, \varepsilon$):

$$\Psi_s^{I\pm}(x,y) = e^{ik_y y \pm ik_x x + \kappa x}\begin{pmatrix} e^{\mp i\beta} \\ \mp ie^{\mp i\beta} \\ e^{-i\phi_I} \\ \mp ie^{-i\phi_I} \end{pmatrix}. \tag{195}$$

The effective Hamiltonian in region II ($0 < z < L$, $x = 0$) for the step junction is $\mathbf{H_{yz}^n}$. The solutions of the eigenvalue problem are any linear combination of the eigenstates

$$\Psi_e^{II\pm}(y,z) = \frac{1}{\sqrt{1+\sin(\alpha(\varepsilon))}}\begin{pmatrix} \mp i\cos(\alpha(\varepsilon)) \\ 1+\sin(\alpha(\varepsilon)) \\ 0 \\ 0 \end{pmatrix} e^{ik_y y \pm ik_z(\varepsilon)z}, \tag{196}$$

$$\Psi_h^{II\pm}(y,z) = \frac{1}{\sqrt{1+\sin(\alpha(-\varepsilon))}}\begin{pmatrix} 0 \\ 0 \\ \mp i\cos(\alpha(-\varepsilon)) \\ 1+\sin(\alpha(-\varepsilon)) \end{pmatrix} e^{ik_y y \pm ik_z(-\varepsilon)z}, \tag{197}$$

where $\sin(\alpha(\varepsilon)) = \frac{\hbar v_F^{yz} k_y}{\varepsilon + \mu - \varepsilon_0^{yz}}$ and $\frac{A_1}{A_2}k_z(\varepsilon) = \sqrt{\frac{(\varepsilon+\mu-\varepsilon_0^{yz})^2}{(\hbar v_F^{yz})^2} - k_y^2}$.

The solution of the BdG equations of region III ($x > 0$, $z = L$) with the Hamiltonian $\mathbf{H_{xy}^s}$ are similar to those of the planar case:

$$\Psi_s^{III\pm}(x,y) = \begin{pmatrix} \Psi_{se}^{III\pm}(x,y) \\ \Psi_{sh}^{III\pm}(x,y) \end{pmatrix}^{\pm} = e^{ik_y y \pm ik_x(x) - \kappa(x)}\begin{pmatrix} e^{\pm i\beta} \\ \mp ie^{\pm i\beta \pm i\alpha} \\ e^{-i\phi_{III}} \\ \mp ie^{-i\phi_{III} \pm i\alpha} \end{pmatrix}, \tag{198}$$

where $\beta = \arccos(\varepsilon/\Delta_0)$, $\sin(\alpha) = \frac{\hbar v_F^{xy} k_y}{U_0+\mu-\varepsilon_0^{xy}}$, $k_x = \sqrt{\frac{(U_0+\mu-\varepsilon_0^{xy})^2}{(\hbar v_F^{xy})^2} - k_y^2}$ and $\kappa = \frac{(U_0+\mu-\varepsilon_0^{xy})\Delta_0}{(\hbar v_F^{xy})^2 k_x}\sin(\beta)$. These solutions decay as $x \to \infty$. We again assume heavy doping of the superconducting region such that the wave functions can be simplified with $\alpha = 0$:

$$\Psi_s^{III\pm}(x,y) = e^{ik_y y \pm ik_x(x) - \kappa(x)} \begin{pmatrix} e^{\pm i\beta} \\ \mp i e^{\pm i\beta} \\ e^{-i\phi_{III}} \\ \mp i e^{-i\phi_{III}} \end{pmatrix}. \tag{199}$$

4.3.2 Boundary conditions

In the step junction the Hamiltonians describing the three regions are TR invariant too. We use the boundary condition with the thin potential barrier. For the first interface (between region I and II) we have:

$$[a_{e,h}^{+}\Psi_{e,h}^{II+}(y,z) + a_{e,h}^{-}\Psi_{e,h}^{II-}(y,z)]|_{z\to 0^+} = i\sqrt{\frac{v_F^{xy}A_2}{v_F^{yz}A_1}} e^{-i\gamma_1\sigma_y}[\alpha^{+}\Psi_{s(e,h)}^{I+}(x,y) + \alpha^{-}\Psi_{s(e,h)}^{I-}(x,y)]|_{x\to 0^-}. \tag{200}$$

The indices e, h denote the electron and the hole wave functions. In the superconducting wave function, e refers to the first two entries and h to the last two entries of the four component wave vectors. $a_{e,h}^{\pm}$ are the amplitudes of the electron and hole wave functions propagating in $\pm z-$direction. They are different for electrons and holes in the second region. In the superconductor on the contrary, the electron and hole wave functions have the same amplitudes $\alpha^{\pm}$ as there the electron and holes are coupled to each other via the BdG equations. For the interface between region II and III we get similar equations:

$$[\beta^{+}\Psi_{s(e,h)}^{III+}(x,y) + \beta^{-}\Psi_{s(e,h)}^{III-}(x,y)]|_{x\to 0^+} = i\sqrt{\frac{v_F^{yz}A_1}{v_F^{xy}A_2}} e^{-i\gamma_2\sigma_y}[a_{e,h}^{+}\Psi_{e,h}^{II+}(y,z) + a_{e,h}^{-}\Psi_{e,h}^{II-}(y,z)]|_{z\to L^-}. \tag{201}$$

In contrast to the planar junction, the velocities of the superconducting and normal regions are different, this is why they appear in the boundary conditions. The factor i appears because the sign of the discontinuous part changes at the interface.
With the same procedure like in the planar case − writing the eight equations in matrix representation and demanding nontrivial solutions for the coefficients − we get a similar condition for ϕ as in the planar case Eq. (187), but with different signs:

$$\begin{aligned} \cos(\phi) = &\left(\cos(k_z(\varepsilon)L)\cos(k_z(-\varepsilon)L) + \frac{\sin(k_z(\varepsilon)L)\sin(k_z(-\varepsilon)L)}{\cos(\alpha(\varepsilon))\cos(\alpha(-\varepsilon))}\right)\cos(2\beta) \\ &+ \left(\frac{\cos(k_z(\varepsilon)L)\sin(k_z(-\varepsilon)L)}{\cos(\alpha(-\varepsilon))} - \frac{\sin(k_z(\varepsilon)L)\cos(k_z(-\varepsilon)L)}{\cos(\alpha(\varepsilon))}\right)\sin(2\beta) \\ &- \sin(k_z(\varepsilon)L)\sin(k_z(-\varepsilon)L)\tan(\alpha(\varepsilon))\tan(\alpha(-\varepsilon)). \end{aligned} \tag{202}$$

As before, it is calculated in the heavily doped regime, meaning the parameters $\alpha \to 0$ in the superconducting regions.

4.3.3 Josephson current

To calculate the Josephson current, a finite width W is introduced to quantize the transverse wave vectors in region II, $k_y \to k_{yn}$, $n = 0, 1, 2, \ldots$. With $\rho_n(\varepsilon, \phi)$, the density of states of mode n, the Josephson current at zero temperature is given by:

$$J(\phi) = -\frac{2e}{\hbar}\frac{d}{d\phi}\int_0^\infty d\varepsilon \sum_{n=0}^{\infty} \rho_n(\varepsilon,\phi)\varepsilon. \tag{203}$$

Using again the "infinite mass" boundary conditions [28] at $y = 0$ and $y = W$, $k_{yn} = (n + 1/2)\pi/W$ is valid. This quantizes k_{zn} and $\frac{A_1}{A_2}k_{zn} = \sqrt{\left(\frac{\mu-\varepsilon_0^{yz}}{\hbar v_F^{yz}}\right)^2 - k_{yn}^2}$, which means the lowest $N(\mu - \varepsilon_0^{yz}) =$

$\left(\frac{\mu-\varepsilon_0^{yz}}{\hbar v_F^{yz}}\right)\frac{W}{\pi}$ modes are propagating as k_{zn} is real, while the higher modes are evanescent, since for these modes k_{zn} is imaginary. The analysis of the Josephson current is done in the short-junction regime where the length L of the normal region is small relative to the superconducting coherence length ξ. This requires $\Delta_0 \ll \hbar v_F^{yz}/L$ making $\alpha(-\varepsilon) \approx \alpha(\varepsilon) \approx \alpha(0) =: \alpha$ and $k_z(-\varepsilon) \approx k_z(\varepsilon) \approx k_z(0) =: k_{zn}$ a good approximation. The solution is a single bound state per mode:

$$\varepsilon_n(\phi) = \Delta_0\sqrt{1-\tau_n\sin^2(\phi/2)}, \tag{204}$$

$$\tau_n = \frac{\left(\frac{A_1}{A_2}k_{zn}\right)^2}{\left(\frac{A_1}{A_2}k_{zn}\right)^2\cos^2(k_{zn}L)+\left(\frac{\mu-\varepsilon_0^{yz}}{\hbar v_F^{yz}}\right)^2\sin^2(k_{zn}L)}. \tag{205}$$

We compare Eq. (204) to the energy modes of the usual Andreev reflection. This enables us to identify τ_n as the transmission probability of the topological insulator surface sandwiched between two heavily doped topological superconducting surfaces. We realize that the solutions of the step case are the same as those of the planar case (see Eq. (190)) with exception of the additional scaling factor $\frac{A_1}{A_2}$ in the step case. This scaling factor means, that the Fermi velocity in direction of transport ($z-$direction) is different from the velocity in transverse direction ($y-$direction).
By using $\rho_n(\varepsilon,\phi) = \delta(\varepsilon-\varepsilon_n(\phi))$ the supercurrent due to the discrete spectrum becomes

$$J(\phi) = \frac{e\Delta_0}{2\hbar}\sum_{n=0}^{\infty}\frac{\tau_n\sin(\phi)}{\sqrt{1-\tau_n\sin^2(\phi/2)}} = \frac{e\Delta_0}{\hbar}\frac{W}{2\pi}\int_0^{\infty}\frac{\tau_n\sin(\phi)}{\sqrt{1-\tau_n\sin^2(\phi/2)}}dk_{yn}. \tag{206}$$

As $L \ll W$, the summation over n may be replaced by an integration. The integral can be solved numerically. In Fig. 18 we plotted the Josephson current for different values of $\Lambda = \frac{\mu-\varepsilon_0^{yz}}{\hbar v_F^{yz}}\left(\frac{A_2 L}{A_1}\right)$, where the chemical potential μ is the parameter that can be tuned.

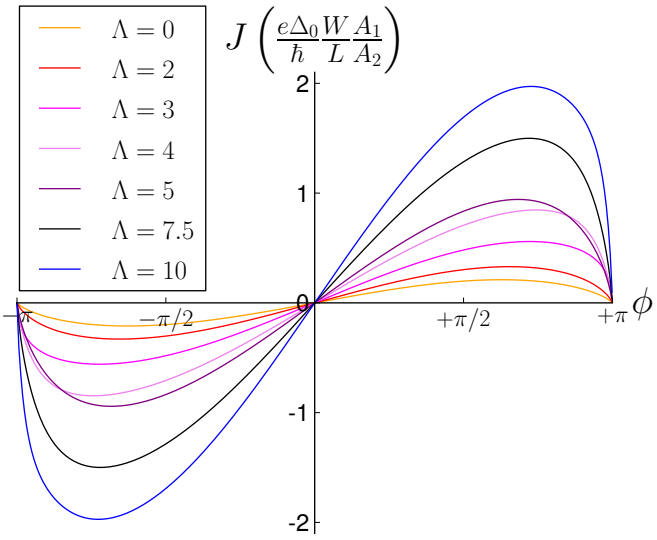

Figure 18: Current $J(\phi)$ of a Josephson junction for different values of $\Lambda = \frac{\mu-\varepsilon_0^{yz}}{\hbar v_F^{yz}}\left(\frac{A_2 L}{A_1}\right)$.

The $\Lambda = 0$ curve shows the small $\mu - \varepsilon_0^{yz}$ limit, which is calculated analytically later. The other curves are the numerical solutions of the integral in Eq. (206).
By maximizing the current with respect to ϕ, the critical Josephson current can be calculated. This is shown in Fig. 19 for different values of A_1 and A_2. Figure 20 (blue line) shows the most general case, where the dependence of A_1 and A_2 is absorbed in the axis scaling of the plot. The red line is the contribution of the propagating waves only.

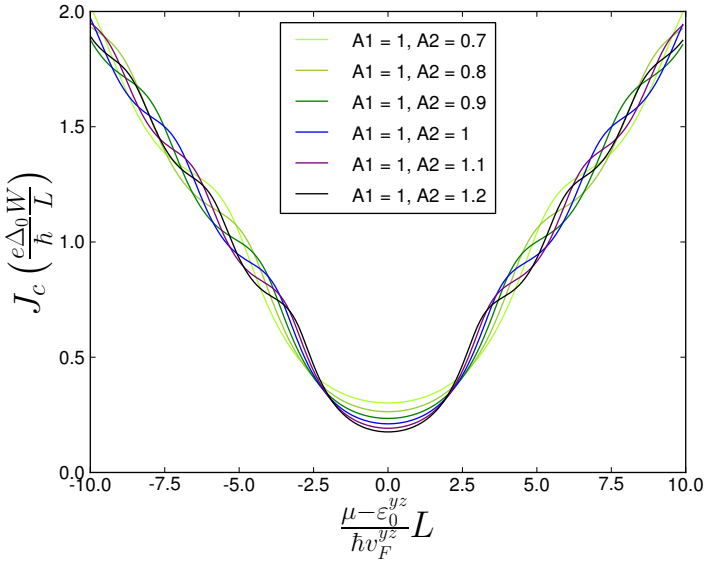

Figure 19: Critical current J_c of a Josephson junction for different values of A_1 and A_2, as a function of the chemical potential μ.

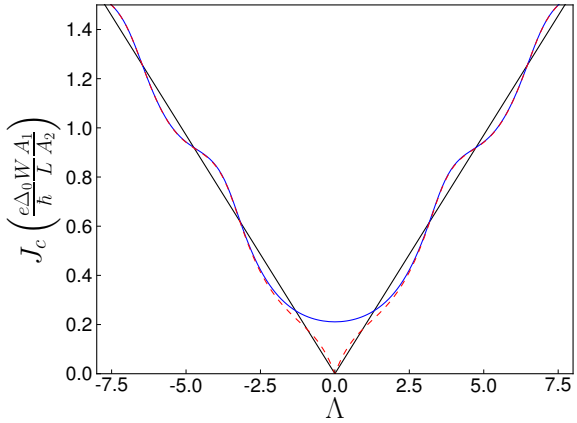

Figure 20: Critical current J_c of a Josephson junction, as a function of the chemical potential $\Lambda = \frac{\mu-\varepsilon_0^{yz}}{\hbar v_F^{yz}}\left(\frac{A_2 L}{A_1}\right)$ of the normal region (blue). This is the most general case, where the whole dependence on the factor $\frac{A_1}{A_2}$ is absorbed in the plotting variable and in the critical current J_c. In red, the contribution of the propagating waves only is shown. The black line is the slope of the critical current ($|\Lambda| \gg 1$).

The limiting behaviour at the Dirac point $\mu - \varepsilon_0^{yz} \ll \frac{\hbar v_F^{yz}}{L}$ can be calculated:

$$\begin{aligned} J(\phi) &= \frac{e\Delta_0}{2\hbar}\sum_{n=0}^{\infty}\frac{\tau_n \sin(\phi)}{\sqrt{1-\tau_n \sin^2(\phi/2)}} \\ &= \frac{e\Delta_0}{2\hbar}\sin(\phi)\sum_{n=0}^{\infty}\left(\tau_n + \frac{\tau_n^2\sin^2(\phi/2)}{2} + \frac{3\tau_n^3\sin^4(\phi/2)}{8} + \frac{5\tau_n^4\sin^6(\phi/2)}{16} + \dots\right). \end{aligned} \tag{207}$$

To get an analytical expression, $\sum_{n=0}^{\infty}\tau_n$ is calculated under the assumption $k_{zn} = i\kappa$, which means that $\tau_n = \frac{1}{\cosh^2(\kappa L)}$ and thus

$$\sum_{n=0}^{\infty}\tau_n = \frac{W}{L\pi}\frac{A_1}{A_2}\int_0^{\infty}\frac{d(\kappa L)}{\cosh^2(\kappa L)} = \frac{W}{L\pi}\frac{A_1}{A_2}. \tag{208}$$

Similarly the other sums can be computed:

$$\sum_{n=0}^{\infty}\frac{\tau_n^2}{2}=\frac{W}{L\pi}\frac{A_1}{A_2}\int_0^{\infty}d(\kappa L)\frac{1}{2\cosh^4(\kappa L)}=\frac{1}{3}\frac{W}{L\pi}\frac{A_1}{A_2}, \tag{209}$$

$$\sum_{n=0}^{\infty}\frac{3\tau_n^3}{8}=\frac{W}{L\pi}\frac{A_1}{A_2}\int_0^{\infty}d(\kappa L)\frac{3}{8\cosh^6(\kappa L)}=\frac{1}{5}\frac{W}{L\pi}\frac{A_1}{A_2}, \tag{210}$$

$$\sum_{n=0}^{\infty}\frac{5\tau_n^4}{16}=\frac{W}{L\pi}\frac{A_1}{A_2}\int_0^{\infty}d(\kappa L)\frac{5}{16\cosh^8(\kappa L)}=\frac{1}{7}\frac{W}{L\pi}\frac{A_1}{A_2}. \tag{211}$$

Using these approximations, the current becomes:

$$\begin{aligned}J(\phi)&=\frac{e\Delta_0}{\hbar}\frac{W}{L\pi}\frac{A_1}{A_2}\sum_{n=0}^{\infty}\cos(\phi/2)(\sin(\phi/2)+\frac{1}{3}\sin^3(\phi/2)+\frac{1}{5}\sin^5(\phi/2)\frac{1}{7}\sin^5(\phi/2)+\dots)\\&=\frac{e\Delta_0}{\hbar}\frac{W}{L\pi}\frac{A_1}{A_2}\cos(\phi/2)\mathrm{arctanh}(\sin(\phi/2)).\end{aligned} \tag{212}$$

This leads to the following critical current in the small $|\mu-\varepsilon_0^{yz}|$ regime:

$$J_{c,min}=0.21\frac{e\Delta_0}{\hbar}\frac{W}{L}\frac{A_1}{A_2}. \tag{213}$$

The Josephson current for these regime ($\Lambda=0$) is plotted in Fig. 18.

The slope (Fig. 20, black) of the numerically calculated critical current, corresponding to the opposite regime ($|\mu-\varepsilon_0^{yz}|\gg\hbar v_F^{yz}/L$), is:

$$J_{c,slope}=0.61\frac{e\Delta_0}{\hbar}\frac{W}{L\pi}\frac{A_1}{A_2}(\mu-\varepsilon_0^{yz}). \tag{214}$$

4.4 Edge junction

4.4.1 Solutions of the BdG equations

In region I ($x<0$, $z=0$) and in region II ($0<z<L$, $x=0$) of the edge junction we have the same solutions $\Psi_s^{I\pm}(x,y)$, $\Psi_e^{II\pm}(y,z)$ and $\Psi_h^{II\pm}(y,z)$ as for the step junction. Region III is described by $\mathbf{H^s_{yz}}$.

The solutions for $|k_y|\leq\left|\frac{\mu-\varepsilon_0^{yz}}{\hbar v_F^{yz}}\right|$ and $U_0+\mu-\varepsilon_0^{yz}\gg\{\Delta_0,\varepsilon\}$ and $\varepsilon<\Delta_0$ can be obtained by performing a rotation by $\pi/2$ about the $z-$axis and a rotation by $\pi/2$ about the $y-$axis in spin- and real-space. The transformation is described in Appendix B. The real-space transformation changes the $\{x,y,z\}$ dependent part, whereas the spin rotation changes the prefactor. The decay parameter κ has to be adapted and should be dependent on k_z. Eventually, we find the solutions of the BdG equations in region III:

$$\Psi_s^{III\pm}(y,z)=\begin{pmatrix}\Psi_s e^{III\pm}(y,z)\\ \Psi_s h^{III\pm}(y,z)\end{pmatrix}=e^{ik_y y\pm ik_z(z-L)-\kappa(z-L)}\begin{pmatrix}e^{\pm i\beta}\\ \pm i\frac{1+\cos(\alpha)}{\sin(\alpha)}e^{\pm i\beta}\\ e^{-i\phi}\\ \pm i\frac{1+\cos(\alpha)}{\sin(\alpha)}e^{-i\phi}\end{pmatrix}, \tag{215}$$

where $\beta=\arccos(\varepsilon/\Delta_0)$, $\sin(\alpha)=\frac{\hbar v_F^{yz}\frac{A_1}{A_2}k_z}{U_0+\mu-\varepsilon_0^{yz}}$, $\frac{A_1}{A_2}k_z=\sqrt{\left(\frac{U_0+\mu-\varepsilon_0^{yz}}{\hbar v_F^{yz}}\right)^2-k_y^2}$ and $\kappa=\frac{(U_0+\mu-\varepsilon_0^{yz})}{(\hbar v_F^{yz}\frac{A_1}{A_2})^2k_z}\Delta_0\sin(\beta)$.

The heavily doped regime (very large U_0) of region III can be approximated using:

$$\begin{aligned}\frac{1+\cos(\alpha)}{\sin(\alpha)} &= \frac{1 \pm \sqrt{1-\left(\frac{\hbar v_F^{yz}\frac{A_1}{A_2}k_z}{U_0+\mu-\varepsilon_0^{yz}}\right)^2}}{\frac{\hbar v_F^{yz}\frac{A_1}{A_2}k_z}{U_0+\mu-\varepsilon_0^{yz}}} \\ &= \frac{U_0+\mu-\varepsilon_0^{yz}}{\hbar v_F^{yz}\frac{A_1}{A_2}k_z} \pm \sqrt{\left(\frac{U_0+\mu-\varepsilon_0^{yz}}{\hbar v_F^{yz}\frac{A_1}{A_2}k_z}\right)^2-1} \\ &= \frac{U_0+\mu-\varepsilon_0^{yz}}{\sqrt{(U_0+\mu-\varepsilon_0^{yz})^2-(\hbar v_F^{yz})^2k_y^2}} \pm \sqrt{\left(\frac{U_0+\mu-\varepsilon_0^{yz}}{\sqrt{(U_0+\mu-\varepsilon_0^{yz})^2-(\hbar v_F^{yz})^2k_y^2}}\right)^2-1} \\ &\approx 1.\end{aligned} \tag{216}$$

Finally we obtain the wave functions in the heavily doped region III:

$$\Psi_s^{III\pm}(y,z) = e^{ik_y y \pm ik_z(z-L)-\kappa(z-L)}\begin{pmatrix} e^{\pm i\beta} \\ \pm ie^{\pm i\beta} \\ e^{-i\phi} \\ \pm ie^{-i\phi}\end{pmatrix}. \tag{217}$$

4.4.2 Boundary conditions

Again the Hamiltonians are TR invariant and the most general boundary condition for the first interface (between region I and II) is given by:

$$[a_{e,h}^+\Psi_{e,h}^{II+}(y,z)+a_{e,h}^-\Psi_{e,h}^{II-}(y,z)]|_{z\to 0^+} = i\sqrt{\frac{v_F^{xy}A_2}{v_F^{yz}A_1}}e^{-i\gamma_1\sigma_y}[\alpha^+\Psi_{s(e,h)}^{I+}(x,y)+\alpha^-\Psi_{s(e,h)}^{I-}(x,y)]|_{x\to 0^-}. \tag{218}$$

The indices e, h denote the electron and hole wave functions. In the superconducting wave function, e refers to the first two entries and h to the last two entries of the four component wave vectors. $a_{e,h}^{\pm}$ are the amplitudes of the electron and hole wave functions propagating in $\pm z-$direction in the normal region and $\alpha^{\pm}$ are the amplitudes of the wave functions in the superconducting region. For the interface between region II and III we get similar equations:

$$[\beta^+\Psi_{s(e,h)}^{III+}(x,y)+\beta^-\Psi_{s(e,h)}^{III-}(x,y)]|_{z\to L^+} = e^{-i\gamma_2\sigma_y}[a_{e,h}^+\Psi_{e,h}^{II+}(y,z)+a_{e,h}^-\Psi_{e,h}^{II-}(y,z)]|_{z\to L^-}. \tag{219}$$

In the edge junction the velocity changes only at the first interface. This is why only the boundary conditions for the first interface are dependent on the velocities.

4.4.3 Josephson current

We perform the same procedure as in the planar and step case and use the same "infinite mass" boundary conditions [28] as in the step case to quantize $k_{yn} = (n+1/2)\pi/W$. In the heavily doped regime and in the low energy limit some parameters can be simplified: $\alpha(-\varepsilon) \approx \alpha(\varepsilon) \approx \alpha(0) := \alpha$, and $k_z(-\varepsilon) \approx k_z(-\varepsilon) \approx k_z(0) := k_{zn}$. Finally, we get:

$$\varepsilon_n = \Delta_0\sqrt{(1-\tau_n\sin(\phi/2)^2)}, \tag{220}$$

$$\tau = -\frac{1}{\tan(\alpha)^2\sin(k_{zn}L)^2}. \tag{221}$$

Naturally, $\tau_n < 0$ corresponds to $\varepsilon_n > \Delta_0$ implying absence of Andreev bound states. The formation of Andreev bound states in the central region requires the presence of electrons with opposite spins in

regions I and III. Due to spin momentum locking in the topological insulator and because the spins in region I and III lie in different planes, the formation of Andreev bound states is prohibited. The only possibility is $k_y = 0$ implying spin along $y-$direction. This is not allowed due to the boundary conditions: $k_{yn} = (n + 1/2)\pi/W > 0$. Thus, the contribution of the Andreev bound states to the Josephson current vanishes in these edge junctions.

5 Josephson effect in ferromagnetic topological insulator junctions

So far, we have analyzed the Josephson effect on a topological insulator planar and step junction. Now we perform a similar examination of a junction with induced ferromagnetism. We aim to see the influences of the magnetization $\mathbf{M} = \mathbf{m} \cdot \sigma$ on the Josephson current. The analysis becomes a lot simpler, when we limit ourselves to a magnetization perpendicular to the junction. There the magnetization opens up a gap. Using the magnetization as a parameter, we can tune the critical current. To investigate how the magnetization in different directions affects the Josephson current, we will carry out an analysis of the Josephson current at the Dirac point.

We look at two systems (see Fig. 21), a planar junction in the $(x-y)$ plane and a step junction with superconducting electrodes in the $(x-y)$ plane and a weak link between them in the $(y-z)$ plane.

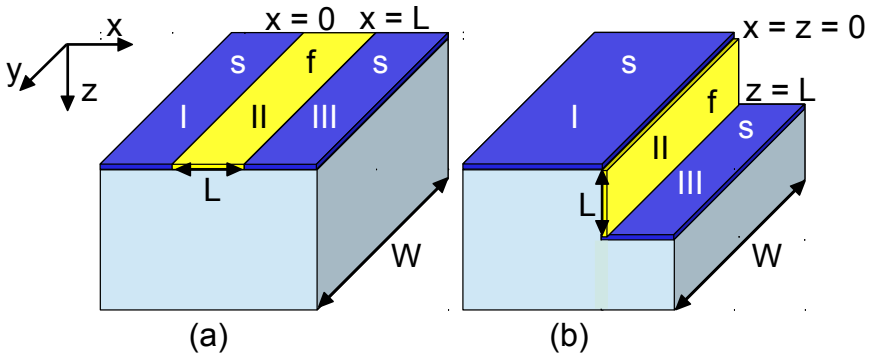

Figure 21: Schematics of the two ferromagnetic topological insulator junctions: (a) planar junction and (b) step junction. The blue planes are the superconductors inducing superconductivity in the surface states of the topological insulator (s). The left superconducting region is referred to as region I, the right as region III. The yellow plane is the ferromagnetic insulator inducing the magnetization $\mathbf{M}$ in the surface states of the topological insulator (f, region II).

5.1 Ferromagnetic planar junction

The junction to be investigated is shown in Fig. 21(a). Here, region II is covered by a ferromagnetic insulator, which leads to induced magnetization in the surface of the topological insulator. The simplest case is a magnetization perpendicular to the junction, thus $\mathbf{M} = m_z\sigma_z$. This is why we will first restrict ourselves to a junction with perpendicular magnetization only and afterwards we will extend our analysis by considering magnetizations in all directions for a chemical potential at the Dirac point energy.

5.1.1 General case

The ferromagnetic region is described by

$$\mathbf{H_{xy}^f} = \begin{pmatrix} H^{xy} - \mu + m_x\sigma_x + m_y\sigma_y + m_z\sigma_z & 0 \\ 0 & -H^{xy} + \mu + m_x\sigma_x + m_y\sigma_y + m_z\sigma_z \end{pmatrix}. \tag{222}$$

We can separate the BdG equation in two equations, one for holes and one for electrons. Then we can solve the simplified equation $H_{xy}^f(m_x, m_y, m_z)\Psi_e(x,y) = \varepsilon\Psi_e(x,y)$ for the first two components of the electron wave functions (the remaining two components are 0 due to the block diagonal form of the Hamiltonian), where:

$$H_{xy}^f(m_x, m_y, m_z) = \begin{pmatrix} \varepsilon_0^{xy} - \mu + m_z & -i\hbar v_F^{xy}(\partial_y + i\partial_x) + m_x - im_y \\ -i\hbar v_F^{xy}(\partial_y - i\partial_x) + m_x + im_y & \varepsilon_0^{xy} - \mu - m_z \end{pmatrix}. \tag{223}$$

For the hole wave functions the last two components (the first two are 0) can be obtained by solving: $H_{xy}^f(-m_x, -m_y, -m_z)\Psi_h(x,y) = -\varepsilon\Psi_h(x,y)$. Doing so, we find that the BdG equations are solved by

any linear combination of the basis states

$$\Psi_e^{II\pm}(x,y) = \begin{pmatrix} \frac{\mu-\varepsilon_0^{xy}+\varepsilon}{\hbar v_F^{xy}} + \frac{m_z}{\hbar v_F^{xy}} \\ k_y + \frac{m_x}{\hbar v_F^{xy}} \mp \kappa(\varepsilon, m_x, m_z) \\ 0 \\ 0 \end{pmatrix} e^{ik_y y + (i\frac{m_y}{\hbar v_F^{xy}} \pm \kappa(\varepsilon, m_x, m_z))x} \tag{224}$$

and

$$\Psi_h^{II\pm}(x,y) = \begin{pmatrix} 0 \\ 0 \\ \frac{\mu-\varepsilon_0^{xy}-\varepsilon}{\hbar v_F^{xy}} - \frac{m_z}{\hbar v_F^{xy}} \\ k_y(-\varepsilon) - \frac{m_x}{\hbar v_F^{xy}} \mp \kappa(-\varepsilon, -m_x, -m_z) \end{pmatrix} e^{ik_y y + (-i\frac{m_y}{\hbar v_F^{xy}} \pm \kappa(-\varepsilon, -m_x, -m_z))x} \tag{225}$$

with $\kappa(\varepsilon, m_x, m_z) = \sqrt{m_z^2 - (\mu - \varepsilon_0^{xy} + \varepsilon)^2 + (k_y \hbar v_F^{xy} + m_x)^2}/(\hbar v_F^{xy})$. The wave functions of the superconducting regions were calculated in the previous chapter.

The magnetization $\mathbf{M}$ breaks TR symmetry, thus we cannot use the general boundary conditions we used in the preceding sections. Instead, for simplicity, we demand continuity of the wave functions at the interfaces. We follow the same procedure as in the preceding chapters and write the boundary conditions in matrix form and search for nontrivial solutions. Consequently, we want the determinant of the matrix to be 0. We assume that the chemical potential satisfies $|\mu - \varepsilon_0^{xy}| \gg \varepsilon$ and we call this the low energy regime. It can be seen that we can apply this assumption by setting $\varepsilon = 0$ in the wave functions $\Psi_e^{II\pm}(x,y)$ and $\Psi_h^{II\pm}(x,y)$ of region II as ε is very small compared to $\mu - \varepsilon_0^{xy}$. This simplifies the problem, since only the wave functions of the superconducting regions remain energy dependent, whereas the wave functions of region II become independent of the excitation energy ε. Finally, we find solutions for ε. Unfortunately, this ends in very complicated solutions, thus, for further analysis, we distinguish between two special cases: perpendicular magnetization ($m_x = 0$ and $m_y = 0$) and chemical potential at the Dirac point energy ($\mu - \varepsilon_0^{xy} = 0$).

5.1.2 Perpendicular magnetization ($m_x = 0$ and $m_y = 0$)

In this case we see that in the low energy limit $\kappa(-\varepsilon, -m_x, -m_z) \approx \kappa(\varepsilon, m_x, m_z) \approx \kappa(0, 0, m_z) =: \kappa = \sqrt{m_z^2 - (\mu - \varepsilon_0^{xy})^2 + (k_y \hbar v_F^{xy})^2}/(\hbar v_F^{xy})$ such that we get a simple expression for the energy:

$$\varepsilon = \Delta_0 \sqrt{\frac{\kappa^2 + k_y^2 \sinh^2(\kappa L)}{\kappa^2 + (k_y^2 + m_z^2)\sinh^2(\kappa L)} - \frac{\kappa^2 \sin^2(\phi/2)}{\kappa^2 + (k_y^2 + m_z^2)\sinh^2(\kappa L)}} \tag{226}$$

A discussion of the results will be provided in the next section, where we perform the same analysis for a step junction. We can adopt the complete analysis from the step case by substituting $m_x \to m_z$ and setting $\frac{A_1}{A_2} = 1$.

Small magnetization: $m_z \leq \mu - \varepsilon_0^{xy}$:
For this case we assume, that we have only propagating states and no decaying states, thus instead of $\kappa(\varepsilon)$ we have $k_x(\varepsilon)$. The propagating wave functions which solve the BdG equation in the junction are:

$$\Psi_e^{II\pm}(x,y) = \begin{pmatrix} \sin(\alpha(\varepsilon)) \pm i\sqrt{\cos(\alpha(\varepsilon)^2) - p(m_z, \varepsilon)^2} \\ 1 - p(m_z, \varepsilon) \\ 0 \\ 0 \end{pmatrix} e^{ik_y y \pm ik_x(\varepsilon)x}, \tag{227}$$

$$\Psi_h^{II\pm}(x,y) = \begin{pmatrix} 0 \\ 0 \\ \sin(\alpha(-\varepsilon)) \pm i\sqrt{\cos(\alpha(-\varepsilon)^2) - p(-m_z, -\varepsilon)^2} \\ 1 - p(-m_z, -\varepsilon) \end{pmatrix} e^{ik_y y \pm ik_x(-\varepsilon)x}, \tag{228}$$

where $\sin(\alpha(\varepsilon)) = \frac{\hbar v_F^{xy} k_y}{\varepsilon+\mu-\varepsilon_0^{xy}}$, $k_x(\varepsilon) = \sqrt{\frac{(\varepsilon+\mu-\varepsilon_0^{xy})^2}{(\hbar v_F^{xy})^2} - \frac{m_z^2}{(\hbar v_F^{yz})^2} - k_y^2}$ and $p(m_z,\varepsilon) = \frac{m_z}{\varepsilon+\mu-\varepsilon_0^{xy}}$.

As the magnetization $m_z\sigma_z$ breaks the TR symmetry, we use continuity of the wave functions at the interfaces and demand nontrivial solutions for the coefficient vectors. As always, we have heavily doped superconducting regions and we analyze low energy solutions, $\alpha(-\varepsilon) \approx \alpha(\varepsilon) \approx \alpha(0) =: \alpha$, $p(m_z,-\varepsilon) \approx p(m_z,\varepsilon) \approx p(m_z,0) =: p(m_z)$, and $k_x(-\varepsilon) \approx k_x(\varepsilon) \approx k_x(0) =: k_x$. We get the following bound states:

$$\varepsilon = \Delta_0 \sqrt{\frac{1}{1+N} - \tau \sin^2(\phi/2)} \tag{229}$$

with

$$N = \frac{\frac{m_z^2}{(\hbar v_F^{xy})^2}\sin^2(k_x L)}{(k_x)^2\cos^2(k_x L) + \left(\left(\frac{\mu-\varepsilon_0^{xy}}{\hbar v_F^{xy}}\right)^2 - \frac{m_z^2}{(\hbar v_F^{xy})^2}\right)\sin^2(k_x L)} \tag{230}$$

and

$$\tau = \frac{(k_x)^2}{(k_x)^2\cos^2(k_x L) + \left(\frac{\mu-\varepsilon_0^{xy}}{\hbar v_F^{xy}}\right)^2 \sin^2(k_x L)}. \tag{231}$$

After performing the calculations we find that the detailed analysis and the calculation of the Josephson current can be adopted from the ferromagnetic step junction by replacing $\frac{A_1}{A_2} \to 1$, $k_z \to k_x$, $m_z \to m_x$, $\varepsilon_0^{yz} \to \varepsilon_0^{xy}$ and $v_F^{yz} \to v_F^{xy}$.

5.1.3 Chemical potential at the Dirac point ($\mu - \varepsilon_0^{xy} = 0$)

By considering only the case where the chemical potential is at the Dirac point energy, it is possible to get results for the magnetization pointing in any direction. If we assume $\sqrt{m_z^2+m_x^2} \gg \varepsilon$ we can employ $\kappa(\varepsilon,m_x,m_z) \approx \kappa(0,m_x,m_z) =: \kappa(m_x)$ and $\kappa(-\varepsilon,-m_x,-m_z) \approx \kappa(0,-m_x,-m_z) \approx \kappa(-m_x)$. Then the energy reads:

$$\frac{\varepsilon}{\Delta_0} = \sqrt{\frac{1}{2} + \frac{\cos(2L\frac{m_y}{\hbar v_F^{xy}} + \phi)\kappa(m_x)\kappa(-m_x) + \left(k_y^2 - \left(\frac{m_x}{\hbar v_F^{xy}}\right)^2 - \left(\frac{m_z}{\hbar v_F^{xy}}\right)^2\right)\sinh(\kappa(m_x)L)\sinh(\kappa(-m_x)L)}{2\kappa(m_x)\kappa(-m_x)\cosh(\kappa(m_x)L)\cosh(\kappa(-m_x)L)}}. \tag{232}$$

In this case we can inherit the solutions from the step case as well. We only have to replace $\kappa(m_z) \to \kappa(-m_x)$, $\kappa(-m_z) \to \kappa(m_x)$ and $-m_y\frac{A_2}{A_1} \to m_y$. The only difference in the analysis appears in the shift of the phase difference of the superconducting regions due to m_y in $\cos(2L\frac{m_y}{\hbar v_F^{xy}} + \phi)$. In the planar case the phase is shifted in the opposite direction and does not have the prefactor $\frac{A_2}{A_1}$.

5.2 Ferromagnetic step junction

The ferromagnetic step junction is illustrated in Fig. 21(b). Region I and III are covered by a superconductor and region II by a ferromagnet, leading to a superconducting or a ferromagnetic proximity effect respectively. Again we begin with the examination of a junction with perpendicular magnetization and later we will analyze the effects of the magnetization in all directions for the case of the chemical potential at the Dirac point energy.

5.2.1 General case

The Hamiltonian describing the ferromagnetic region II is:

$$\mathbf{H_{yz}^f} = \begin{pmatrix} H^{yz} - \mu + m_x\sigma_x + m_y\sigma_y + m_z\sigma_z & 0 \\ 0 & -H^{yz} + \mu + m_x\sigma_x + m_y\sigma_y + m_z\sigma_z \end{pmatrix} \tag{233}$$

As in the planar case we can separate the BdG equation in two equations, one for holes and one for electrons. Solving the simplified equation $H^f_{yz}(m_x, m_y, m_z)\Psi_e(y,z) = \varepsilon\Psi_e(y,z)$ gives us the first two components $\Psi_e(y,z)$ of the electron wave functions (the remaining two components are 0), where

$$H^f_{yz}(m_x, m_y, m_z) = \begin{pmatrix} \varepsilon_0^{yz} - \mu + i\hbar v_F^{yz}\partial_y + m_z & -\hbar v_F^{yz}\frac{A_1}{A_2}\partial_z + m_x - im_y \\ \hbar v_F^{yz}\frac{A_1}{A_2}\partial_z + m_x + im_y & \varepsilon_0^{yz} - \mu - i\hbar v_F^{yz}\partial_y - m_z \end{pmatrix}. \tag{234}$$

For the hole wave functions we find the last two components (the first two are 0) by solving $H^f_{yz}(-m_x, -m_y, -m_z)\Psi_h(y,z) = -\varepsilon\Psi_h(y,z)$ for the wave function. The BdG equations are then fulfilled by any linear combination of the wave functions:

$$\Psi_e^{II\pm}(y,z) = \begin{pmatrix} \frac{\mu-\varepsilon_0^{yz}+\varepsilon}{\hbar v_F^{yz}} - k_y + \frac{m_z}{\hbar v_F^{yz}} \\ \frac{m_x}{\hbar v_F^{yz}} \pm \kappa(\varepsilon, -m_x, -m_z) \\ 0 \\ 0 \end{pmatrix} e^{ik_y y + (-i\frac{m_y}{\hbar v_F^{xy}}\frac{A_2}{A_1} \pm \kappa(\varepsilon, m_x, m_z))z} \tag{235}$$

and

$$\Psi_h^{II\pm}(y,z) = \begin{pmatrix} 0 \\ 0 \\ \frac{\mu-\varepsilon_0^{yz}-\varepsilon}{\hbar v_F^{yz}} - k_y - \frac{m_z}{\hbar v_F^{yz}} \\ -\frac{m_x}{\hbar v_F^{yz}} \pm \kappa(-\varepsilon, m_x, m_z) \end{pmatrix} e^{ik_y y + (i\frac{m_y}{\hbar v_F^{xy}}\frac{A_2}{A_1} \pm \kappa(-\varepsilon, m_x, m_z))z}, \tag{236}$$

with $\kappa(\varepsilon, m_x, m_z) = \sqrt{m_x^2 - (\mu - \varepsilon_0^{yz} + \varepsilon)^2 + (k_y\hbar v_F^{xy} + m_z)^2}\frac{A_2}{\hbar v_F^{yz} A_1}$.
The wave functions for the superconducting regions are known from the previous chapter.

As the magnetization breaks TR symmetry we use continuity of the wave functions as boundary condition. We assume $|\mu - \varepsilon_0^{yz}| \gg \varepsilon$ (low energy regime) and follow the same procedure as in the planar case; we write the eight equations in matrix representation and demand nontrivial solutions for the coefficients of the wave functions. Again we restrict ourselves to the special cases of perpendicular magnetization and chemical potential at the Dirac point.

5.2.2 Perpendicular magnetization ($m_z = 0$ and $m_y = 0$)

In this case we see that in the low energy regime ($|\mu - \varepsilon_0^{yz}| \gg \varepsilon$) we can use $\kappa(-\varepsilon, -m_x, -m_z) \approx \kappa(\varepsilon, m_x, m_z) \approx \sqrt{m_x^2 - (\mu - \varepsilon_0^{yz})^2 + (k_y\hbar v_F^{yz})^2}\frac{A_2}{\hbar v_F^{yz} A_1} =: \kappa$ resulting in a handsome solution for the energy:

$$\varepsilon = \Delta_0\sqrt{\frac{\kappa^2 + k_y^2\sinh^2(\kappa L)}{\kappa^2 + (k_y^2 + m_x^2)\sinh^2(\kappa L)} - \frac{\kappa^2\sin^2(\phi/2)}{\kappa^2 + (k_y^2 + m_x^2)\sinh^2(\kappa L)}}. \tag{237}$$

Next we want to calculate the Josephson current. Therefore, we introduce a finite width W to quantize the transverse wave vectors of region II, $k_y \to k_{yn} = (n + 1/2)\pi/W$, $n = 0, 1, 2, \ldots$ ("infinite mass" boundary conditions [28]). With $\rho_n(\varepsilon, \phi)$, the density of states in mode n, the Josephson current at zero temperature is given by:

$$J(\phi) = -\frac{2e}{\hbar}\frac{d}{d\phi}\int_0^\infty d\varepsilon \sum_{n=0}^{\infty}\rho_n(\varepsilon, \phi)\varepsilon. \tag{238}$$

κ is quantized as well and $\kappa_n = \sqrt{m_x^2 - (\mu - \varepsilon_0^{yz})^2 + (k_{yn}\hbar v_F^{yz})^2}\frac{A_2}{\hbar v_F^{yz} A_1}$. The lowest $N(\mu - \varepsilon_0^{yz}) = \left(\frac{\sqrt{(\mu-\varepsilon_0^{yz})^2 - m_x^2}}{\hbar v_F^{yz}}\right)\frac{W}{\pi}$ modes are propagating as κ_n is imaginary while the higher modes are evanescent, since for these modes κ is real. The analysis of the Josephson current is done in the short-junction regime where the length L of the ferromagnetic region is small relative to the superconducting coherence length ξ. This requires $\Delta_0 \ll \hbar v_F^{yz}/L$. Finally, we have a single bound state per mode:

$$\varepsilon_n = \Delta_0\sqrt{\frac{\kappa_n^2 + k_y^2\sinh^2(\kappa_n L)}{\kappa_n^2 + (k_{yn}^2 + m_x^2)\sinh^2(\kappa_n L)} - \frac{\kappa_n^2\sin^2(\phi/2)}{\kappa_n^2 + (k_{yn}^2 + m_x^2)\sinh^2(\kappa_n L)}}. \tag{239}$$

By using $\rho_n(\varepsilon,\phi)=\delta(\varepsilon-\varepsilon_n(\phi))$ the supercurrent due to the discrete spectrum is

$$J(\phi)=\frac{e\Delta_0}{2\hbar}\sum_{n=0}^{\infty}\frac{\frac{\kappa_n^2}{\kappa_n^2+(k_{yn}^2+m_x^2)\sinh^2(\kappa_n L)}\sin(\phi)}{\varepsilon_n(\phi)}=\frac{e\Delta_0}{\hbar}\frac{W}{2\pi}\int_0^{\infty}\frac{\frac{\kappa_n^2}{\kappa_n^2+(k_{yn}^2+m_x^2)\sinh^2(\kappa_n L)}\sin(\phi)}{\varepsilon_n(\phi)}dk_{yn}. \quad (240)$$

As $L\ll W$, the summation over n may be replaced by an integration. The integral can be solved numerically. We calculate the critical Josephson current by maximizing the current with respect to the phase difference ϕ of the superconductors. This is done with Mathematica. Figure 22 shows the behaviour of the critical current for different values of $q_x=\frac{m_x}{\hbar v_F^{yz}}\frac{A_2L}{A_1}$. By plotting the solutions of the

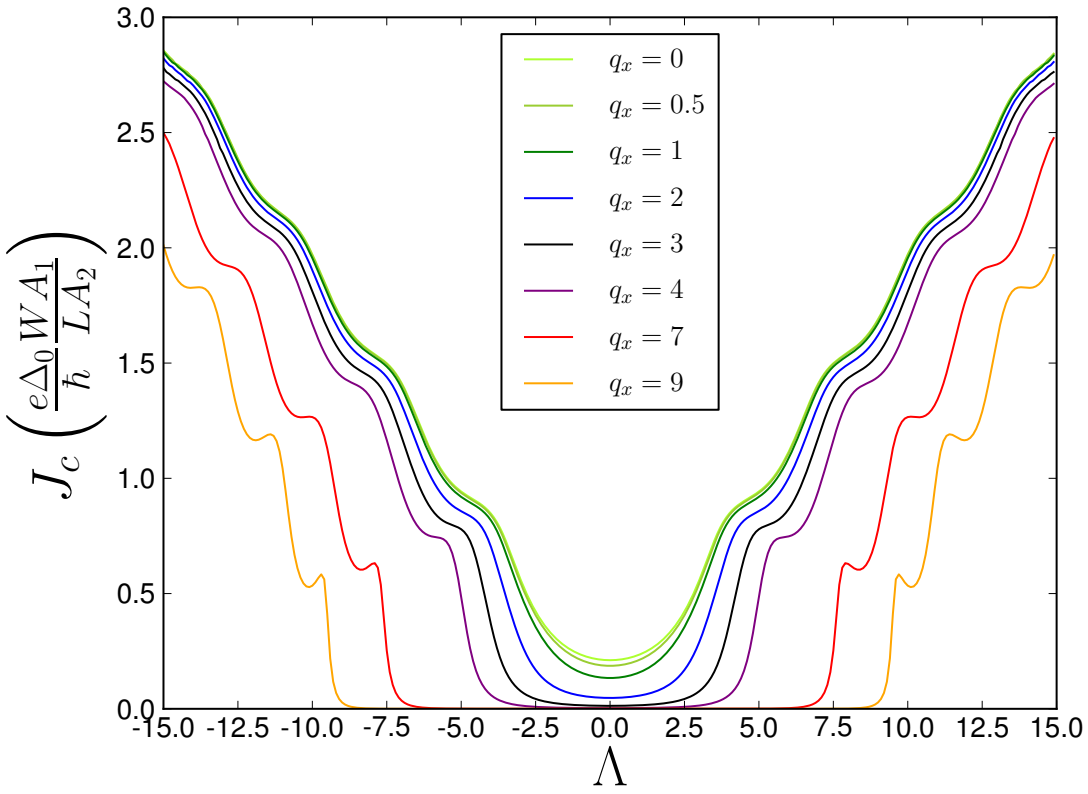

Figure 22: Critical Josephson current J_c of a ferromagnetic step junction as a function of $\Lambda=\frac{\mu-\varepsilon_0^{yz}}{\hbar v_F^{yz}}\left(\frac{A_2L}{A_1}\right)$ for different values of $q_x=\frac{m_x}{\hbar v_F^{yz}}\frac{A_2L}{A_1}$.

normal step junction and the solution here for $q_x=0$ in the same figure, we find that the $q_x=0$ plot restores the solutions of the normal step junction. Calculation shows that for $\Lambda=\frac{\mu-\varepsilon_0^{yz}}{\hbar v_F^{yz}}\left(\frac{A_2L}{A_1}\right)=0$ and $q_x=0$ we get the same critical current as in the step case:

$$J_c=0.21\frac{e\Delta_0}{\hbar}\frac{W}{L}\frac{A_1}{A_2}. \quad (241)$$

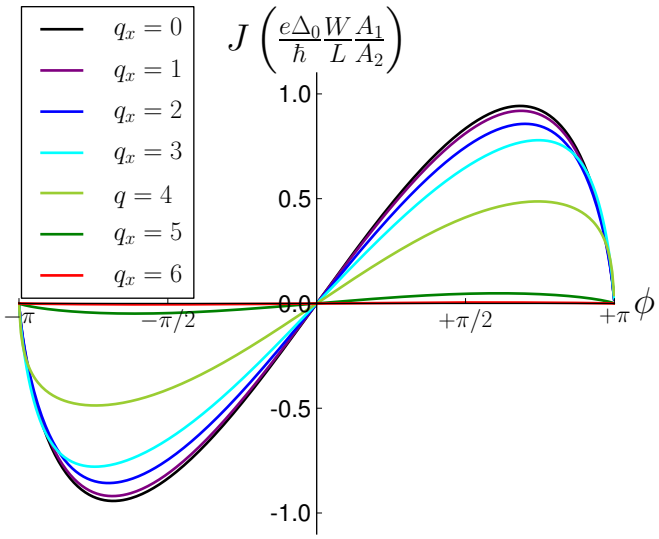

Figure 23: Josephson current for different values of $q_x = \frac{m_x}{\hbar v_F^{yz}} \frac{A_2 L}{A_1}$ while $\Lambda = \frac{\mu - \varepsilon_0^{yz}}{\hbar v_F^{yz}} \left(\frac{A_2 L}{A_1}\right) = 5$ is fixed.

The Josephson current gets suppressed by a perpendicular magnetization. This can be seen in Fig. 23, where the Josephson current for different magnetization strengths q_x is plotted while $\Lambda = 5$ is fixed. As the magnetization is increased, the current decreases. From Fig. 22 we know that the magnetization q_x can be used to tune the critical Josephson current. The stronger the magnetization, the larger the chemical potential needs to be, to result in a finite current. For large magnetization the finite Josephson current at the Dirac point ($\Lambda = 0$) vanishes. This can be seen in Fig. 24 which illustrates the dependence of J_c on q_x at $\Lambda = 0$. It corresponds to the points at $\Lambda = 0$ in Fig. 22.

At larger values of Λ we get a strange behaviour, as can be seen for $q_x = 7$ in Fig. 22. Certain values of J_c can be achieved by different values of Λ. In Fig. 25 the critical Josephson current is plotted as a function of Λ and q_x. We will analyze this non-monotonic behaviour of J_c in Appendix C in more detail.

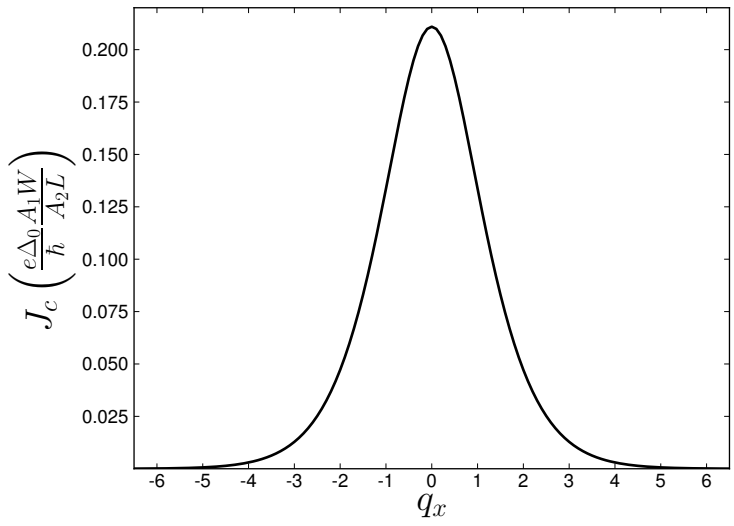

Figure 24: Critical Josephson current J_c of a ferromagnetic step junction as a function of $q_x = \frac{m_x}{\hbar v_F^{yz}} \frac{L A_2}{A_1}$.

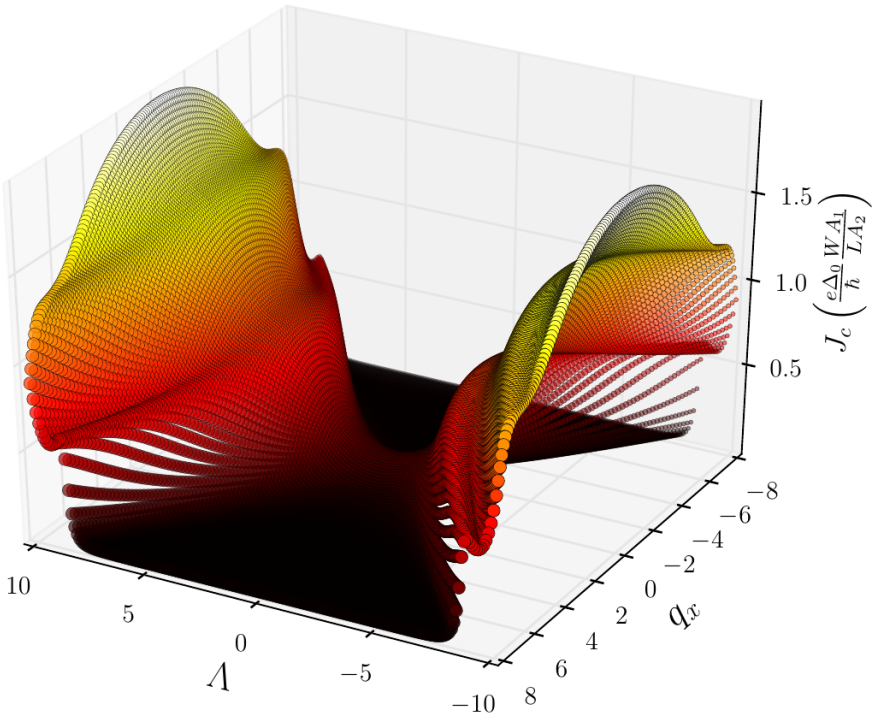

Figure 25: Critical Josephson current $J_c(\Lambda, q_x)$ of a ferromagnetic junction with $q_x = \frac{m_x}{\hbar v_F^{yz}}\frac{A_2 L}{A_1}$ and $\Lambda = \frac{\mu-\varepsilon_0^{yz}}{\hbar v_F^{yz}}\left(\frac{A_2 L}{A_1}\right)$. As soon as q_x is large enough, the same critical current can appear for different Λ.

Small magnetization: $m_x \leq \mu - \varepsilon_0^{yz}$ **($q_x \leq \Lambda$):**
In this limit only propagating waves contribute to the Josephson current. Consequently, instead of $\kappa(\varepsilon)$ we use $k_z(\varepsilon)$. The BdG equations are solved by the wave functions

$$\Psi_e^{II\pm}(y,z) = \begin{pmatrix} 1-\sin(\alpha(\varepsilon)) \\ p(m_x,\varepsilon) \pm i\sqrt{\cos(\alpha(\varepsilon)^2) - p(m_x,\varepsilon)^2} \\ 0 \\ 0 \end{pmatrix} e^{ik_y y \pm i k_z(\varepsilon) z}, \tag{242}$$

$$\Psi_h^{II\pm}(y,z) = \begin{pmatrix} 0 \\ 0 \\ 1-\sin(\alpha(-\varepsilon)) \\ p(-m_x,-\varepsilon) \pm i\sqrt{\cos(\alpha(-\varepsilon)^2) - p(-m_x,-\varepsilon)^2} \end{pmatrix} e^{ik_y y \pm i k_z(-\varepsilon) z}, \tag{243}$$

where $\sin(\alpha(\varepsilon)) = \frac{\hbar v_F^{yz} k_y}{\varepsilon+\mu-\varepsilon_0^{yz}}$, $\frac{A_1}{A_2}k_z(\varepsilon) = \sqrt{\frac{(\varepsilon+\mu-\varepsilon_0^{yz})^2}{(\hbar v_F^{yz})^2} - \frac{m_x^2}{(\hbar v_F^{yz})^2} - k_y^2}$ and $p(m_x,\varepsilon) = \frac{m_x}{\varepsilon+\mu-\varepsilon_0}$.

We can see, that magnetization $m_x\sigma_x$ breaks the TR symmetry. As a result the boundary conditions are given by the continuity of the wave functions. As before, we assume heavily doped superconducting regions. Furthermore, we consider only low energy solutions, enabling us to simplify some parameters: $\alpha(-\varepsilon) \approx \alpha(\varepsilon) \approx \alpha(0) =: \alpha$, $p(m_x,-\varepsilon) \approx p(m_x,\varepsilon) \approx p(m_x,0) =: p(m_x)$, and $k_z(-\varepsilon) \approx k_z(\varepsilon) \approx k_z(0) =: k_z$. Finally, demanding nontrivial solutions leads to

$$\varepsilon = \Delta_0\sqrt{\frac{1}{1+N} - \tau\sin^2(\phi/2)}, \tag{244}$$

with

$$N = \frac{\frac{m_x^2}{(\hbar v_F^{yz})^2}\sin^2(k_z L)}{\left(\frac{A_1}{A_2}k_z\right)^2\cos^2(k_z L) + \left(\left(\frac{\mu-\varepsilon_0^{yz}}{\hbar v_F^{yz}}\right)^2 - \frac{m_x^2}{(\hbar v_F^{yz})^2}\right)\sin^2(k_z L)} \tag{245}$$

and

$$\tau = \frac{\left(\frac{A_1}{A_2}k_z\right)^2}{\left(\frac{A_1}{A_2}k_z\right)^2 \cos^2(k_z L) + \left(\frac{\mu-\varepsilon_0^{yz}}{\hbar v_F^{yz}}\right)^2 \sin^2(k_z L)}. \tag{246}$$

With the "infinite mass" boundary conditions [28] at $y = 0$ and $y = W$, quantized $k_{yn} = (n+1/2)\pi/W$ can be used which quantizes k_{zn} as well. Then, $\frac{A_1}{A_2}k_{zn} = \sqrt{\frac{(\mu-\varepsilon_0^{yz})^2}{(\hbar v_F^{yz})^2} - \frac{m_x^2}{(\hbar v_F^{yz})^2} - k_{yn}^2}$, which means the lowest $N = \sqrt{\left(\frac{\mu-\varepsilon_0^{yz}}{\hbar v_F^{yz}}\right)^2 - \frac{m_x^2}{(\hbar v_F^{yz})^2}}\frac{W}{\pi}$ modes are propagating as k_{zn} is real, while the higher modes are evanescent, since for these modes k_{zn} is imaginary. The analysis of the Josephson current is done in the short-junction regime where the length L of the normal region is small relative to the superconducting coherence length ξ. The solution is a single bound state per mode where the index n denotes the nth mode:

$$\varepsilon(\phi) \to \varepsilon_n(\phi), \quad \tau \to \tau_n \quad \text{and} \quad N \to N_n. \tag{247}$$

Then the supercurrent due to the discrete spectrum becomes:

$$J(\phi) = \frac{e\Delta_0}{2\hbar}\sum_{n=0}^{\infty}\frac{\tau_n \sin(\phi)}{\sqrt{\frac{1}{1+N_n} - \tau_n \sin^2(\phi/2)}} = \frac{e\Delta_0}{\hbar}\frac{W}{2\pi}\int_0^{\sqrt{\left(\frac{\mu-\varepsilon_0^{yz}}{\hbar v_F^{yz}}\right)^2 - \frac{m_x^2}{(\hbar v_F^{yz})^2}}}\frac{\tau_n \sin(\phi)}{\sqrt{\frac{1}{1+N_n} - \tau_n \sin^2(\phi/2)}}dk_{yn}. \tag{248}$$

As $L \ll W$, the summation over n may be replaced by an integration. We only integrate over real k_{zn}.

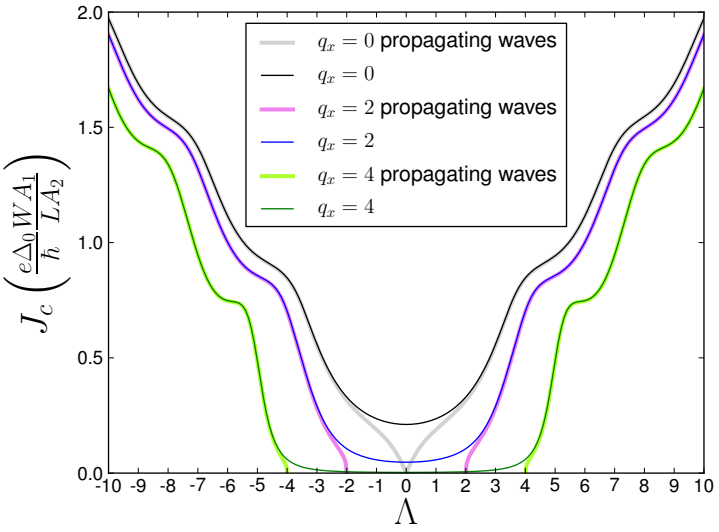

Figure 26: Critical current J_c of a ferromagnetic step junction as a function of Λ for three different values of $q_x = \frac{m_x}{\hbar v_F^{yz}}\frac{LA_2}{A_1}$. The contributions due to propagating waves only (labeled with "propagating waves") and the critical Josephson current (including the current due to decaying waves) are plotted.

As before we maximize the current with respect to ϕ and receive the critical current. Figure 26 shows the total critical current and the critical current due to propagating waves only for $q_x = 0$, $q_x = 2$ and $q_x = 4$. It can be seen that the critical Josephson current for $|\Lambda| < |q_x|$ arises due to decaying waves only. Both, propagating and decaying waves, contribute for chemical potentials with $|q_x| < |\Lambda| < |q_x| + \delta$, where $\delta > 0$ gives the range. As soon as $|\Lambda| > |q_x| + \delta$, the critical Josephson current arises singly due to propagating waves.

In the succeeding discussion, the use of κ refers to decaying waves in $z-$direction, whereas k_z refers to the propagating waves. They are related by $\kappa = -ik_z$.

5.2.3 Chemical potential at the Dirac point ($\mu - \varepsilon_0^{yz} = 0$)

With this simplification it is possible to examine an arbitrary direction of magnetization. If we assume $\sqrt{m_x^2 + m_z^2} \gg \varepsilon$ then $\kappa(\varepsilon, -m_x, -m_z) \approx \kappa(0, -m_x, -m_z) =: \kappa(-m_z)$ and $\kappa(-\varepsilon, m_x, m_z) \approx \kappa(0, m_x, m_z) =: \kappa(m_z)$. Again we calculate the energy:

$$\frac{\varepsilon}{\Delta_0} = \sqrt{\frac{1}{2} + \frac{\cos(2L\frac{m_y}{\hbar v_F^{yz}}\frac{A_2}{A_1} - \phi)\kappa(m_z)\kappa(-m_z) + \left(\frac{A_2}{A_1}\right)^2\left(k_y^2 - \left(\frac{m_x}{\hbar v_F^{yz}}\right)^2 - \left(\frac{m_z}{\hbar v_F^{yz}}\right)^2\right)\sinh(\kappa(m_z)L)\sinh(\kappa(-m_z)L)}{2\kappa(m_z)\kappa(-m_z)\cosh(\kappa(m_z)L)\cosh(\kappa(-m_z)L)}}. \tag{249}$$

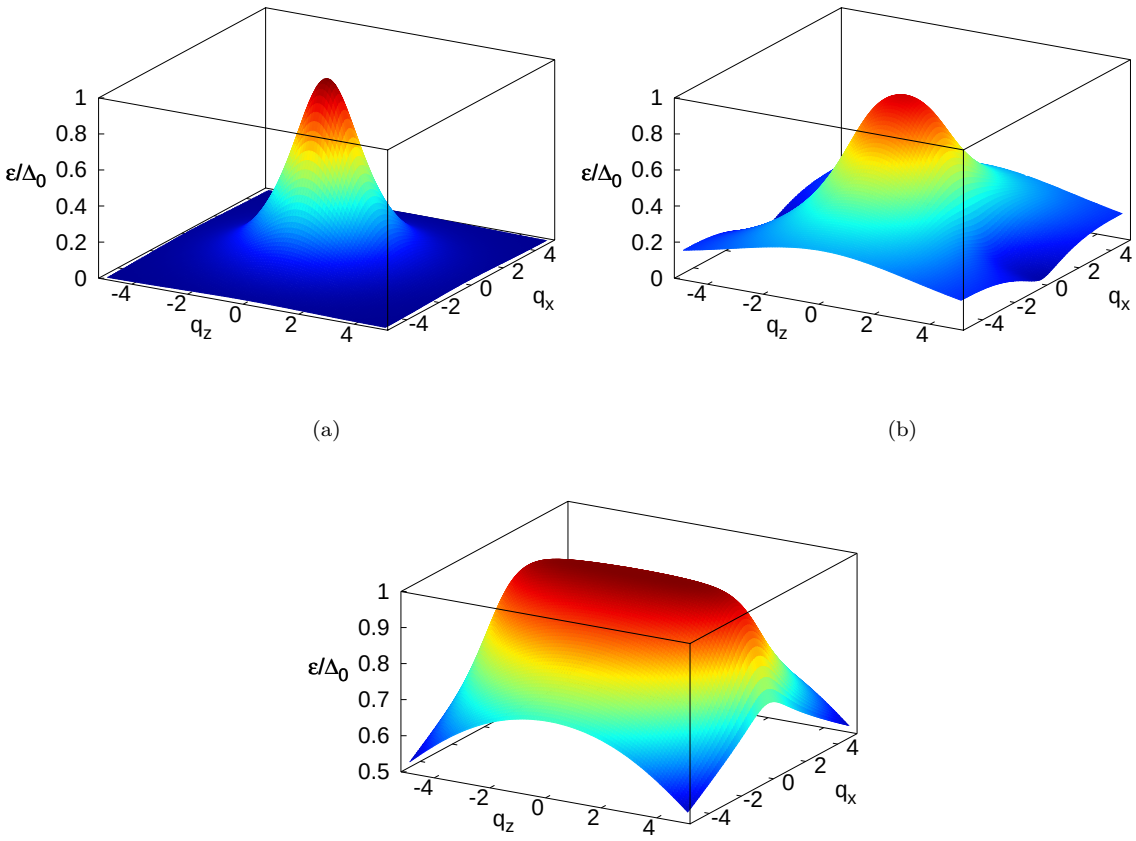

Figure 27: Energy dependence on $q_x = \frac{m_x}{\hbar v_F^{yz}}\frac{LA_2}{A_1}$ and $q_z = \frac{m_z}{\hbar v_F^{yz}}\frac{LA_2}{A_1}$ for $\phi = 0$ for different values of $q_y = \frac{m_y}{\hbar v_F^{yz}}\frac{LA_2}{A_1}$. (a) $q_y = 0$, (b) $q_y = 1.5$ and (c) $q_y = 5$.

We can plot the energy as a function of $q_x = \frac{m_x}{\hbar v_F^{yz}}\frac{LA_2}{A_1}$ and $q_z = \frac{m_z}{\hbar v_F^{yz}}\frac{LA_2}{A_1}$. Figure 27 shows such plots for 3 different values of $q_y = \frac{m_y}{\hbar v_F^{yz}}\frac{LA_2}{A_1}$ for the superconducting phase difference $\phi = 0$. The energy fulfills $\varepsilon \leq \Delta_0$. We can calculate the Josephson current as before by introducing the finite width W and thus

quantizing k_{yn}. The Josephson current then again is written in terms of a numerical integral:

$$J(\phi) = \frac{e\Delta_0}{\hbar}\frac{W}{L2\pi}\frac{A_1}{A_2}\int_0^\infty \frac{\sin\left(\phi - 2L\frac{m_y}{\hbar v_F^{yz}}\frac{A_2}{A_1}\right)}{\cosh(\kappa(m_z)L)\cosh(\kappa(-m_z)L)\frac{\varepsilon}{\Delta_0}} d\left(\frac{LA_2}{A_1}k_y\right). \tag{250}$$

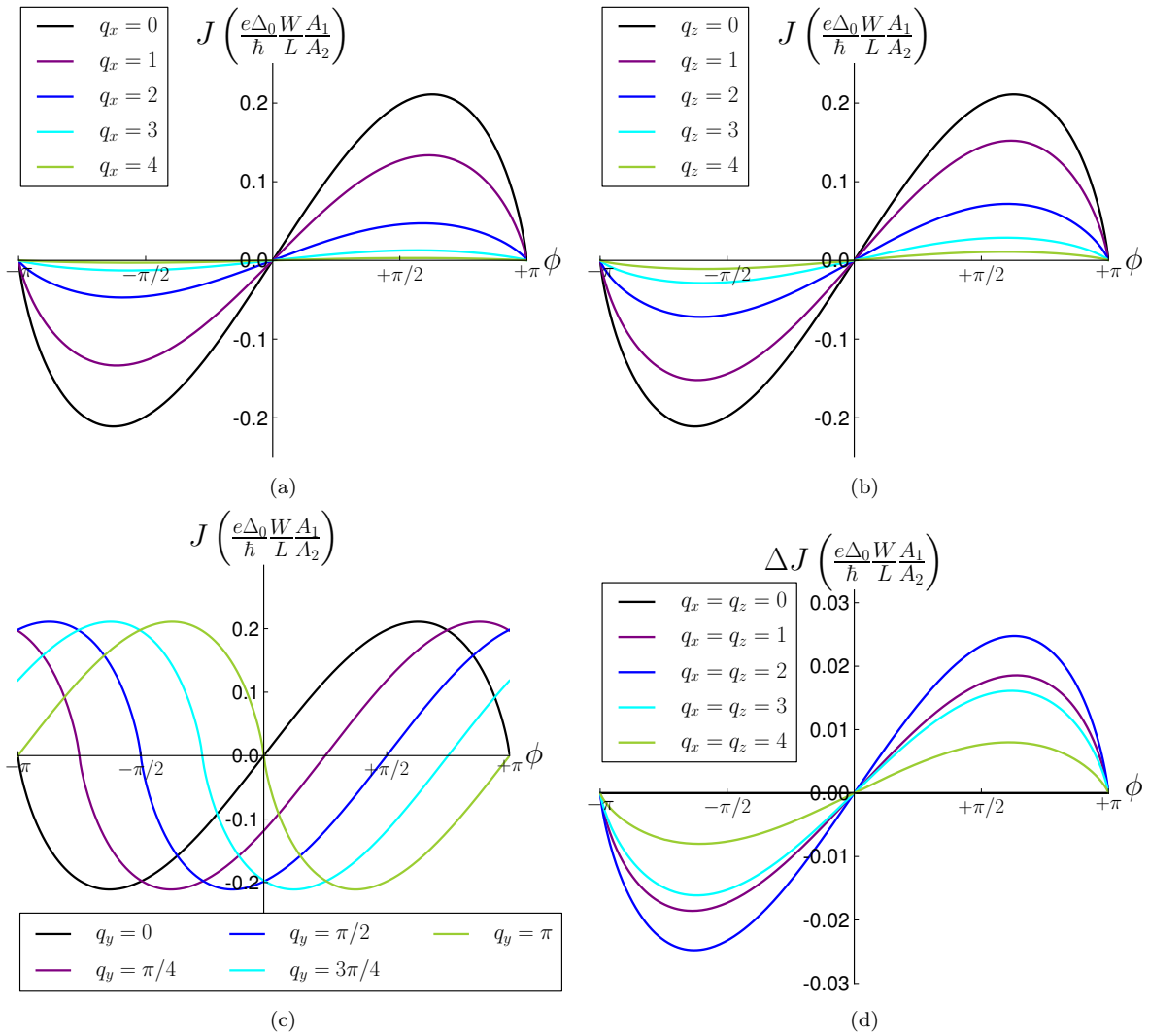

Figure 28: Josephson current as a function of ϕ for different magnetization $q_x = \frac{m_x}{\hbar v_F^{yz}}\frac{LA_2}{A_1}$, $q_y = \frac{m_y}{\hbar v_F^{yz}}\frac{LA_2}{A_1}$ and $q_z = \frac{m_z}{\hbar v_F^{yz}}\frac{LA_2}{A_1}$. (a) Josephson current for different values of q_x while $q_y = q_z = 0$. (b) Josephson current for different values of q_z while $q_x = q_y = 0$. (c) Josephson current for different values of q_y while $q_x = q_z = 0$. The black line in (a), (b) and (c) is $q_x = q_y = q_z = 0$. (d) shows the difference between the Josephson current of junctions with magnetization in $x-$ and $z-$direction ($\Delta J = J(q_z, \phi) - J(q_x, \phi)$).

We can see from the equation and in Fig. 28(c) that the magnetization $\frac{m_y}{\hbar v_F^{yz}}\frac{LA_2}{A_1}$ leads to a phase shift in the Josephson current and thus does not influence the critical current. Furthermore, we observe from Figs. 28(a), (b) and (d), that the magnetization in $x-$direction (perpendicular to the junction) suppresses the current stronger than the magnetization in $z-$direction (direction of transport). This can be understood, when we look at $\kappa(m_z)$ and $\kappa(-m_z)$, which are equal if m_z is 0 but they differ if $m_z \neq 0$. In principle, both, q_x and q_z, suppress the Josephson current.

Figure 29 shows the dependence of the critical Josephson current on $q_x = \frac{m_x}{\hbar v_F^{yz}}\frac{LA_2}{A_1}$ and $q_z = \frac{m_z}{\hbar v_F^{yz}}\frac{LA_2}{A_1}$

for $q_y = 0$. The black line corresponds to $q_z = 0$ and thus perpendicular magnetization. Moreover, it the same curve as in Fig. 24 at $\Lambda = 0$.

The maximal value of the critical current can again be calculated (numerically) and we can see that it restores again the result: $J_c = 0.21 \frac{e\Delta_0}{\hbar} \frac{W}{L} \frac{A_1}{A_2}$ for $q_x = q_y = q_z = \Lambda = 0$.

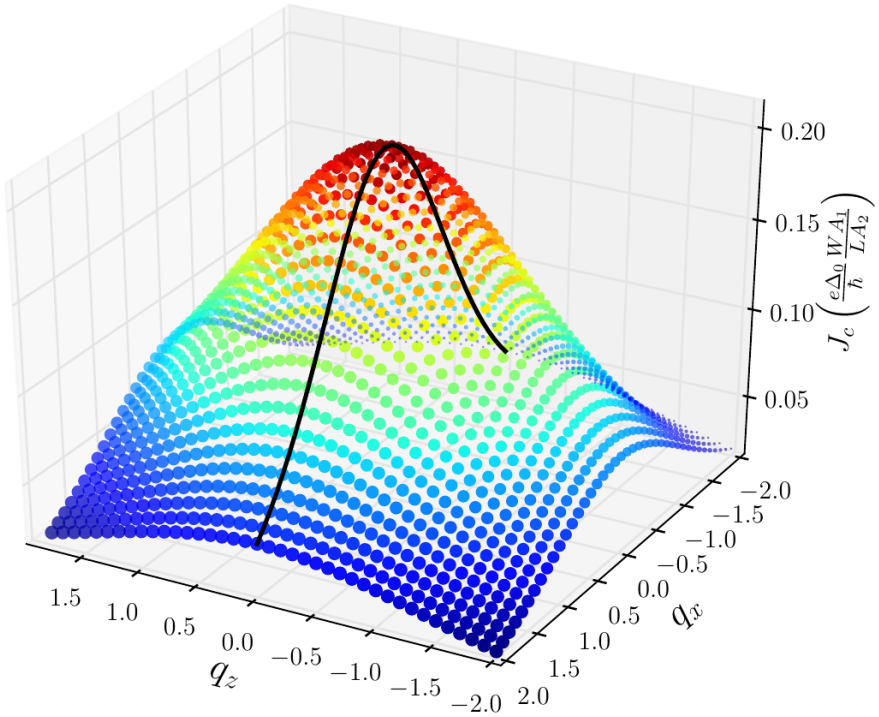

Figure 29: Critical Josephson current J_c of a ferromagnetic step junction as a function of $q_x = \frac{m_x}{\hbar v_F^{yz}} \frac{LA_2}{A_1}$ and $q_z = \frac{m_z}{\hbar v_F^{yz}} \frac{LA_2}{A_1}$ for $q_y = 0$. The black line corresponds to $q_z = 0$ (perpendicular magnetization).

5.3 Context of the results to current publications

Recently, the topics of induced superconductivity and ferromagnetism on topological insulators have attracted a great deal of attention. However, most of the calculations are done with Dirac-type surface Hamiltonians ($H = \hbar v_F(\sigma_x k_x + \sigma_y k_y)$) and include only the planar setup. In this section we would like to link our results to these works and discuss the similarities and differences. We focus on two subjects: the Josephson current of topological ferromagnetic junctions and the occurrence of Majorana fermions at the interface between the ferromagnetic and superconducting surfaces.

5.3.1 Josephson effect in ferromagnetic topological insulator junctions

In 2009 Y. Tanaka et al. [32] and in 2010 Linder et al. [18] studied the transport properties of planar topological ferromagnetic junctions. They calculated the Josephson current of this junction and found an anomalous current-phase relation, for a magnetization in $x-$direction (thus, in direction of transport). The magnetization m_x leads to a shift of the phase difference in the Josephson current, such that at $\phi = 0$ a finite Josephson current is possible for $m_x \neq 0$. This is similar to the behaviour we calculated for the magnetization m_y in $y-$ direction.
This different behaviour occurs due to the fact that Tanaka and Linder chose their topological insulator surface Hamiltonian to be a Dirac-type Hamiltonian $H = \hbar v_F(\sigma_x k_x + \sigma_y k_y)$. We, on the contrary, chose the model describing the topological insulator Bi_2Se_3, which is a Rashba type Hamiltonian of the form $H = \hbar v_F(\sigma_x k_y - \sigma_y k_x)$. This gives rise to a different spin-momentum locking on the surface and therefore the magnetization acts differently on the surface states of a Rashba-type Hamiltonian and a Dirac-type

Hamiltonian. Nevertheless, a comparison to the results of Tanaka and Linder shows, that our results are in agreement with their predictions. Furthermore, Tanaka and Linder showed that a perpendicular magnetization opens up a gap in the energy spectrum of a planar junction with a Dirac-type Hamiltonian, which is also what we calculated and analyzed for a step junction with a Rashba-type Hamiltonian.

5.3.2 Majorana fermions at the edge of the topological superconducting and ferromagnetic regions

The search for Majorana fermion realizations has intensified recently, as they enable topological quantum computation due to their non-Abelian statistics. Fu and Kane showed in 2007 [20] that the interface between a topological ferromagnetic region and a topological superconducting region hosts chiral Majorana edge states. In 2009 Tanaka et al. [32] found that the sign of the perpendicular magnetization m_z corresponds to the chirality of the Majorana mode. Since the Josephson junctions we calculated have two such interfaces, we investigated whether they can host Majorana fermions, which would lead to complete agreement with known results. We examine the interfaces for the topological ferromagnetic planar as well as the step junctions.

Ferromagnetic planar junction
At $\varepsilon = k_y = m_y = 0$ (which is only possible for phase difference $\phi = \pm\pi$ of the superconductors, here we choose $\phi = \pi$) the wave functions are decaying $\propto e^{\pm\frac{\Delta_0}{\hbar v_F^{xy}}x}$ in the superconducting region and $\propto e^{\pm\frac{\sqrt{m_x^2+m_z^2-(\mu-\varepsilon_0^{xy})^2}}{\hbar v_F^{xy}}x}$ in the ferromagnetic region. Note that for $k_y = 0$ and $\varepsilon = 0$ we have $\kappa(\varepsilon, m_x) = \kappa(-\varepsilon, -m_x) = \kappa(0, \pm m_x) =: \kappa$ (the sign of m_x does not matter as it occurs only squared in κ). If the length L of the junction is sufficiently large such that the decay length in the ferromagnetic region is smaller than L, $L \geq \frac{1}{\kappa} = \frac{\hbar v_F^{xy}}{\sqrt{m_x^2+m_z^2-(\mu-\varepsilon_0^{xy})^2}}$, we can assume that the first boundary of the ferromagnetic region supports states propagating in positive $x-$direction only and the second boundary supports states propagating in negative $x-$direction only. With these conditions we can calculate the spinors at the boundaries:

$$\Psi_1 = \begin{pmatrix} i(m_z+\mu-\varepsilon_0^{xy}) \\ i(m_x+\kappa) \\ -i(m_x+\kappa) \\ i(m_z+\mu-\varepsilon_0^{xy}) \end{pmatrix}, \qquad \Psi_2 = \begin{pmatrix} (i-1)(m_z+\mu-\varepsilon_0^{xy}) \\ (i-1)(m_x-\kappa) \\ (-i-1)(m_x-\kappa) \\ (i+1)(m_z+\mu-\varepsilon_0^{xy}) \end{pmatrix}. \tag{251}$$

These spinors satisfy $\mathcal{P}\Psi_1 = \Psi_1$ and $\mathcal{P}\Psi_2 = \Psi_2$, with the particle-hole conjugation operator $\mathcal{P} = (\tau_y \otimes \sigma_y K)$. These relations imply that we have Majorana bound states at the boundaries to the ferromagnet. With the spinors we can write the wave functions in the superconducting regions I and III:

$$\Psi_s^I(x,y) = \Psi_1 e^{\frac{\Delta_0}{\hbar v_F^{xy}}x} \quad \text{for region I and} \quad \Psi_s^{III}(x,y) = \Psi_2 e^{\frac{\Delta_0}{\hbar v_F^{xy}}(L-x)} \quad \text{for region III.} \tag{252}$$

In the ferromagnetic region ($0 < x < L$) the wave functions read:

$$\Psi_f^{II}(x,y) = \Psi_1 e^{-\frac{\sqrt{m_x^2+m_z^2-(\mu-\varepsilon_0^{xy})^2}}{\hbar v_F^{xy}}x} + \Psi_2 e^{\frac{\sqrt{m_x^2+m_z^2-(\mu-\varepsilon_0^{xy})^2}}{\hbar v_F^{xy}}(x-L)} \tag{253}$$

If the length of the Josephson junction becomes $L \leq \frac{1}{\kappa} = \frac{\hbar v_F^{xy}}{\sqrt{m_x^2+m_z^2-(\mu-\varepsilon_0^{xy})^2}}$, we don't have zero energy Majorana bound states anymore. Instead the overlap between the two boundaries gives rise to a finite splitting.

Ferromagnetic step junction
At $\varepsilon = m_y = 0$ and $k_y = 0$ (which is only true for phase difference $\phi = \pm\pi$ of the superconductors, here we choose $\phi = \pi$) the wave functions are decaying $\propto e^{\pm\frac{\Delta_0}{\hbar v_F^{xy}}x}$ in the superconducting region and $\propto e^{\pm\frac{\sqrt{m_x^2+m_z^2-(\mu-\varepsilon_0^{yz})^2}}{\hbar v_F^{yz}}z}$ in the ferromagnetic region. Note that for $k_y = 0$ and $\varepsilon = 0$ we have $\kappa(\varepsilon, m_z) = \kappa(-\varepsilon, -m_z) =: \kappa$. If the length L of the junction is sufficiently large such that the decay length in the ferromagnetic region is smaller than L, $L \geq \frac{1}{\kappa} = \frac{\hbar v_F^{yz}}{\sqrt{m_x^2+m_z^2-(\mu-\varepsilon_0^{yz})^2}}$, we can assume that the

first boundary in the ferromagnetic region supports states propagating in positive $z-$direction only and the second boundary supports states propagating in negative $z-$direction only. With these conditions we can calculate the spinors at the boundaries:

$$\Psi_1 = \begin{pmatrix} i(m_z + \mu - \varepsilon_0^{yz}) \\ i(m_x - \kappa) \\ -i(m_x - \kappa) \\ i(m_z + \mu - \varepsilon_0^{yz}) \end{pmatrix}, \qquad \Psi_2 = \begin{pmatrix} (i-1)(m_z + \mu - \varepsilon_0^{yz}) \\ (i-1)(m_x + \kappa) \\ (-i-1)(m_x + \kappa) \\ (i+1)(m_z + \mu - \varepsilon_0^{yz}) \end{pmatrix}. \tag{254}$$

They satisfy $\mathcal{P}\Psi_1 = \Psi_1$ and $\mathcal{P}\Psi_2 = \Psi_2$, with the particle-hole conjugation operator $\mathcal{P} = (\tau_y \otimes \sigma_y K)$, implying that we have Majorana bound states. With these spinors we can write the wave functions in the superconducting regions I and III:

$$\Psi_s^I(x,y) = \Psi_1 e^{\frac{\Delta_0}{\hbar v_F^{xy}} x} \quad \text{for region I} \quad \Psi_s^{III}(x,y) = \Psi_2 e^{-\frac{\Delta_0}{\hbar v_F^{xy}} x} \quad \text{for region III.} \tag{255}$$

In the ferromagnetic region ($0 < z < L$) we have:

$$\Psi_f^{II}(y,z) = \Psi_1 e^{-\frac{\sqrt{m_x^2 + m_z^2 - (\mu - \varepsilon_0^{yz})^2}}{\hbar v_F^{yz}} z} + \Psi_2 e^{\frac{\sqrt{m_x^2 + m_z^2 - (\mu - \varepsilon_0^{yz})^2}}{\hbar v_F^{yz}} (z-L)} \tag{256}$$

If the length L of the Josephson junction becomes $L \leq \frac{1}{\kappa} = \frac{\hbar v_F^{yz}}{\sqrt{m_x^2 + m_z^2 - (\mu - \varepsilon_0^{yz})^2}}$ we don't have zero energy Majorana bound states anymore. Instead the overlap between the two boundaries gives rise to a finite splitting.

It can be seen that the calculation of the Majorana bound states in step junctions is completely analogous to the planar junctions. Therefore an edge between a superconducting region and a ferromagnetic region perpendicular to the superconducting region can host Majorana edge states as well.

6 Conclusion and outlook

In this Master thesis we have conducted a detailed study of the Josephson effect on the surface of a topological insulator, e.g. Bi_2Se_3. Mainly we used two setups − the planar junction and the step junction. The symmetries of the bulk crystal structure give rise to different Fermi velocities in direction of the rotation symmetry axis and in direction perpendicular to it. We discovered that this manifests itself in a scaling factor in the critical Josephson current of the step junction when compared to the planar junction. This scaling appears in both normal and ferromagnetic topological insulator junctions. We performed a detailed discussion of the ferromagnetic topological insulator step junction revealing that a magnetization perpendicular to the junction suppresses the critical Josephson current. A magnetization in the transverse direction leads to a finite Josephson current, even when the phase difference of the superconductors is zero. Our findings are in agreement with the existing results about ferromagnetic topological Josephson junctions. We found a non-monotonic behaviour in the critical Josephson current when the perpendicular magnetization and the chemical potential are sufficiently large. An experimental verification of this behaviour (as shown in Fig. 22) could provide valuable insights into the transport mechanisms in these junctions.
Interestingly, the edge junction (see Fig. 16) gives rise to a vanishing contribution to the Josephson current from Andreev bound states. This suppression was explained in terms of spin momentum locking which prohibits the formation of Andreev bound states in the central region. From a finite contribution to the Josephson current for a planar junction, we enter a regime with vanishing contribution for a $\pi/2-$edge junction. Thus, the investigation of Andreev bound states for a general $\vartheta-$edge junction ($0 \leq \vartheta \leq \pi/2$) would be interesting from the point of view of this crossover. With this in mind we derived the surface Hamiltonian for a general angle about the $z-$axis. This would give the necessary equipment for an analysis of the Josephson effect at a general angle.

The same study can also be adapted to a spherical system. A description of a spherical topological insulator is found in Ref. [33]. They found that a nontrivial quantum spin connection emerges from the three-dimensional band structure. Their Hamiltonian can be used to calculate the Josephson effect on a spherical topological insulator with superconducting pole caps. Owing to spin orbit coupling, the electronic spin changes direction with latitude, implying that it lies in a horizontal plane at the poles, but in a vertical plane at the equator. This change of the spin orientation may have impact on the electronic response of various spintronics devices like spin valves. One may also include ferromagnetic components, which may lead to interesting behaviour as well.

Apart from investigating different geometries, the presence of an external magnetic field applied on the junction promises interesting effects. In Ref. [34] they discuss exact analytical solutions for the bound states of Dirac electrons in graphene in various magnetic fields with translational symmetry. The authors use a factorization method in the framework of the Dirac-Weyl equation for a massless electron in a magnetic field and other techniques of supersymmetric quantum mechanics. The solutions and the ideas may be adapted to topological insulators and may enable the calculation of the Josephson effect in junctions with different magnetic fields.

Last but not least, systems studied in this Master thesis could be investigated with a bias voltage applied over the junction. This leads to an AC Josephson effect. It has been shown that the conductance in a topological insulator step junction is suppressed when the bias current is increased [35]. Furthermore, one may use ferromagnetic topological insulator junctions which may also lead to interesting interactions between the bias voltage and the ferromagnetism.

7 Acknowledgements

My thanks go to Prof. Dr. Christoph Bruder for regularly discussing the progress and for offering the equipment. Special gratitudes I give to Dr. Rakesh Tiwari and to Dr. Thomas Schmidt, who supervised the project and provided very good advice and support.

Appendices

A TR and particle-hole symmetry

A.1 TR symmetry for spin-1/2 particles

In this section we want to investigate how TR acts on spin-1/2 particles and what the TR operator $\mathcal{T}$ looks like. The spin is described with the Pauli matrices σ_i, $i = x, y, z$. As the TR operator flips the sign of a spin, we know: $\mathcal{T}\sigma_i\mathcal{T}^{-1} = -\sigma_i$. This can be satisfied with $\mathcal{T} = i\sigma_y K$ where K is the complex conjugation. We can see that $\mathcal{T}^2 = i\sigma_y K i\sigma_y K = i\sigma_y i\sigma_y = -\sigma_y^2 = -\mathbb{I}_{2\times 2}$. $i\sigma_y$ is a unitary matrix and thus $\mathcal{T}^{-1} = \mathcal{T}^\dagger$ which means that $\mathcal{T}$ is an anti unitary operator.
To see that it is a good TR operator for our properties, we apply it on position $\mathbf{r}$ and on momentum $\hbar\mathbf{k}$ (replace k_i by $-i\partial_i$) we can see that:

$$\begin{aligned}
&\mathcal{T}(r_i \cdot \mathbb{I}_{2\times 2})\mathcal{T}^{-1} = r_i \cdot \mathbb{I}_{2\times 2} && \text{the position is invariant under TR}\\
&\mathcal{T}(-i\hbar\partial_i \cdot \mathbb{I}_{2\times 2})\mathcal{T}^{-1} = i\hbar\partial_i && \text{the momentum } \mathbf{k} \text{ changes sign}\\
&\mathcal{T}\sigma_i\mathcal{T}^{-1} = -\sigma_i && \text{the spin changes sign}\\
&\mathcal{T}(U \cdot \mathbb{I}_{2\times 2})\mathcal{T}^{-1} = U \cdot \mathbb{I}_{2\times 2} && \text{constants do not change sign}
\end{aligned} \tag{257}$$

This is true when we consider only one spin-1/2 particle at once. As we work in a Nambu basis where one basis vectors describes an electron and a hole at the same time, the complete TR operator is $\mathcal{T} = \mathbb{I}_{2\times 2} \otimes i\sigma_y K$.

A.2 Particle-hole symmetry

The particle-hole symmetry is the symmetry which relates the electrons and holes in the system to each other. In our Nambu basis we can express the particle-hole symmetry though the operator

$$\mathcal{P} = \tau_y \otimes \sigma_y K = \begin{pmatrix} 0 & 0 & 0 & -1 \\ 0 & 0 & 1 & 0 \\ 0 & 1 & 0 & 0 \\ -1 & 0 & 0 & 0 \end{pmatrix}. \tag{258}$$

K is the complex conjugation and τ_y and σ_y are the second Pauli matrices in real and spin space respectively. This operator fulfills

$$\mathcal{P}\mathbf{H}(\mathbf{r})\mathcal{P}^\dagger = -\mathbf{H}(\mathbf{r}). \tag{259}$$

As $\mathcal{P}^2 = 1$, $\mathcal{P}$ is an unitary operator. If there is a solution ψ_i with positive energy E_i there must exist a solution ψ_j with negative energy $E_j = -E_i$ and the solutions satisfy $\psi_j(\mathbf{r}) = \mathcal{P}\psi_i(\mathbf{r})$. We can diagonalize $\mathbf{H}$: $\mathbf{H_{diag}} = \frac{1}{2}\sum_i E_i \Psi_i^\dagger \Psi_i$. The solutions now satisfy $\Psi_j = \Psi_i^\dagger$. If $E = 0$ it is possible to get a solution that satisfies $\Psi = \Psi^\dagger$ and is thus a Majorana fermion. In our Nambu basis this means, a general Majorana fermion has to satisfy the equation

$$\psi_M(\mathbf{r}) = \mathcal{P}\psi_M(\mathbf{r}). \tag{260}$$

This allows us to write the state in a general form:

$$\psi_M(\mathbf{r}) = \begin{pmatrix} f(\mathbf{r}) \\ g(\mathbf{r}) \\ g^*(\mathbf{r}) \\ -f^*(\mathbf{r}) \end{pmatrix}. \tag{261}$$

Our topological insulator Hamiltonians are TR invariant: $\mathcal{T}\mathbf{H}\mathcal{T} = \mathbf{H}$ where $\mathcal{T} = \mathbb{I}_{2\times 2} \otimes i\sigma_y K$ is the TR operator. If $\psi_i(\mathbf{r})$ is an eigenstate, also $\mathcal{T}\psi_i(\mathbf{r})$ has to be an eigenstate with the same energy. This

is Kramers' theorem for a superconductor. For the Majorana spinor above the Kramers' partner takes the form:

$$\psi'_M(\mathbf{r}) = \begin{pmatrix} g^*(\mathbf{r}) \\ -f^*(\mathbf{r}) \\ -f(\mathbf{r}) \\ -g(\mathbf{r}) \end{pmatrix}. \tag{262}$$

The probability densities of the Majorana fermion and its Kramers' partner are equal: $|\psi_M(\mathbf{r})|^2 = |\psi'_M(\mathbf{r})|^2 = 2|g(\mathbf{r})|^2 + 2|f(\mathbf{r})|^2$. To get spatially isolated Majorana fermions, which means Majorana fermions which don't have a Kramers' partner with identical probability density, we need a Hamiltonian which breaks TR symmetry.

B Spin- and real-space rotation

As we need to solve complicated equations for the different faces of the topological insulator, it may be useful to know, how one can derive the solution of a face when knowing the solution of another face. We derive this for the example of the two faces of the 3D topological insulator that are described with Hamiltonians of the form:

$$H^{xy} = \sigma_x k_y - \sigma_y k_x \tag{263}$$

and

$$H^{yz} = \sigma_y k_z - \sigma_z k_y. \tag{264}$$

We want to transform H^{xy} to H^{yz}. For that, a spin-space rotation and a real-space rotation are needed. At first a rotation by $\pi/2$ about the $z-$axis and a rotation by $\pi/2$ about the $y-$axis in spin-space are done by the transformation

$$S = e^{-i\pi/4\sigma_y} e^{-i\pi/4\sigma_z}. \tag{265}$$

This fulfills

$$S \begin{pmatrix} \sigma_x \\ \sigma_y \\ \sigma_z \end{pmatrix} S^{-1} = \begin{pmatrix} \sigma_y \\ \sigma_z \\ \sigma_x \end{pmatrix}. \tag{266}$$

The same rotation in real space reads

$$R(\mathbf{n}, \phi) = e^{-i\phi \mathbf{nL}}. \tag{267}$$

$\mathbf{n}$ is the unit vector about which the system is rotated, $\phi = (\phi_x, \phi_y, \phi_z)$ is the rotation angle and $\mathbf{L} = \mathbf{r} \times \mathbf{k}$ is the angular momentum operator. As before, a rotation by $\pi/2$ about the $z-$axis and a rotation by $\pi/2$ about the $y-$axis shall be done. First the rotation by $\pi/2$ about the $z-$axis a calculated:

$$\begin{aligned} R(\mathbf{e_z}, \pi/2) \begin{pmatrix} k_x \\ k_y \end{pmatrix} R(\mathbf{e_z}, \pi/2)^\dagger &= \begin{pmatrix} k_x \\ k_y \end{pmatrix} + \left(\frac{-i\pi}{2} \right) \left[xk_y - yk_x, \begin{pmatrix} k_x \\ k_y \end{pmatrix} \right] + \dots \\ &= \begin{pmatrix} k_x \\ k_y \end{pmatrix} + \left(\frac{i\pi}{2} \right) \begin{pmatrix} -ik_y \\ ik_x \end{pmatrix} + \frac{1}{2} \left(\frac{-i\pi}{2} \right)^2 \left[xk_y - yk_x, \begin{pmatrix} ik_y \\ -ik_x \end{pmatrix} \right] + \dots \\ &= \begin{pmatrix} k_x \\ k_y \end{pmatrix} + \left(\frac{\pi}{2} \right) \begin{pmatrix} k_y \\ -k_x \end{pmatrix} - \frac{1}{2} \left(\frac{\pi}{2} \right)^2 \begin{pmatrix} k_x \\ k_y \end{pmatrix} + \dots \\ &= \begin{pmatrix} k_x \cos(\pi/2) + k_y \sin(\pi/2) \\ k_y \cos(\pi/2) - k_x \sin(\pi/2) \end{pmatrix} \\ &= \begin{pmatrix} k_y \\ -k_x \end{pmatrix}. \end{aligned} \tag{268}$$

Analogously one can obtain

$$R(\mathbf{e_y}, \pi/2) \begin{pmatrix} k_z \\ k_x \end{pmatrix} R(\mathbf{e_y}, \pi/2)^\dagger = \begin{pmatrix} k_x \\ -k_z \end{pmatrix}. \tag{269}$$

Finally, we get the complete rotation in real-space

$$R(\mathbf{e_y}, \pi/2) R(\mathbf{e_z}, \pi/2) \begin{pmatrix} k_x \\ k_y \\ k_z \end{pmatrix} R(\mathbf{e_z}, \pi/2)^\dagger R(\mathbf{e_y}, \pi/2)^\dagger = \begin{pmatrix} k_y \\ k_z \\ k_x \end{pmatrix}. \tag{270}$$

Therefore (spin- and real-space transformations commute) the unitary transformation is described by the operator

$$U = SR(\mathbf{e_y}, \pi/2) R(\mathbf{e_z}, \pi/2), \tag{271}$$

which acts on the Hamiltonian as follows:

$$U H^{xy} U^\dagger = H^{yz}. \tag{272}$$

To perform the rotation on the wave functions, the matrix representation of the rotations is chosen:

$$R_x(\phi_x) = \begin{pmatrix} 1 & 0 & 0 \\ 0 & \cos(\phi_x) & -\sin(\phi_x) \\ 0 & \sin(\phi_x) & \cos(\phi_x) \end{pmatrix}, \tag{273}$$

$$R_y(\phi_y) = \begin{pmatrix} \cos(\phi_y) & 0 & \sin(\phi_y) \\ 0 & 1 & 0 \\ -\sin(\phi_y) & 0 & \cos(\phi_y) \end{pmatrix}, \tag{274}$$

$$R_z(\phi_z) = \begin{pmatrix} \cos(\phi_z) & -\sin(\phi_z) & 0 \\ \sin(\phi_z) & \cos(\phi_z) & 0 \\ 0 & 0 & 1 \end{pmatrix}. \tag{275}$$

The rotation transforms a vector $(x, y, z)^\intercal$ in the following way:

$$SR_y(\pi/2)R_z(\pi/2) \begin{pmatrix} x \\ y \\ z \end{pmatrix} = S \begin{pmatrix} z \\ x \\ y \end{pmatrix}. \tag{276}$$

This can be applied on the wave functions.

C Non-monotonic critical Josephson current at $\Lambda > q_x$

In this section we want to discuss the non-monotonic critical Josephson current appearing for certain values of q_x and Λ in step junctions with perpendicular magnetization. Our investigation leads to ideas of how this behaviour is connected to ferromagnetism.

In Figs. 22 and 25 we can see that, as soon as the magnetization q_x becomes large enough, there are points of critical current J_c which can belong to two or three different chemical potentials. Further analysis shows, that this is not the case for $q_x \leq 4.51$ but is the case for $q_x \geq 4.55$. The critical value for 0 slope is in between. As the calculation for the critical current involves solving a numerical integral and a maximization with respect to ϕ it is very hard to find the reason for this behaviour. To get a better picture we look at the $q_x = 7$ curve. We choose six points (belonging to two values of the critical current J_c) which we want to analyze. They are listed in Tab. 1. The first point is located before the local maximum, the second point is around the inflection point and the third point is after the local minimum.

J_c	$\Lambda = \frac{\mu - \varepsilon_0^{yz}}{\hbar v_F^{yz}} \left(\frac{A_2 L}{A_1}\right)$	$\phi(J_c)$
0.61	7.8	2.51
	8.17	2.29
	8.52	2.17
1.27	10.1	2.33
	10.2	2.28
	10.5	2.22

Table 1: Two values of critical current J_c which can be achieved by three different Λ and three points corresponding to this J_c are listed. The magnetization is chosen to be $q_x = \frac{m_x}{\hbar v_F^{yz}} \frac{A_2 L}{A_1} = 7$. $\phi(J_c)$ is the phase difference where the Josephson current achieves its maximal value J_c.

For further analysis we look at the energy spectrum for the first three points listed in Table 1. We examine the energy within the regime where we have propagating waves, thus $0 \leq k_y \leq \sqrt{\left(\frac{\mu - \varepsilon_0^{yz}}{\hbar v_F^{yz}}\right)^2 - \frac{m_x^2}{(\hbar v_F^{yz})^2}}$, with respect to $k_z L$ and ϕ. This is illustrated in Fig. 30. Figure 31 shows the energy with respect to $k_y \frac{A_2 L}{A_1}$ and ϕ. We can see that there are certain points with zero energy.

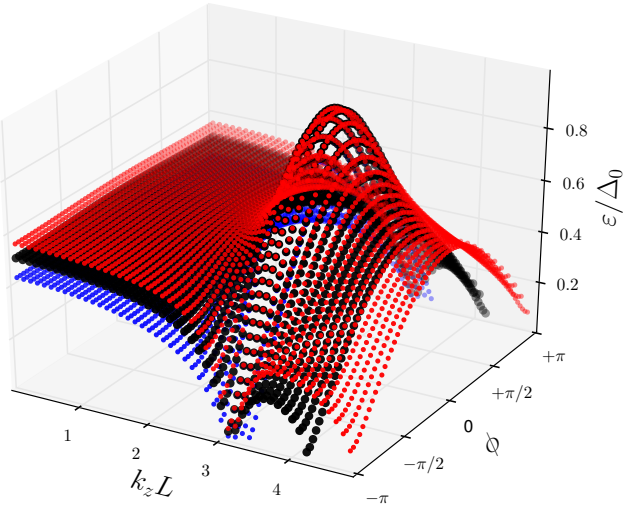

Figure 30: Energy dependence on the superconducting phase difference ϕ and on $k_z L$ for different $\Lambda = \frac{\mu - \varepsilon_0^{yz}}{\hbar v_F^{yz}} \left(\frac{A_2 L}{A_1} \right)$. The magnetization is chosen to be $q_x = \frac{m_x}{\hbar v_F^{yz}} \frac{A_2 L}{A_1} = 7$. Blue: $\Lambda = 7.8$, black: $\Lambda = 8.17$ and red: $\Lambda = 8.52$.

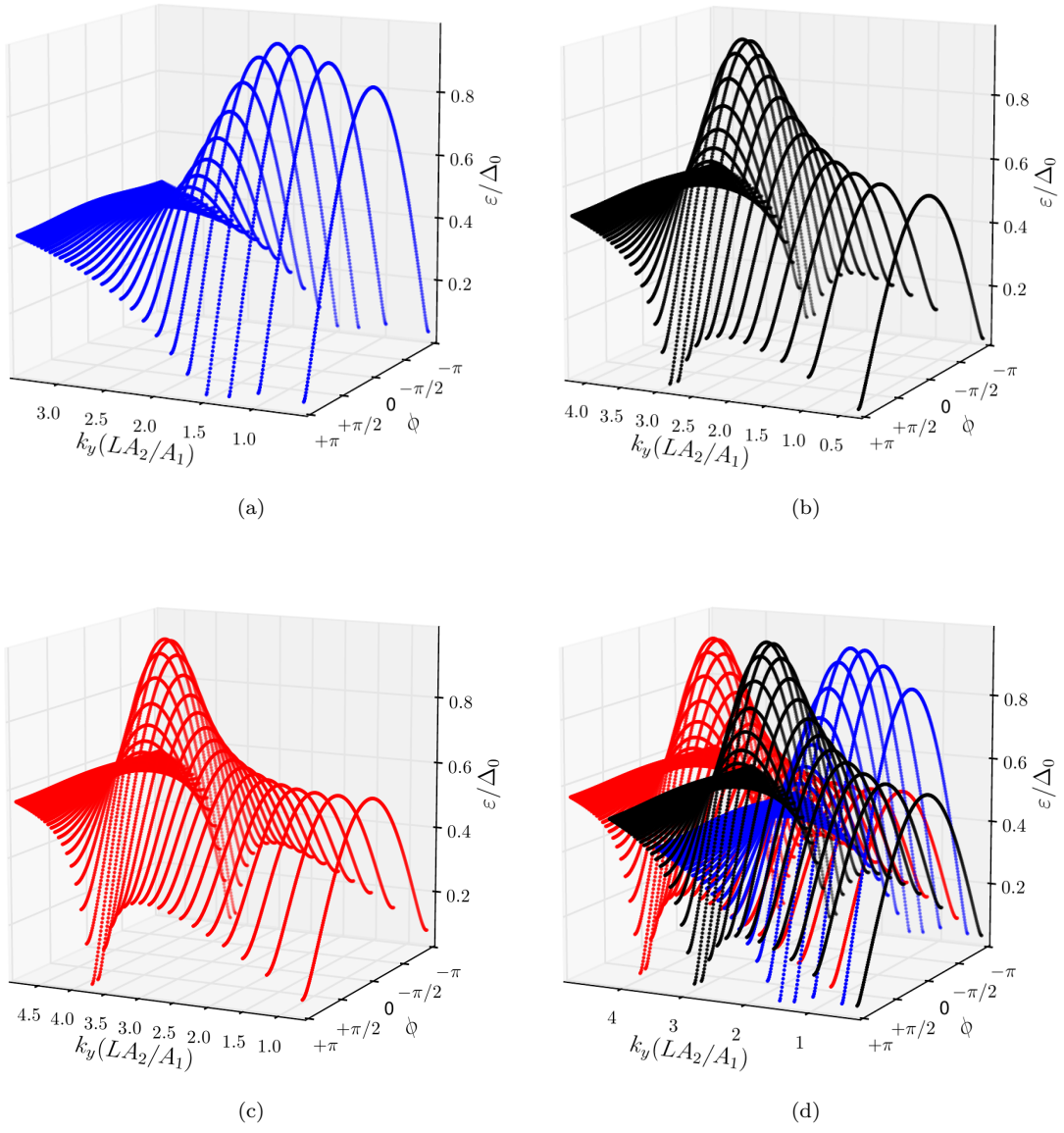

Figure 31: Energy dependence on the superconducting phase difference ϕ and on k_y for different $\Lambda = \frac{\mu - \varepsilon_0^{yz}}{\hbar v_F^{yz}} \left(\frac{A_2 L}{A_1}\right)$. The magnetization is chosen to be $q_x = \frac{m_x}{\hbar v_F^{yz}} \frac{A_2 L}{A_1} = 7$. The values for Λ are (a) $\Lambda = 7.8$, (b) $\Lambda = 8.17$ and (c) $\Lambda = 8.52$. (d) shows a comparison of (a), (b) and (c).

Zero energy modes:

Zero energy modes are particularly interesting, because $\varepsilon = 0$ is the necessary condition for the appearance of a Majorana bound state. Furthermore, we know that k_y needs to be 0 and that κ has to be real, such that the particle can be its own antiparticle. This means the Majorana modes need to decay in $z-$direction. To analyze the appearance of zero energy modes, we look at the energy (Eq. (237)) and set it to 0. This leads to the equations: $\kappa^2 + (k_y^2 + m_x^2)\sinh^2(\kappa L) \neq 0$ (denominator has to be nonzero) and $\kappa^2 + k_y^2 \sinh^2(\kappa L) - \kappa^2 \sin^2(\phi/2) = 0$. For a general phase difference ϕ the second condition can only be fulfilled if $\kappa = k_y = 0$. We note, that the denominator (condition one) gets 0, but we can take the limit $\{\kappa, k_y\} \to 0$ and we see that $\varepsilon \to 0$, thus this is a zero energy solution. It also requires $q_x = \pm\Lambda$. By substituting this condition in the wave function of the second region, we can see that the spinor can never take a form of a Majorana spinor.

The remaining zero energy modes need $\phi = \pm\pi$. For κ real, there is no additional zero energy mode to the one already mentioned. There are still several cases where we have zero energy for waves propagating

in z, thus $k_z \neq 0$:

1. $k_z = n\pi/L$ and $k_y = 0$, where $n > 0$ is an integer.

2. $k_z = n\pi/L$ and $k_y\sqrt{\Lambda^2 - q^2 - (n\pi)^2} \neq 0$. In Fig. 32 the possible $k_y \frac{A_2 L}{A_1}$ for the corresponding q_x values are plotted, for $-15 \leq \Lambda \leq 15$, $k_z L = \phi = \pi$. The zero energy points in the Figs. 30 and 31 are such zero energy modes. In Tab. 2 the three zero energy points in 31 for $\phi = \pi$ are characterized.

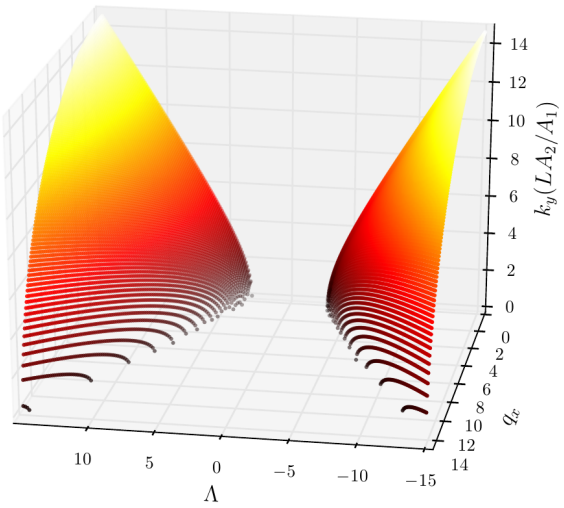

Figure 32: Zero energy modes with $k_z L = \phi = \pi$. The plot shows the allowed $k_y \frac{A_2 L}{A_1}$ values for different magnetization $q_x = \frac{m_x}{\hbar v_F^{yz}} \frac{A_2 L}{A_1}$ and different $\Lambda = \frac{\mu - \varepsilon_0^{yz}}{\hbar v_F^{yz}} \left(\frac{A_2 L}{A_1}\right)$.

$\Lambda = \frac{\mu - \varepsilon_0^{yz}}{\hbar v_F^{yz}} \left(\frac{A_2 L}{A_1}\right)$	$\frac{A_2 L}{A_1} k_y$	$k_z L$
7.8	1.4	π
8.17	2.8	π
8.52	3.7	π

Table 2: Characterization of three different zero energy points at $\phi = \pi$ for magnetization $q_x = \frac{m_x}{\hbar v_F^{yz}} \frac{A_2 L}{A_1} = 7$.

The non-monotonic behaviour in the critical Josephson current may arise due to the zero energy modes appearing in the energy spectrum of ferromagnetic topological insulator junctions. But as the calculation of the critical current involves numerically solving an integral and maximizing the current with respect to the superconducting phase difference, the analysis becomes very intriguing. In a next step, we analyze the appearance of new propagating modes.

Comparison to number of propagating modes:
We compare the values of Λ, where this non-monotonic behavior arises, to the scaled number of modes $N' = N \cdot \frac{L}{W} \frac{A_2}{A_1} = \sqrt{\Lambda^2 - q_x^2}/\pi$. Doing so, we find that when Λ is small enough such that the curve is still monotonic, $N' < 1$. We increase Λ and just before the first local maximum of J_c, N' exceeds 1. Just before the second local maximum, we have $N' \geq 2$. When plotting the superconducting phase difference $\phi(J_c)$ which maximizes the current J against Λ, we find that this phase difference oscillates between larger values for larger q_x. This is shown in Fig. 33. The crosses indicate the value of Λ where N' becomes an integer. Again we see that by increasing Λ the next integer value of N' is achieved just

before the maximum of $\phi(J_c)$. All this suggests that this non-monotonic behavior arises due to quantum interference of the new additional propagating mode and the already existing ones.

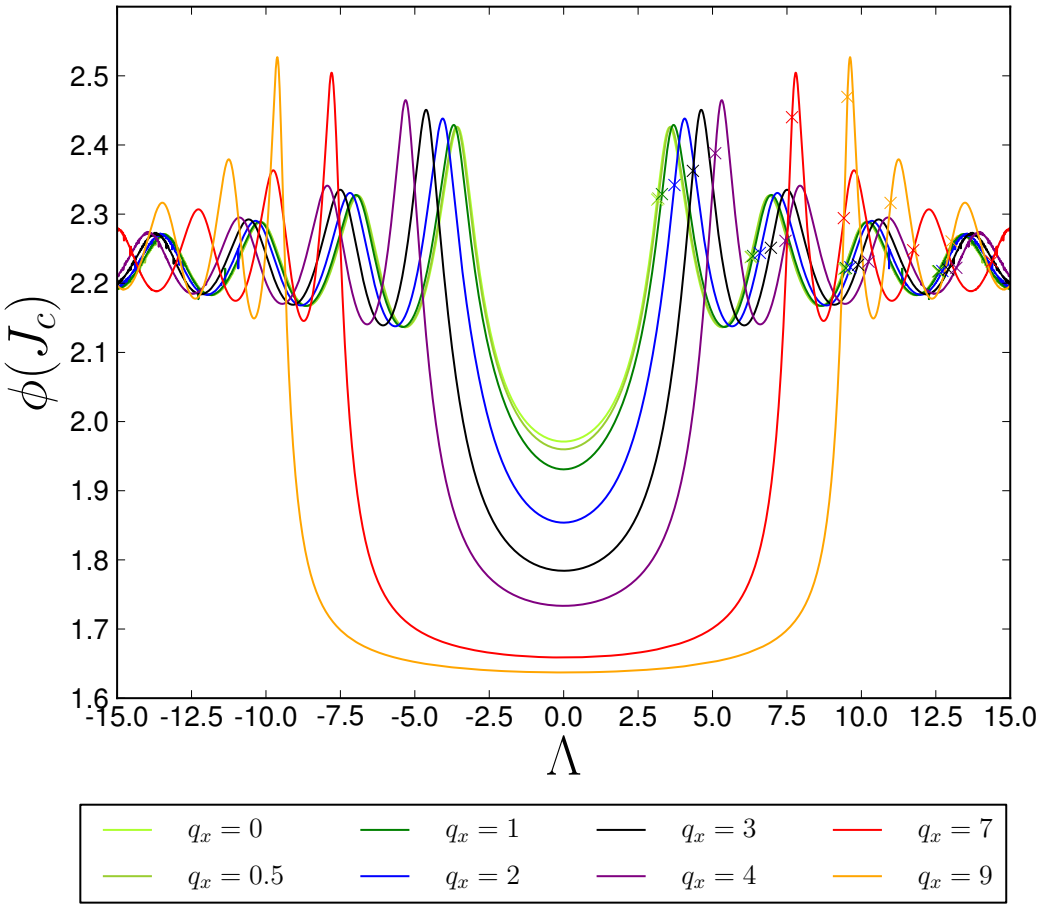

Figure 33: Superconducting phase difference $\phi(J_c)$ (which maximizes the current J) as a function of $\Lambda = \frac{\mu - \varepsilon_0^{yz}}{\hbar v_F^{yz}} \left(\frac{A_2 L}{A_1}\right)$ for different values of $q_x = \frac{m_x}{\hbar v_F^{yz}} \frac{L A_2}{A_1}$. The crosses indicate the Λ at which the scaled number of modes $N' = N \cdot \frac{L}{W} \frac{A_2}{A_1} = \sqrt{\Lambda^2 - q_x^2})/\pi$ takes an integer value.

References

[1] P. W. Anderson. *Basic notions of condensed matter physics*. Reading, Mass.: Advanced Book Program, Addison-Wesley, 1997. Originally published: Menlo Park, Calif.: Benjamin/Cummings Pub. Co., Advanced Book Program, 1984.

[2] C. L. Kane and E. J. Mele. Topological order and the quantum spin Hall effect. *Phys. Rev. Lett.*, 95:146802, Sep 2005.

[3] B. Andrei Bernevig, T. L. Hughes, and S. C. Zhang. Quantum spin Hall effect and topological phase transition in HgTe quantum wells. *Science*, 314(5806):1757, 2006.

[4] L. Fu and C. L. Kane. Topological insulators with inversion symmetry. *Phys. Rev. B*, 76(4):045302, July 2007.

[5] J. E. Moore and L. Balents. Topological invariants of time-reversal-invariant band structures. *Phys. Rev. B*, 75:121306, Mar 2007.

[6] R. Roy. Z_2 classification of quantum spin Hall systems: An approach using time-reversal invariance. *Phys. Rev. B*, 79:195321, May 2009.

[7] D. Hsieh, D. Qian, L. Wray, Y. Xia, Y. S. Hor, R. J. Cava, and M. Z. Hasan. A topological Dirac insulator in a quantum spin Hall phase (experimental realization of a 3d topological insulator). *ArXiv e-prints*, October 2009.

[8] M. König, H. Buhmann, L. W. Molenkamp, T. Hughes, C. X. Liu, X. L. Qi, and S. C. Zhang. The quantum spin Hall effect: Theory and experiment. *Journal of the Physical Society of Japan*, 77(3):031007, 2008.

[9] C. Wu, B. A. Bernevig, and S. C. Zhang. Helical liquid and the edge of quantum spin Hall systems. *Phys. Rev. Lett.*, 96:106401, Mar 2006.

[10] M. Z. Hasan and C. L. Kane. *Colloquium*: Topological insulators. *Rev. Mod. Phys.*, 82:3045, Nov 2010.

[11] X. L. Qi and S. C. Zhang. Topological insulators and superconductors. *Rev. Mod. Phys.*, 83:1057, Oct 2011.

[12] H. Zhang, C. X. Liu, X. L. Qi, X. Dai, Z. Fang, and S. C. Zhang. Topological insulators in Bi_2Se_3, Bi_2Te_3 and Sb_2Te_3 with a single Dirac cone on the surface. *Nat. Phys*, 5(6):438, June 2009.

[13] C. X. Liu, X. L. Qi, H. Zhang, X. Dai, Z. Fang, and S. C. Zhang. Model Hamiltonian for topological insulators. *Phys. Rev. B*, 82:045122, Jul 2010.

[14] X. L. Qi and S. C. Zhang. Topological insulators and superconductors. *Rev. Mod. Phys.*, 83(4):1057, October 2011.

[15] M. Tinkham. *Introduction to Superconductivity*. Dover books on physics and chemistry. Dover Publications, 2004.

[16] J. Bardeen, L. N. Cooper, and J. R. Schrieffer. Theory of superconductivity. *Phys. Rev.*, 108:1175, Dec 1957.

[17] P. G. De Gennes. *Superconductivity Of Metals And Alloys*. Advanced Book Program, Perseus Books, 1999.

[18] J. Linder, Y. Tanaka, T. Yokoyama, A. Sudbø, and N. Nagaosa. Interplay between superconductivity and ferromagnetism on a topological insulator. *Phys. Rev. B*, 81:184525, May 2010.

[19] N. Read and D. Green. Paired states of fermions in two dimensions with breaking of parity and time-reversal symmetries and the fractional quantum Hall effect. *Phys. Rev. B*, 61:10267, April 2000.

[20] L. Fu and C. L. Kane. Superconducting proximity effect and majorana fermions at the surface of a topological insulator. *Phys. Rev. Lett.*, 100:096407, Mar 2008.

[21] T. Yokoyama, Y. Tanaka, and N. Nagaosa. Anomalous magnetoresistance of a two-dimensional ferromagnet/ferromagnet junction on the surface of a topological insulator. *Phys. Rev. B*, 81:121401, Mar 2010.

[22] L. Martin and K. Flensberg. Introduction to topological superconductivity and Majorana fermions. *Semiconductor Science and Technology*, 27(12):124003, 2012.

[23] Y. V. Nazarov and Y. M. Blanter. *Quantum Transport: Introduction to Nanoscience*. Cambridge University Press, 2009.

[24] B. D. Josephson. Possible new effects in superconductive tunnelling. *Physics Letters*, 1(7):251, 1962.

[25] B. Zhou, H. Z. Lu, R. L. Chu, S. Q. Shen, and Q. Niu. Finite size effects on helical edge states in a quantum spin-Hall system. *Phys. Rev. Lett.*, 101:246807, Dec 2008.

[26] W. Y. Shan, H. Z. Lu, and S. Q. Shen. Effective continuous model for surface states and thin films of three-dimensional topological insulators. *New Journal of Physics*, 12(4):043048, 2010.

[27] D. Sen and O. Deb. Junction between surfaces of two topological insulators. *Phys. Rev. B*, 85(24):245402, June 2012.

[28] M. V. Berry and R. J. Mondragon. Neutrino billiards: Time-reversal symmetry-breaking without magnetic fields. *Proceedings of the Royal Society of London. A. Mathematical and Physical Sciences*, 412(1842):53, 1987.

[29] J. Tworzydło, B. Trauzettel, M. Titov, A. Rycerz, and C. W. J. Beenakker. Sub-poissonian shot noise in graphene. *Phys. Rev. Lett.*, 96(24):246802, June 2006.

[30] C. W. J. Beenakker and H. van Houten. Josephson current through a superconducting quantum point contact shorter than the coherence length. *Phys. Rev. Lett.*, 66:3056, Jun 1991.

[31] M. Titov and C. W. J. Beenakker. Josephson effect in ballistic graphene. *Phys. Rev. B*, 74(4):041401, July 2006.

[32] Y. Tanaka, T. Yokoyama, and N. Nagaosa. Manipulation of the Majorana fermion, Andreev reflection, and Josephson current on topological insulators. *Phys. Rev. Lett.*, 103:107002, Sep 2009.

[33] V. Parente, P. Lucignano, P. Vitale, A. Tagliacozzo, and F. Guinea. Spin connection and boundary states in a topological insulator. *Phys. Rev. B*, 83:075424, Feb 2011.

[34] Ş. Kuru, J. Negro, and L. M. Nieto. Exact analytic solutions for a Dirac electron moving in graphene under magnetic fields. *Journal of Physics: Condensed Matter*, 21(45):455305, 2009.

[35] M. Alos-Palop, R. P. Tiwari, and M. Blaauboer. Suppression of conductance in a topological insulator nanostep junction. *Phys. Rev. B*, 87(3):035432, January 2013.